Study on Expansion Performance of Calcified Coronary Arteries by Finite Element Modeling and Analysis of a Balloon with Blades

ブレード付バルーンの有限要素モデル化と解析による冠動脈石灰化病変の拡張性能に関する研究

2021 年 7 月

朱　暁冬

Xiaodong ZHU

Study on Expansion Performance of Calcified Coronary Arteries by Finite Element Modeling and Analysis of a Balloon with Blades

ブレード付バルーンの有限要素モデル化と解析による冠動脈石灰化病変の拡張性能に関する研究

2021 年 7 月

早稲田大学大学院　創造理工学研究科

総合機械工学専攻　医用機械工学応用研究

朱　暁冬

Xiaodong ZHU

Abstract

Coronary artery disease has been recognized as the first cause of death in the world among the common causes of death in non-communicable diseases, which induced the largest number of deaths in 2017 and a high increase of 22.3 % from 2007 to 2017. Coronary artery calcification is a risk factor associated with major adverse cardiovascular events and increases luminal stenosis and cause of coronary artery thrombosis. Although, drug-eluting stents have substantially reduced the rate of in-stent restenosis and have improved clinical outcomes compared with those of bare-metal stents, coronary artery calcification is still a problematic lesion, increasing the possibility of procedural failure and the risk of complications after conventional balloon angioplasty. Furthermore, it is associated with stent underexpansion, a higher rate of restenosis and stent thrombosis compared with simpler lesions. Therefore, plaque modification, utilizing cutting balloon, scoring balloon, or rotational atherectomy devices for calcified artery lesions prior to stent implantation is a key procedure in percutaneous coronary intervention.

Cutting balloon angioplasty has been a useful alternative treatment for calcified artery lesions before stent implantation. The cutting-balloon catheter has three or four microsurgical metal blades mounted longitudinally on the outer surface of the balloon, which can create incisions in the calcification during expansion to improve the coronary artery compliance to gain larger lumen expansion to facilitate the subsequent stent implantation. However, cutting balloon angioplasty in calcified lesions is associated with increased incidences of arterial dissection and perforation. A multicenter randomized clinical trial showed that the incidence of coronary artery perforation was associated with the cutting balloon, although the rate of target vessel revascularization was reduced in comparison with conventional balloons.

For cutting balloon expansion, like conventional balloon angioplasty, a balloon-to-artery ratio

of 1:1 is used. However, there is little knowledge of how the balloon-to-artery ratio for the cutting balloon influences both effective incision of the calcification and potential perforation

The author hypothesizes that there exists an adequate balloon-to-artery ratio specific to the cutting balloon in terms of effectively inducing stress concentration at the calcification for fracturing calcification while reducing the stress concentration at the borders of the coronary artery adjacent to the calcification for preventing perforation. The number of blades facing a calcified lesion may also be crucial for expanding calcifications while avoiding dissection and vessel injuries.

The author aims to investigate the influences of balloon-to-artery ratios of the cutting balloon on the stress concentrations and distribution in the calcification model and at the borders of the coronary artery adjacent to the calcification using finite element analysis in order to obtain a criterion for the balloon-to-artery ratio for the cutting balloon. The author also focuses on a calcified artery with a 180° calcification model with two conditions where either one or two blades face the 180° calcification model to gain mechanistic insights into calcification incisions using cutting balloons and to provide suggestions for improving the clinical outcomes of cutting balloon angioplasty.

This thesis is composed of five chapters. Descriptions of each chapter are presented following.

Chapter 1 introduces the current therapies for coronary artery calcification and highlights the complications in the cutting balloon angioplasty. The author summarizes the related studies in the field of numerical researches of balloon expansion. Moreover, the author shows the necessity of investigation of the cutting balloon expansion in calcified lesions and describes the purpose of this study.

Chapter 2 introduces the novel modeling of a three-folded balloon. The initial diameter and

Young's modulus of the balloon model are obtained based on the manufacturer's compliance chart data indicating the relationship of the diameter and pressure. An innovative numerical process of crimping and compressing is employed to generate a realistic three-folded balloon model according to the manufacturing process. The numerical expansion of the folded balloon model is in agreement with the compliance chart data. In addition, the folded balloon model is successfully used to expand a coronary stent model and the phenomenon of dogbone shape is reproduced. Finally, the balloon expansion of the stent model in a stenotic artery model is carried out to confirm the reliability of the balloon model in comparison with a radial displacement-driven cylinder expansion. The simulations of expansion are carried out in Abaqus/Explicit solver with adequate analysis time step and loading rate to ensure a quasi-static analysis while the kinetic energy remained almost below 5% of the internal energy for each model. The contact condition between each model is defined utilizing the general contact algorithm with a static friction coefficient of 0.2. The peak value of the von Mises stress occurred in the stent model for the balloon expansion was similar to that for the cylinder expansion at the final process. On the other hand, the peak value of the maximum principal stress in the plaque model for the cylinder expansion was 144 % higher than that for the balloon expansion of that for the balloon expansion. The folded balloon model shows a good response to the realistic expansion and the method of validated modeling promotes further modeling of the balloon.

Chapter 3 describes the expansion of a cutting balloon with five different diameters in a stenotic calcified artery model. As in conventional balloon angioplasty, a balloon-to-artery ratio of 1:1 is used for the cutting balloon with metallic blades. The author aims to investigate the influence of the balloon-to-artery ratio on the stress concentrations in the calcified model and at the borders of the coronary artery adjacent to the calcification to obtain a criterion of

balloon-to-artery ratio for the cutting balloon. The folded cutting balloon model is generated by the method described in Chapter 2 and equipped with three pairs of blades and cast pads on the balloon surface. The cutting balloon model is deployed in a 50% diameter stenotic coronary artery model with a 360° concentric, 400-μm-thick, 5-mm-long calcification. Simulations of the expansion of cutting balloons with diameters from 2.0 to 3.0 mm in 0.25-mm increments which corresponded to balloon-to-artery ratios from 0.67:1 to 1:1 were conducted with pressures up to 1.216 MPa (12 atm). The result reveals that the cutting balloon downsized by 0.25 mm and 0.5 mm preserved maximum principal tensile stress concentrations comparable to that of the cutting balloon with a balloon-to-artery of 1:1 while distinctly reducing the stress concentrations at the border of the artery adjacent to the calcification. The data shows that selecting a cutting balloon downsized by 0.25 mm or 0.5 mm should be the first choice for effectively fracturing the calcification while reducing the risks of artery perforation. For the cutting balloon, a balloon-to-artery of 1:1, which is recommended for conventional balloons, seems inappropriate.

Chapter 4 describes the expansion of the cutting balloon in a non-circular calcified artery model. The author hypothesizes that the balloon-to-artery ratio and the number of blades facing a 180° calcified lesion may be crucial for fracturing the calcification while avoiding vessel injury. Numerical simulations were performed for cutting balloons with five different diameters and two types of blade directions in a 180° calcification model. The calcification expansion ability was distinctly higher when two blades faced the calcification than when one blade did. Moreover, when two blades faced the calcification model, larger maximum principal stresses were generated in the calcification even when using undersized balloons with diameters reduced by 0.25 or 0.5 mm from the reference diameter, when compared with the case where one blade faced the calcification and a balloon of diameter equal to the reference diameter was used. When two blades faced the calcification, smaller stresses were generated in the artery adjacent

to the calcification. Furthermore, the maximum stress generated in the artery model adjacent to the calcification under the rated pressure of 12 atm when employing under-sized balloons was smaller than that when only one blade faced the calcification and when lesion-identical balloon diameters were used under nominal pressure of 6 atm. The data suggested that 0.25 mm or 0.5 mm size-down balloons would be effective in not only expanding the calcified lesion but also reducing the risk of dissection.

Chapter 5 summarizes the conclusions and describes the plans for future work.

The significance of the thesis is that the author not only proposes realistic and validated modeling of a three-folded balloon to generate the configurations of the cutting balloons but also reveals the influence of the expansion of the cutting balloons in calcified artery models. These results will contribute to improve the clinical outcomes of cutting balloon angioplasty and help to promote the future development of the cutting balloon.

Acknowledgement

First of all, I would like to gratefully thank my supervisor Prof. Kiyotaka Iwasaki for his guidance and support. He improved the quality of my research and other works over the last eight years, including master's and doctoral degree programs. I also express my thankfulness to my reviewers Prof. Mitsuo Umezu, Prof. Atsuo Takanishi and Prof. Makoto Yoshida, for their important comments and suggestions in improving this dissertation.

Prof. Mitsuo Umezu and Prof. Kiyotaka Iwasaki gave me the opportunity to join their outstanding research team. They are experts in Bio-engineering with high-level research on medical devices, tissue engineering, artificial organs, cellular engineering, and so on. At the beginning of my master's degree program, my first challenge was considering the theme of finite element analysis on coronary stents to verify the performance and safety. At the same time, in-vitro experiments had been carried out by the team members for a period. Many members in Umezu/Iwasaki Laboratory supported me to create numerical models and taught me the knowledge of medical devices and heart disease. A folded balloon shape and balloon-expansion simulation in the cutting balloon study became the new subjects during my doctoral degree program. Prof. Kiyotaka Iwasaki and my team members gave me many suggestions for my work. Some very important persons, Prof. Yagi, Prof. Sakaguchi, Ph.D.Tobe@Pittsburgh, Ph.D. Matsuhashi, Ph.D. Tsuboko, Dr. Yamamoto@Hokkaido, Dr. Hikichi@Saga and others also helped me very much. Words cannot describe my sincere feelings towards their kind supports.

Finally, I would like to express my gratitude to my family and parents for the constant support. I would also like to thank my wonderful wife Xia Jing and my lovely son Zhu Xiarui. They supported and encouraged me to finish my study.

Tokyo, June 2021

Xiaodong ZHU

Table of contents

Chapter 1: Introduction

1.1 Chapter introduction

In recent years, coronary artery disease (CAD) has been effectively treated with the development of percutaneous coronary intervention (PCI) such as balloon angioplasty and stent deployment. In the case of the calcified lesion, a balloon or stent seem to be difficult to expand the lesion due to the existence of stiff calcified plaque. Therefore, a specialized balloon such as cutting balloon catheter, which consists of metal blades on the balloon surface, has been developed to treat the calcified lesion before stent deployment.

This thesis aims to construct a numerical cutting balloon model and investigate the efficacy and safety of the cutting balloon expansion in a calcified coronary artery model utilizing finite element analysis. This study generates a folded balloon process to construct the cutting balloon model and a calcified artery model with different calcification angles.

In this chapter, the background of this study introduces the general treatment for coronary artery calcification and emphasizes the importance of the cutting balloon in order to show the purpose of this study. Next, the chapter shows the state-of-arts of related studies to understand the finite element balloon model, definition of plaque material model, and reference research. Finally, a composition of this thesis is showed to understand the flow and contents of this study.

1.2 Background of this study

1.2.1 Coronary artery calcification

Coronary artery disease is a common of the cardiovascular disease, which reduces the blood flow to the heart muscle through building up plaques in the arteries of the heart. Chest pain or discomfort is the common symptom and shortness of breath may also occur sometimes. In many cases, the initial paroxysm is heart attack, leading to angina, myocardial infarction, ischemic heart failure and sudden cardiac death.

Coronary artery disease affected about 126 million persons and caused approximately 8.93 million deaths in the world in 2017 [1] [2]. Among the common causes of death in non-communicable diseases, due to the largest numbers of deaths in 2017 and the high increase of 22.3% from 2007 to 2017, coronary artery disease has been recognized the first cause of death in the world (Fig1.1).

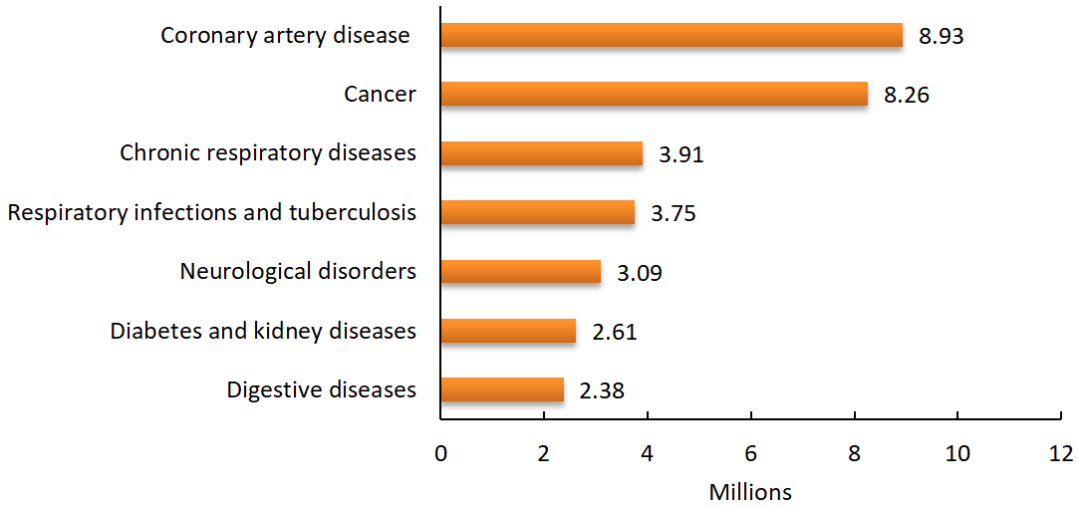

Figure 1.1 Global number of deaths by cause in 2017 for non-communicable diseases. [1] [2]

Coronary artery calcification develops from micro-calcification in atherosclerotic coronary arteries with pathological intimal thickening. Micro-calcifications grow and combine into larger masses to form speckles and fragments of calcifications over time and further result in calcified plaques with calcified sheets or plates, leading to nodular calcification. Moreover, those heavily

calcified segments might be associated with severe arterial calcification with increasing luminal stenosis and cause of thrombosis [3].

In clinical detection for coronary artery calcification, intravascular ultrasound (IVUS) with sensitivity of 90% to 100% and specificity of 99% to 100% is substantially accurate so that several metrics can grade the calcification. The arc of calcification can be defined as Class I (0^{o} ~90^{o}), Class II (91^{o}~180^{o}), Class III (181^{o}~270^{o}) and Class IV (271^{o}~360^{o}). Location of calcification can be classified into two distinct generations in the intimal-luminal interface (intimal calcification) or in the vascular medial layer. The calcium length also can be measured and the thickness or volume of calcium can be examined through Optimal coherence tomography (OCT) [4].

Percutaneous coronary intervention (PCI) is a typical therapy for coronary artery disease. This process combines coronary angioplasty and stent implantation to treat narrowed coronary arteries of the heart. Several PCI strategies such as rotational atherectomy, balloon angioplasty, specialized balloon, stent implantation, and post-dilation have been used to treat coronary artery calcification. Balloon angioplasty, stent implantation and specialized balloons will be presented following.

1.2.2 Balloon Angioplasty

Balloon angioplasty is a balloon catheter with a deflated balloon on the catheter, inserted into the narrowed artery through a guidewire and inflated to increase the balloon diameter to expand the artery and surrounding muscular wall to improve the blood flow. The process is illustrated in Fig 1.2.

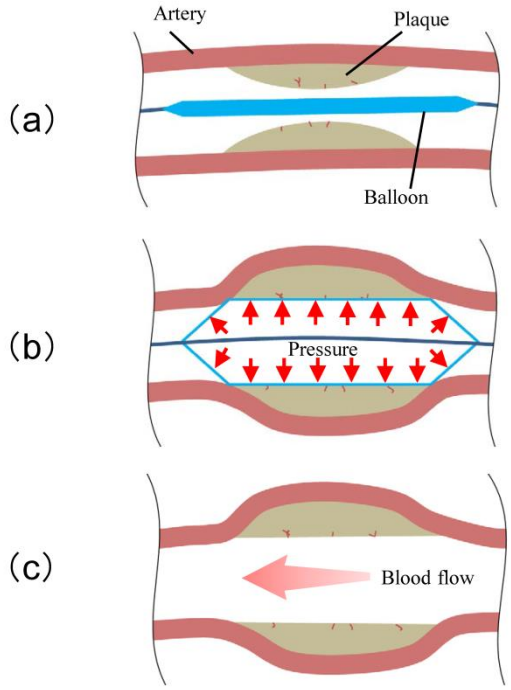

Figure 1.2 Process for balloon angioplasty. (a) delivering the balloon catheter into the stenotic lesion (b) expanding the balloon (c) after balloon expansion.

Balloon catheters are in a wide range for diameters from 2.0 mm to 4.0 mm, lengths of 10 mm to 40 mm to match the dimension of the coronary lesion. A typical balloon catheter consists of a cylindrical balloon body and two conical tapered ends fixed on the catheter shaft. The balloon is expanded by high pressure to apply force to compress the plaque inside the lesion.

Balloon angioplasty effectively treats stenotic coronary by compressing and breaking the atherosclerotic plaque in the diseased artery wall. However, in some clinical studies, coronary artery calcification is recognized as a factor of the increase of procedural failure and complication after balloon angioplasty [4] [5] [6]. Non-compliant calcified plaques usually need high-pressure balloon dilation as high as 20atm or more. This further increases the risk of coronary dissection or perforation, restenosis and thrombosis [7] [8] [9]. For these clinical reasons, coronary balloon angioplasty is often used to combine with stent implantation.

1.2.3 Stent implantation

A coronary stent is a metal mesh tiny tube device used to expand the stenotic coronary artery to keep the blood flow to the heart. It is equipped with a balloon catheter and can be inserted into a narrowed coronary artery. The coronary stent is expanded by balloon pressurization undergoing elastoplastic deformation to reach its required diameter. Next, the balloon is deflated and then withdrawn from the artery. The stent will partly recover the elastic deformation and its diameter will slightly shrink. This is called elastic recoil. The stent supports the artery wall to keep normal blood flow in the coronary artery.

Bare-metal stents (BMS) were first developed during the 1980s and widely used in the 1990s [10]. BMSs have reduced restenosis in comparison with balloon angioplasty [11] [12]. However, stent underexpansion observed in heavily calcified lesions increases the risk of complications such as in-stent restenosis and stent thrombosis [13] [14] [15].

A drug-eluting stent (DES) is a coating BMS with drugs that releases sirolimus or paclitaxel to deal with in-stent restenosis. The DESs have resulted in a lower rate of in-stent restenosis less than 10% in comparison with the rate of 30% ~ 40% in BMSs [16]. In coronary artery calcification lesions, some studies have shown that DES is more effective than BMS with less restenosis and repeat revascularization [17] [18] [19]. Furthermore, similar rates of stent thrombosis with DES and BMS with similar rates of myocardial infarction and death in calcified lesions have been reported [18] [19] [20]. On the other hand, however, there are higher rates of in-stent restenosis and repeat revascularization including stent underexpansion with DES in calcified lesions compared with non-calcified lesions. [21] [22]. Therefore, to facilitate the DES implantation in the calcified lesions, lesion preparation or also called plaque

modification utilizing cutting balloon (CB), scoring balloon (SB) or rotational atherectomy (RA) is very important before stent implantation [23] [24].

1.2.4 Cutting balloon

A cutting balloon is a balloon catheter with three or four microsurgical metal blades mounted longitudinally on the outer surface of the balloon. These tiny metal blades can create incisions in the plaque in the stenotic coronary artery during balloon dilation to improve the artery compliance to gain larger lumen expansion. Similarly, a scoring balloon is a balloon catheter equipped with one or more scoring elements (metal wires or polymer elements), reducing balloon slippage and generating focal concentrations of expanding force on the plaques in the stenotic coronary arteries during balloon dilation. In addition, a rotational atherectomy is a device using a diamond-tipped elliptical burr with rotational speed as high as 200,000 rpm to ablate the coronary calcium. Cutting balloons and scoring balloons are called specialized balloon or modified balloon.

Cutting balloons (e.g., Flextome Cutting Balloon; Boston Scientific Corp, Natick, MA) have been applied to treat coronary artery calcification to achieve a larger luminal gain to improve the thereafter stent implantation and have been verified the usefulness [25] [26]. Nevertheless, a global randomized trial showed no difference for the rate of restenosis as compared to conventional balloon angioplasty (31.4% vs 30.4%, $p = 0.75$) at six months and reported a greater rate of perforation in cutting balloon angioplasty (0.8% vs 0%, $p = 0.03$) [27]. Arterial dissection is likewise a complication after cutting balloon angioplasty in clinical treatment [25] [28]. Regarding the rate of restenosis and the existing perforation or dissection in clinical studies, cutting balloons are largely used for selected cases with mild to moderate calcified

lesions. Severely calcified lesions seem to be the domain of rotational atherectomy as recommended by the ACCF/AHA/SCAI Guideline [29], since rigidity and bulkiness of the cutting balloon catheter causing delivery challenge. Therefore, a new generation of the Flextome cutting balloon, Wolverine cutting balloon (Boston Scientific Corp) is available with less bulky, more flexible, lower profile so as to be more deliverable in calcified lesions [30].

1.3 Related studies

1.3.1 Folded balloon shape

A balloon catheter consists of an inflatable balloon and an inner shaft connecting to a guidewire. The initial balloon shape is a cylinder body with two tips mounted on the inner shaft. The basic product information of a balloon catheter is balloon length, balloon diameter, shaft outside diameter as well as compliance chart. A compliance chart indicates the relationship between the pressurized Atmosphere and balloon outer diameter supplied by the manufacturer.

A balloon is manufactured to form a wrapped shape to obtain a smaller diameter than a reference lesion caliber so that it can be inserted into a narrowed artery. A balloon wrapper machine including the process of pleating and compressing can pleat a balloon to generate several “wings” and then wrap these wings around the catheter shaft to compress the balloon into a wrapped shape.

However, a numerical model of the wrapped balloon shape is complicated to be created and usually, a simple cylindrical model is used to replace the complex balloon model. In the early era, some studies utilized the simple cylinder models to carry out balloon-expandable stent

expansion simulation by the displacement applied on the inner surface of the cylinder models [31] [32] [33] [34]. Moreover, several studies also defined a wrapped outline in cross-section to mimic a compressed balloon [35] [36]. De Beule [37] has studied three different free-expansion strategies for a balloon-expandable stent: (1) no balloon: just applying uniform pressure directly on the stent inner surface. (2) cylindrical balloon: applying a radial displacement on the cylindrical balloon model. (3) three-folded balloon: applying uniform pressure on the inner surface of the three-folded balloon model. The three-folded balloon was designed by a closed outline in cross-section and its material properties such as the extrapolated initial diameter and elastic modulus were determined using the product compliance chart. It has been verified that the three-folded balloon expansion shows a better realistic result with “dogbone” phenomenon and good qualitative and quantitative agreement with both the manufacturers’ data and experiments than those two strategies. Ragkousis [38] developed calibrated multi-folded balloon models with tips equipped on shaft models and also compared them to manufacturer compliance charts. The initial diameter was tested through different values to obtain the best fit and the material was assumed linear isotropic elastic properties. Consequently, it showed that the balloon model closely followed the expansion behavior of the actual balloon. However, they defined the cross-section outlines to create a virtual folded balloon shape and no wrapped balloon model according to the actual process was considered.

1.3.2 Definition of numerical plaque model

In recent years, some numerical researches have concerned the expansion of balloon-expandable stents in stenotic arteries [36] [39] [40] [41] [42]. Those numerical plaque models were created into simple shapes inside artery models and they described the properties

as a cellular atherosclerotic plaque behavior using hyper-elastic material such as Moony-Rivlin or Ogden, which stiffness was similar to the artery. Therefore, the stent model was expanded by a balloon model to enlarge the narrowed artery model and finally the stent model was deployed inside to support the artery model. However, calcified plaque is stiffer than cellular atherosclerotic plaque with high elastic modulus. The mechanical properties of calcified plaques are similar to bone. The Young's modulus is as high as 20.1GPa measured from the human superficial femoral artery [43]. The heavily calcified plaque often impedes the success of stent implantation and results in stent under-expansion and some complications.

1.3.3 Numerical researches on cutting balloon

Little research is carrying out on the experimental test or numerical study on the cutting balloon or scoring balloon. A study evaluated a Scoreflex scoring balloon device [44]. They dilated the 2.0 × 15 mm scoring balloon in comparison with a 2.0 × 15 mm conventional balloon in calcium tubes with three different thicknesses of 2.0 mm, 2.25 mm, and 2.5 mm. On the other hand, a finite element analysis simulation of scoring element dilation was conducted. An arterial wall, circumferentially calcified plaque, a membrane balloon and two scoring element models were created in their finite element analysis. They set the inner diameter of calcified plaque to 1.0 mm, 1.5 mm, 2.0 mm, and 2.5 mm. The Young's modulus and Poisson's ratio of the calcified plaque model were set to be 20 GPa and 0.17, respectively. The experimental results showed that the scoring balloon could be used to expand a circumferential calcified lesion with lower pressure than the conventional balloon. The numerical simulation showed that the first principal stress concentration is the fundamental mechanism of the increased ability of the scoring balloon device to dilate a calcified lesion.

However, the calcium tubes with a larger scale than actual tissues and no artery model outside cannot represent accurate human lesion models. The two-dimensional finite element simulation has the limitation of axial length and the balloon model was not created following a realistic dimension.

A recent study from the same research group has investigated the efficacy of the Wolverine cutting balloon on a 360º circumferential calcified coronary lesion [45]. They constructed the calcification models using three-dimensional printers from patient computed tomography and intravascular ultrasound data. Wolverine cutting balloon and NC Emerge noncompliant balloon catheter were used to be inflated in the calcification models and the success rate of dilation and maximum dilation pressure were compared. They also performed two-dimensional numerical simulations using the finite element method to evaluate the maximum first principal stresses in calcified lesion models through changing the number and position of the blade.

In their bench tests, the inflation success rate of the cutting balloon was higher and the maximum inflation pressure required was lower in comparison with those of the noncompliant balloon. Numerical results showed that the blades play a role in increasing the maximum first principal stress in calcified lesions.

1.4 Purpose of this study

Clinically, a balloon-to-artery ratio of 1:1 is selected for cutting balloon expansion, like conventional balloon angioplasty [24]. In the conventional balloon angioplasty, a clinical study reported that 60% of calcium fractures were observed in lesions with large calcium arcs from 270 to 360 degrees and only 2.0% (4 of 198) of the lesions with the maximum calcium angles were ≤ 180° [46]. The angles were detected through the cross-sectional images of optical

coherence tomography in the circumferential-wise direction of the lesions.

As described in Chapter 1.2.4, arterial perforation and dissection have been recognized as the complications after cutting balloon angioplasty in clinical treatment [25] [27] [28]. There is no knowledge of how the angle of the calcification and balloon-to-artery ratio for the cutting balloon influences both the effective incision of the calcification and potential perforation or dissection. The author hypothesizes that the lesion/device diameter ratio and the number of blades facing a calcified lesion may be crucial for expanding calcifications while avoiding vessel injuries.

To the best of the author's knowledge, three-dimensional numerical models of the cutting balloon with blades and pads have not been modeled and the approach of the folded shape of the cutting balloon model and the expansion simulations have not been studied. Although the in-vitro experiment on the expansion of the cutting balloon in a stenotic calcified artery model may be appropriate to evaluate the efficacy and safety of the cutting balloon expansion, it is difficult to achieve a stenotic calcified artery model to represent a real one due to the complex material behavior of the calcium and stenotic artery. Therefore, the author considered computational models to replicate the biomechanical response of cutting balloons.

The purpose of this study is to evaluate the ability and safety of the expansion of the cutting balloon in calcified stenotic lesions. The author aims to achieve three targets as follows.

(1) to accomplish a process of a three-folded balloon model and generate the cutting balloon model with blades.

(2) to investigate the influences of balloon-to-artery ratios of the cutting balloon in a 360º calcified artery model.

(3) to investigate the influences of balloon-to-artery ratios and number of blades facing a 180º calcification.

To the best of the author's knowledge, this is the first biomechanical study on expansion ability and safety of the cutting balloon with blades and pads in the calcified artery models. The three dimensional cutting balloon models with different diameters are constructed and the effect of balloon-to-artery ratio and number of blades facing the calcification are investigated.

The biomechanical insights on the expansion of the cutting balloon in calcified artery models may help provide suggestions for improving the clinical outcomes of cutting balloon angioplasty.

1.5 Structure of this thesis

Fig 1.3 illustrates the structure of this thesis. Chapter 2 describes the details of the methodology for generating a reliable folded balloon model by means of finite element analysis and verifies the accuracy of the folded balloon expansion according to its compliance chart and the necessity for using a membrane folded balloon model to expand a coronary stent model in a stenotic artery model in comparison with a cylinder model. Chapter 3 describes the details of the construction of a cutting balloon model with blade and pad models basing on the method of folded balloon in chapter 2. The characteristics of the calcification models are considered based on the clinical studies and the angle of 360º and 180º are selected to evaluate the ability of the cutting balloon on calcium fracture. A stenotic coronary artery model with 360º calcification model is created to mimic the calcified lesion. Finite element analyses of cutting balloon expansion with different balloon-artery ratios are performed in comparison with a typical non-compliant balloon. Chapter 4 presents a 180º calcification model in the stenotic coronary artery model so that the direction of the blades should be examined and the influence of balloon-artery ratio and blade number in calcification model are evaluated. Chapter 5

summarizes the conclusion and future work.

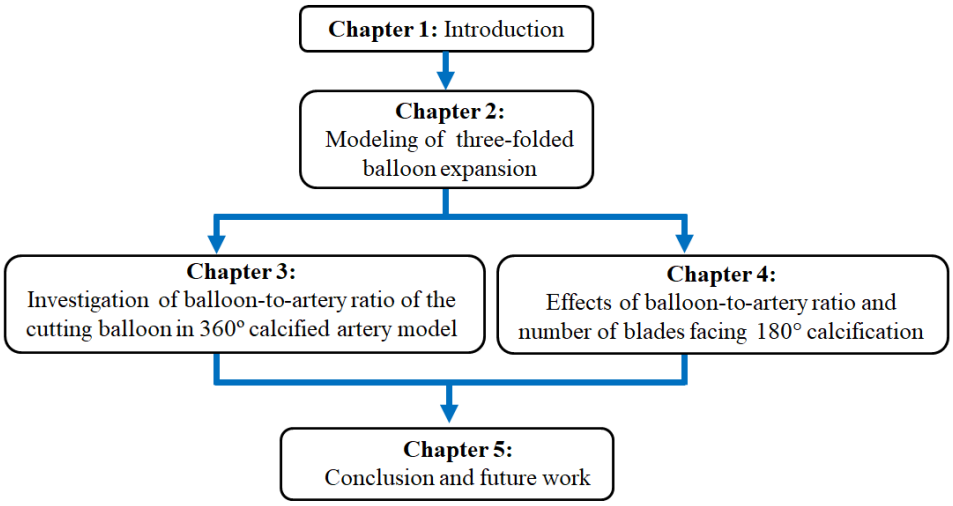

Figure 1.3 Structure of this thesis.

Chapter 2: Modeling of three-folded balloon expansion

2.1 Chapter introduction

Modeling of a three-folded balloon model is described in this chapter. The three-folded balloon is wrapped from its initial shape to be equipped with a coronary stent. The balloon is pressurized to enlarge its diameter. Meanwhile, the stent is expanded to support the artery wall. The balloon is an important device to be used to expand a balloon-expandable stent.

The objective of the chapter is to describe the modeling of the three-folded balloon and verify its accuracy and reliability for the stent expansion and details are described as follows.

(1) to crimp and compress an balloon model into a three-folded shape from the initial balloon model and verify the accuracy during balloon expansion.

(2) to simulate a free expansion for a coronary stent and expansion in a stenotic coronary artery model in comparison with a cylinder expansion.

This chapter shows the good response of the balloon expansion using the folded balloon model. The stent deformation of “dogbone” shape is realized and the result of the stress in the plaque model is more reliable than a cylinder expansion using a cylinder surface. The approach is helpful to generate a complex cutting balloon model as described in Chapter 3 and also to achieve other similar devices such as scoring balloon used in the treatment of plaque modification.

2.2 Materials and methods

2.2.1 Balloon model

2.2.1.1 Initial geometric balloon model

As introduced in chapter 1.4.1, a simple cylinder model is usually used to expand a stent model as a balloon through the radial displacement applied to the inner surface. In addition, a folded balloon model is determined through its closed cross-section outline and length with or without tips on the shaft model [37] [38]. The length of the cross-section outline is configured to be equal to the length of initial diameter before dilation. The folded balloon expansion shows better agreement with both the compliance chart data and experiments [37]. However, a real balloon catheter is made through crimping and compressing to form its folded shape. However, neither created an actual folded balloon model through crimping and compressing deformation to generate the wrapped balloon. On the other hand, although creating a wrapped balloon model through a closed cross-section outline with tips on the shaft is useful through a functional package in CAD software. A commoner and simpler numerical method for a folded balloon shape model basing on the manufactural process of crimping and compressing should be established to accomplish the numerical balloon expansion.

Fig 2.1a shows a balloon obtained from a balloon-expandable L605 cobalt-chromium alloy coronary stent catheter (Xience V, Abbott Vascular) was pressurized to 1 atm. When the inner pressure was equal to the atmosphere pressure, the shape of the balloon maintained its initial shape under this condition. The basic dimensions of length and diameter were measured based on the image and showed in Fig 2.1b. The full length, length of the balloon body and the inner

shaft diameter were 18.5 mm, 23.5 mm and 0.6 mm, respectively.

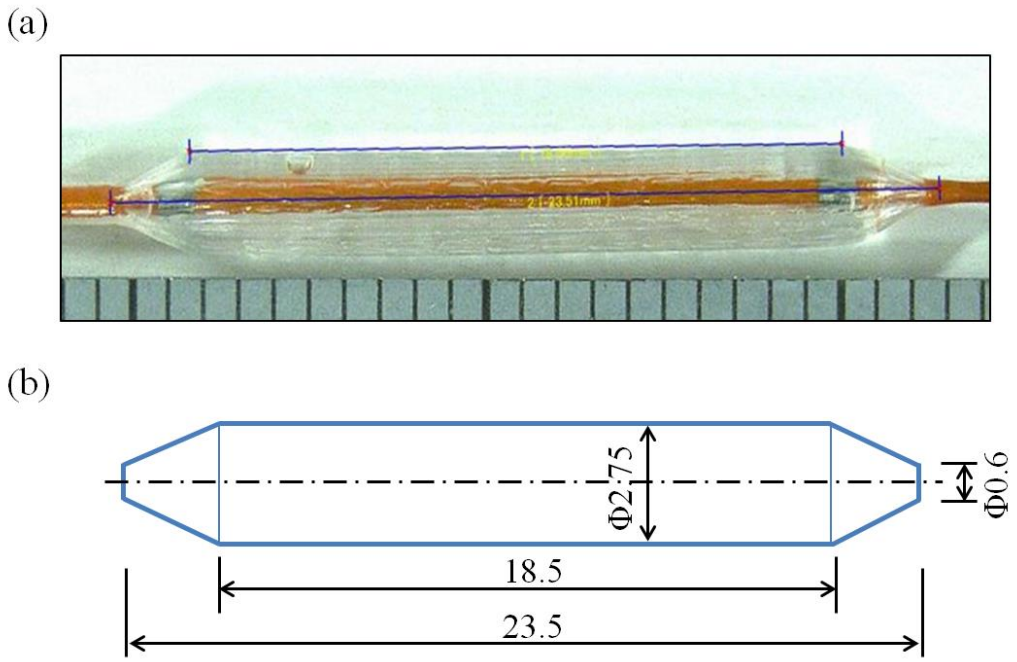

Figure 2.1 Image of the balloon (a) the inflated balloon; (b) the dimensions measured from the image (Unit: mm).

A three-dimensional computer-aided design (CAD) geometric model was created (Fig 2.2) and thereafter a cylindric shaft model was created inside along the longitudinal axis.

The compliance chart of the coronary stent, indicating the relationship between the applied pressure and the inner stent diameter (i.e. balloon outer diameter), is listed in Table 2.1. The nominal pressure is the recommended pressure at which the balloon can be inflated to reach its rated diameter such as the 3.04 mm according to the stent specification of Φ 3.0 mm and the rated burst pressure is the highest pressure. Pressure should not exceed the rated burst pressure. De Beule et al. and Ragkousis et al. have introduced a methodology to obtain an initial diameter and Young's modulus for the balloon model obtained using compliance charts [37] [38]. More details are described in De Beule, M. (2008). Finite element stent design (Doctoral dissertation, Ghent University) [47].

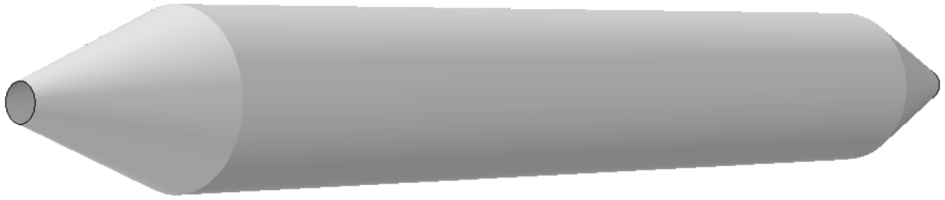

Figure 2.2 Three-dimensional CAD model for the balloon.

Four assumptions are initially presented as following:

(1) The material of the balloon model is assumed to be isotropic homogeneous linear elastic

(2) The balloon model is in the state of plane stress

(3) Balloon diameter Db / balloon thickness Tb is ≥ 5 and the thickness is uniform and constant

(4) Axis stress state is generated through the end constraint from the shaft

Therefore, the nominal circumferential stress ($\sigma_{\theta,nom}$) and strain ($\varepsilon_{\theta,nom}$) components and the nominal axial stress ($\sigma_{Z,nom}$) can be defined as following equations:

$$\varepsilon_{\theta,nom} = \frac{D_b - D_{b0}}{D_{b0}} \tag{2.1}$$

$$\sigma_{\theta,nom} = \frac{pD_b}{2T_b} \tag{2.2}$$

$$\sigma_{Z,nom} = \frac{p(D_b^2 - D_c^2)}{4T_b D_b} \tag{2.3}$$

Here, D_b is the diameter of the balloon; D_{b0} is the initial diameter of the balloon; p is the pressure; T_b is the uniform balloon thickness; D_c is the diameter of the shaft.

The initial diameter of the balloon is obtained from the plotting diagram of the compliance chart (Fig 2.3). An approximated straight line was added to the diagram and the y-intercept was set to be 2.75 mm to obtain the best fit to the compliance chart. Therefore, the initial diameter of 2.75 mm was used to define the balloon model as showed in Fig 2.1b.

Due to the balloon has two closed ends fixed on the shaft, both axial and circumferential

stress components generate during balloon dilation, meanwhile, the balloon diameter is effected by the balloon material and the constraints from the fixation to the shaft. Consequently, the constitutive behavior with the assumed elastic modulus is described as:

$$\varepsilon_{\theta,nom} = \frac{1}{E}\left(\sigma_{\theta,nom} - \nu\sigma_{Z,nom}\right) \tag{2.4}$$

Table 2.1 Compliance chart for the coronary stent.

Xience V (Φ 3 mm x 18 mm)		
Pressure		Stent inner diameter
(atm)	(kPa)	(mm)
8	811	2.90
9	912	2.97
10 (Nominal pressure)	1013	3.04
11	1115	3.10
12	1216	3.15
13	1317	3.19
14	1419	3.23
15	1520	3.26
16 (Rated burst pressure)	1621	3.30
17	1723	3.33
18	1824	3.36

E and ν are Young's modulus and Poisson's ratio.

Here, the Young's modulus can be determined through plotting the true strain in function of the true stress. Therefore, simple conversed expressions form nominal values to true values are:

$$\sigma_{true} = \sigma_{nom}(1 + \varepsilon_{nom}) \tag{2.5}$$

$$\varepsilon_{true} = \ln(1 + \varepsilon_{nom}) \tag{2.6}$$

For the two-dimensional stress state in the elastic balloon model, the circumferential true stress and true strain can be obtained through combining with equation 2.4.

$$\sigma_{\theta,true} = (\sigma_{\theta,true} - \nu\sigma_{Z,nom})(1 + \varepsilon_{\theta,nom}) \quad (2.7)$$

$$\varepsilon_{\theta,true} = \ln(1 + \varepsilon_{\theta,true}) \quad (2.8)$$

The true stress and strain were calculated and plotted in Fig 2.4. The approximated straight line with intercept of $y = 0$ was added to the diagram and the slope of 705.85 was obtained through the expression of the straight line. Therefore, Young's modulus of the elastic balloon model was characterized as 706 MPa, the Poisson's ratio and the nylon balloon material density were assumed to be 0.4 and 1100 kg/m^3.

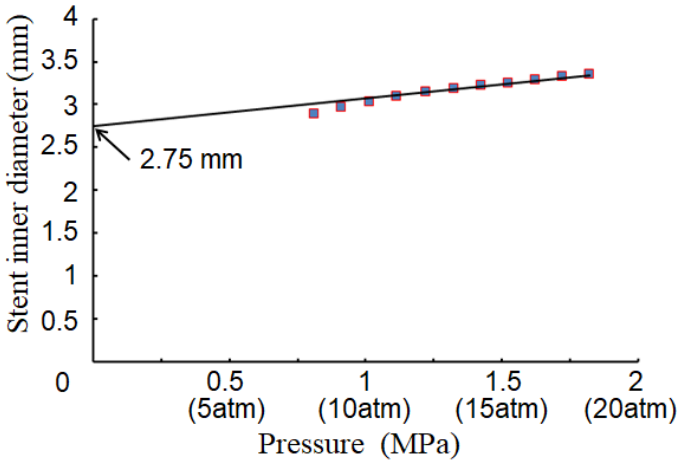

Figure 2.3 Plotting diagram for the compliance chart.

Although the initial diameter, Young' modulus, Poisson's ratio and density for the isotropic elastic balloon model were determined, the accuracy for the relationship between pressure and diameter comparing with the compliance chart should be verified. Therefore, a numerical simulation for the balloon model was carried out utilizing a finite element analysis software, Abaqus CAE 2018 / explicit (Dassault Systèmes K.K., Tokyo, Japan).

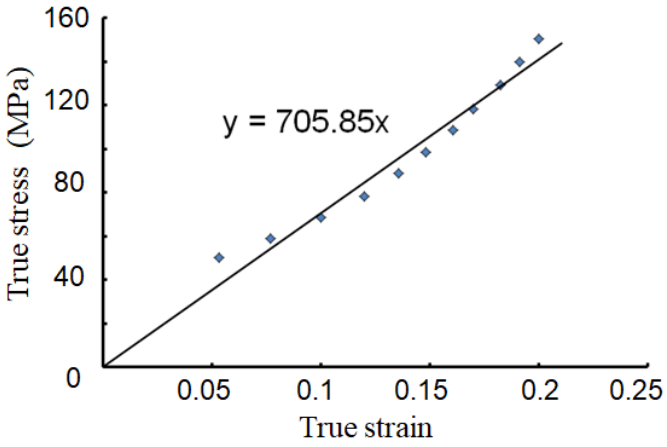

Figure 2.4 True stress and strain plotting diagram.

2.2.1.2 Shell element and membrane element

Shell elements are widely applied in mechanical engineering, biomechanics, aeronautical and marine engineering such as piping system, rockets, ships and skull [48]. A thin shell is a flat structural element bounded by two parallel faces in which the distance between the two faces is the thickness (h) of the plate. It is assumed that the thickness is small compared with other dimensions such as length, width and diameter of the face according to the maximum value of the ratio h/R $\leq$ 1/20 (R represents the radius of curvature of the middle surface). Fig 2.5 is a shell element showed to give a two-dimensional theory of thin shells eliminating the variations with respect to z direction to calculate the stress components S_1 and S_2, referring to the internal forces and moments, respectively, The coordinate axes x, y and z at each nodal point in an ent are designated by 1, 2, 3, respectively [48].

$$\mathrm{d}s_1^z = A^z dxdz = A\left(a - \frac{z}{R1}\right)dxdz\,; \quad ds_2^z = B^z dydz = B\left(a - \frac{z}{R_2}\right)dydz \qquad (2.9)$$

The quantities A and B are the parameters which relate the changes in arc length on the surface while R_1 and R_2 are the first and second principal radius of curvature of the surface.

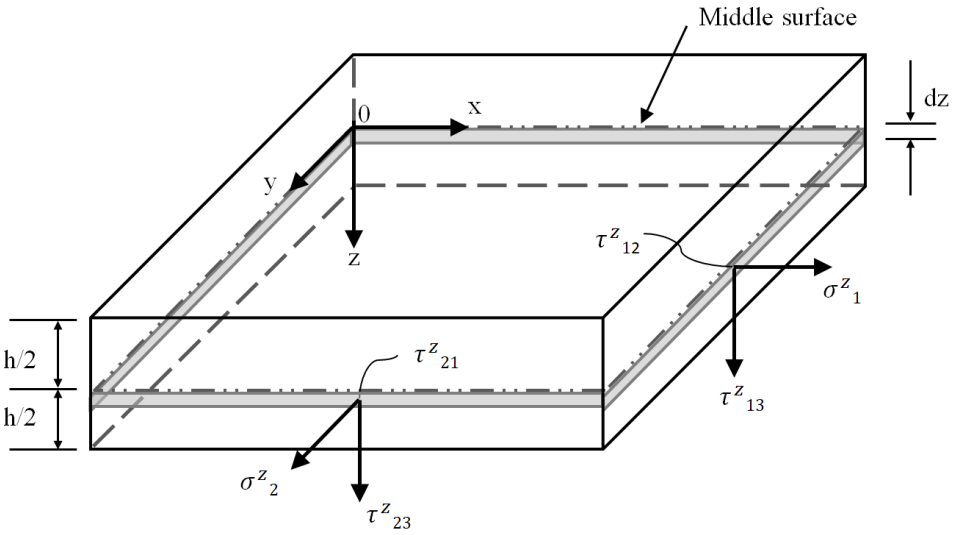

Figure 2.5 A differential element isolated from a shell [48].

The in-plane normal force N_1 referring to the resultant of the normal stresses σ_1 acting on the y-z plane per unit length of the element can be defined as:

$$N_1 = \int_{-h/2}^{h/2} \sigma_1^z \left(1 - \frac{z}{R_2}\right) dz \tag{2.10}$$

Similarly, the shear force N_{12} and the transverse shear force Q_1, referring to the resultants of the shear stress components τ_{12} and τ_{13}, acting on the y-z plane, can be defined as:

$$N_{12} = \int_{-h/2}^{h/2} \tau_{12}^z \left(1 - \frac{z}{R_2}\right) dz \tag{2.11}$$

$$Q_1 = \int_{-h/2}^{h/2} \tau_{13}^z \left(1 - \frac{z}{R_2}\right) dz \tag{2.12}$$

Therefore, the remaining stress components are given by the following in a similar manner:

$$N_2 = \int_{-h/2}^{h/2} \sigma_2^z \left(1 - \frac{z}{R_1}\right) dz \tag{2.13}$$

$$N_{21} = \int_{-h/2}^{h/2} \tau_{21}^z \left(1 - \frac{z}{R_1}\right) dz \tag{2.14}$$

$$Q_2 = \int_{-h/2}^{h/2} \tau_{23}^z \left(1 - \frac{z}{R_1}\right) dz \tag{2.15}$$

Then, the moments of the stress components σ_1^z and τ_{12}^z, referring to the x and y axes, are expressed as following:

$$M_1 = \int_{-h/2}^{h/2} \sigma_1^z z \left(1 - \frac{z}{R_2}\right) dz \tag{2.16}$$

$$M_{12} = \int_{-h/2}^{h/2} \tau_{12}^z z \left(1 - \frac{z}{R_2}\right) dz \tag{2.17}$$

which are referred to the bending and twisting moments acting on the y-z plane. Similarly, the stress couples or the bending and twisting moments on the x-z plane are:

$$M_2 = \int_{-h/2}^{h/2} \sigma_2^z z \left(1 - \frac{z}{R_1}\right) dz \tag{2.18}$$

$$M_{21} = \int_{-h/2}^{h/2} \tau_{21}^z z \left(1 - \frac{z}{R_1}\right) dz \tag{2.19}$$

These equivalent internal forces and moments at the middle surface are shown in Fig 2.6.

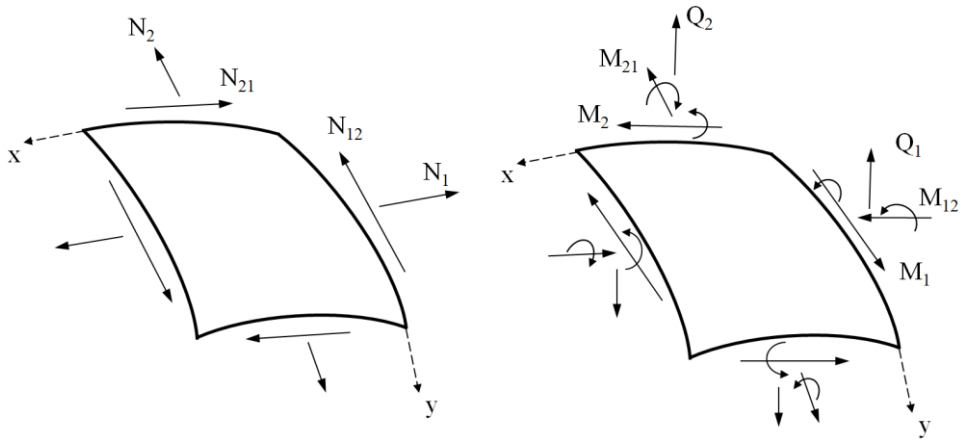

Figure 2.6 Equivalent internal forces and moments at the middle surface of the shell [48].

As presented above, six internal force, N_1, N_{12}, N_{21}, N_2, Q_1 and Q_2, and four moments, M_1, M_2, M_{12} and M_{21}, indicate the state of stress of the shell element in the general linear theory of thin shells. Therefore, the equilibrium conditions of the shell element at the middle surface can be

expressed by the external forces (p_1, p_2, p_3), internal forces and moments (the resultant force and moment of all the external and internal forces are zero) as following:

$$\frac{\partial}{\partial x}(N_1 B) + \frac{\partial}{\partial y}(N_{21} A) + N_{12}\frac{\partial A}{\partial y} - N_2\frac{\partial B}{\partial x} - Q_1\frac{AB}{R_1} + p_1 AB = 0,$$
$$\frac{\partial}{\partial y}(N_2 A) + \frac{\partial}{\partial x}(N_{12} B) + N_{21}\frac{\partial B}{\partial x} - N_1\frac{\partial A}{\partial y} - Q_2\frac{AB}{R_2} + p_2 AB = 0,$$
$$\frac{\partial}{\partial x}(Q_1 B) + \frac{\partial}{\partial y}(Q_2 A) + N_1\frac{\partial A}{\partial R_1} + N_2\frac{AB}{R_2} + p_3 AB = 0 \qquad (2.20)$$

$$\frac{\partial}{\partial x}(BM_{12}) + \frac{\partial}{\partial y}(AM_2) - M_1\frac{\partial A}{\partial y} + M_{21}\frac{\partial B}{\partial x} - Q_2 AB = 0,$$
$$\frac{\partial}{\partial y}(AM_{21}) + \frac{\partial}{\partial x}(BM_1) - M_2\frac{\partial A}{\partial x} + M_{12}\frac{\partial A}{\partial y} - Q_1 AB = 0,$$
$$N_{12} - N_{21} - \frac{M_{12}}{R_1} + \frac{M_{21}}{R_2} = 0 \qquad (2.21)$$

About the above equations, following equations can be set to reduce the number of unknowns:

$$M_{12} = M_{21} = H, \quad S = N_{12} + \frac{H}{R_2} = N_{21} + \frac{H}{R_1} \qquad (2.22)$$

Therefore, M_{12}, M_{21}, N_{12}, N_{21} can be replaced by H, S, R_1 and R_2. Meanwhile, Q_1, Q_2 in equations 2.21 also can be substituted into equations 2.20 to obtain three equations of equilibrium as following:

$$\frac{\partial}{\partial x}(N_1 B) + \frac{1}{A}\frac{\partial}{\partial y}(SA^2) - \frac{2}{R_2}\frac{\partial A}{\partial y}H - \frac{1}{R_1}\left[\frac{\partial}{\partial x}(M_1 B) - M_2\frac{\partial B}{\partial x} + 2\frac{\partial}{\partial y}(HA)\right]$$
$$-N_2\frac{\partial B}{\partial} + ABp_1 = 0,$$
$$\frac{\partial}{\partial y}(N_2 A) + \frac{1}{B}\frac{\partial}{\partial x}(SB^2) - \frac{2}{R_1}\frac{\partial B}{\partial x}H - \frac{1}{R_2}\left[\frac{\partial}{\partial y}(M_2 A) - M_1\frac{\partial A}{\partial y} + 2\frac{\partial}{\partial x}(HB)\right]$$
$$-N_1\frac{\partial A}{\partial y} + ABp_2 = 0,$$
$$N_1\frac{AB}{R_1} + N_2\frac{AB}{R_2} + \frac{\partial}{\partial x}\left\{\frac{1}{A}\left[\frac{1}{A}\frac{\partial}{\partial y}(HA^2) + \frac{\partial}{\partial x}(M_1 B) - M_2\frac{\partial B}{\partial x}\right]\right\}$$

$$+\frac{\partial}{\partial y}\left\{\frac{1}{B}\left[\frac{1}{B}\frac{\partial}{\partial}(HB^2)+\frac{\partial}{\partial y}(AM_2)-M_1\frac{\partial A}{\partial y}\right]\right\}+ABp_3=0 \tag{2.23}$$

Shell elements support external forces through the internal forces and moments. However, membrane elements transmit only in plane forces with no moments and have no stiffness in the bending direction considering as specific shell elements in three-dimensional models. Therefore, the moment terms in the equations of equilibrium for a shell element are neglected as following definition:

$$M_1=M_2=H=Q_1=Q_2=0\,;\quad N_{12}=N_{21}=S \tag{2.24}$$

To take Equation 2.24 into account Equation 2.23, the fundamental equations of the membrane element are:

$$\frac{\partial}{\partial x}(N_1B)+\frac{1}{A}\frac{\partial}{\partial y}(A^2S)-N_2\frac{\partial B}{\partial x}+ABp_1=0,$$

$$\frac{\partial}{\partial y}(N_2A)+\frac{1}{B}\frac{\partial}{\partial x}(B^2S)-N_1\frac{\partial A}{\partial y}+ABp_2=0,$$

$$N_1\frac{1}{R_1}+N_2\frac{1}{R_2}+p_3=0 \tag{2.25}$$

Membrane elements are used to represent thin structures such as a thin layer or sheet that offer strength only in the plane of the element with no bending stiffness. Since the balloon is made of soft polyester or nylon with small stiffness in the bending direction, membrane elements are suitable for the finite element model of the balloon.

A mesh model for the geometric balloon model was created in Abaqus/CAE 2018, a user interface for pre- and post-processing (Fig 2.7). The balloon model was meshed with four-node quadrilateral membrane element with reduced integration (Abaqus element type: M3D4R) with a uniform thickness of 0.02 mm. Each basic line in circumferential direction was divided to 200 numbers of element and lengthwise line were assigned with the seed size of 0.05 mm. The elements for the balloon model were 99,200 in total.

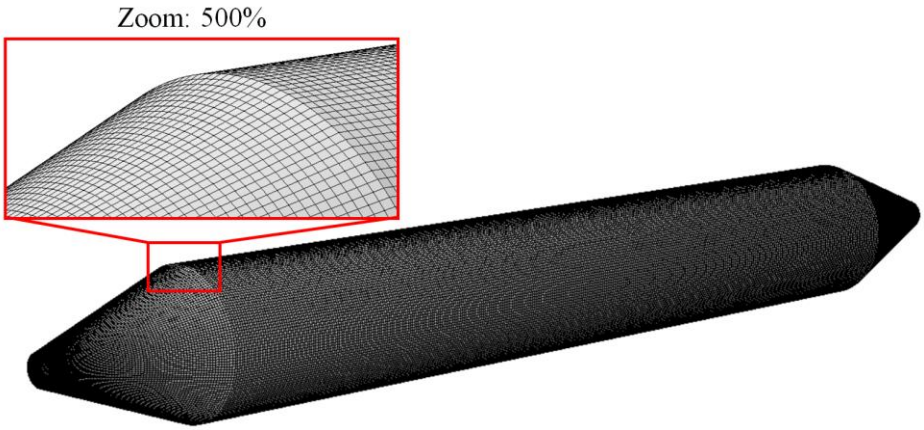

Figure 2.7 Mesh model for the balloon geometric model.

The isotropic elastic materials with Young's modulus of 706 MPa, Poisson's ratio of 0.4 and density of 1100 kg/m^3 were assigned to the balloon model. The two ends of the balloon model were full fixed in all degrees of freedom (X, Y, Z in translation and X, Y, Z in rotation) and pressure from 0 to 18 atm (0 to 1.824 MPa) was applied to the inner surface of the balloon model (Fig 2.8). The numerical simulation was carried out as a quasi-static analysis with Abaqus/Explicit solver.

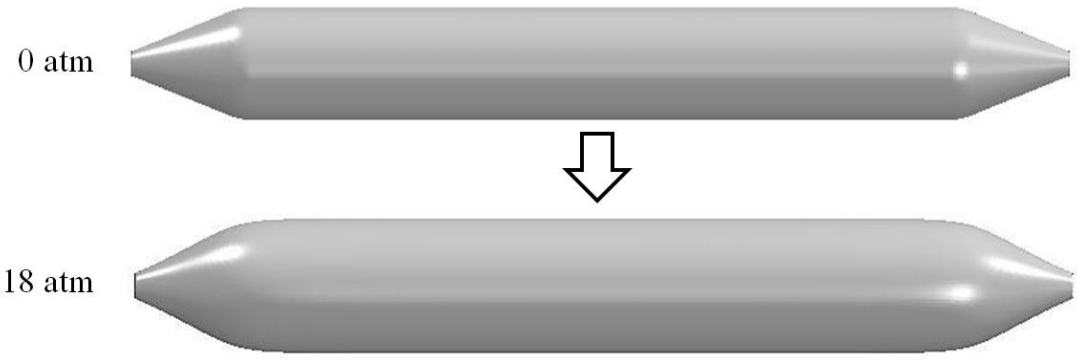

Figure 2.8 Expansion of the balloon model.

2.2.1.3 Quasi-static analysis in Abaqus/Explicit solver

The explicit method is a dynamic procedure to solve high-speed impact problems using quite

small minimum stable time increment and requiring a large number of increments in the solution. The inertial effect plays a primary role in the explicit method. The explicit method in Abaqus/Explicit has proven valuable in solving some quasi-static problems. The main advantage of the explicit method is the greater ease with that it solves very complicated contact problems in comparison with the implicit method. Additionally, the explicit method requires fewer resources for large models than the implicit method. However, a static event is a long-time dependent solution so that computationally, it is impractical to solve a static event in its natural time scale in the explicit solver. An excessive number of small time increments would be required in the explicit method. Therefore, the event must be accelerated in some way to get an economical solution. When the event is accelerated, the state of static equilibrium evolves into a state of dynamic equilibrium with more inertial effects. The strategy is to solve the problem in reasonable short time period with insignificant inertial effects.

To carry out a quasi-static analysis with the explicit method, three following main requirements should be guaranteed in Abaqus/Explicit solver.

(1) Estimating the time period in terms of the lowest natural frequency to obtain the proper static response. A frequency analysis showed that the balloon model had a fundamental frequency of 24.7 Hz, corresponding to a time period of 0.04 s.

$$\mathrm{T}_{analysis} > \frac{1}{f_{model(lowest\ natural\ frequency)}} \tag{2.26}$$

Therefore, the time period was determined to be 0.05 s which exceeded the time period calculated form the lowest natural frequency for the balloon model.

(2) Applying the load as smooth as possible to generate a smooth acceleration to avoid jerky changes in velocity and displacement. The most efficient way used in a quasi-static analysis is a definition for a smooth step amplitude curve. As shown in Fig 2.9, a smooth curve was defined instead of a typical uniformly increasing load. Expression 2.27 and 2.28 shows the definition for

the smooth curve between two points: (t_i, A_i) and (t_{i+1}, A_{i+1}).

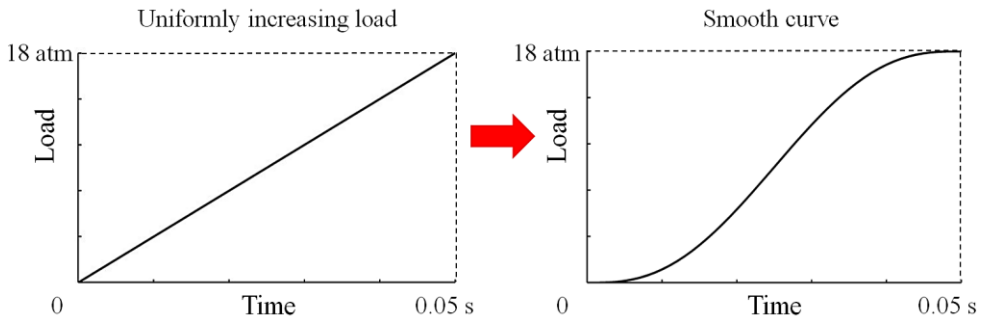

Figure 2.9 Definition of a smooth curve instead of a uniformly increasing load.

$$\mathrm{a} = A_i + (A_{i+1} - A_i)\varepsilon^3(10 - 15\varepsilon + 6\varepsilon^2) \qquad (t_i \le t \le t_{i+1}) \qquad (2.27)$$

$$\varepsilon = (\mathrm{t} - t_i)/(t_{i+1} - t_i) \qquad (2.28)$$

(3) For the deforming model, the kinetic energy should be within a 5% to 10% fraction of the internal energy throughout most of the process. Since the expansion simulation was carried out utilizing the simple initial balloon shape without any complex deformation or contact condition, in the result of the simulation, the kinetic energy almost was on the verge of zero. The inertial effect was insignificant in this analysis procedure (Fig 2.10).

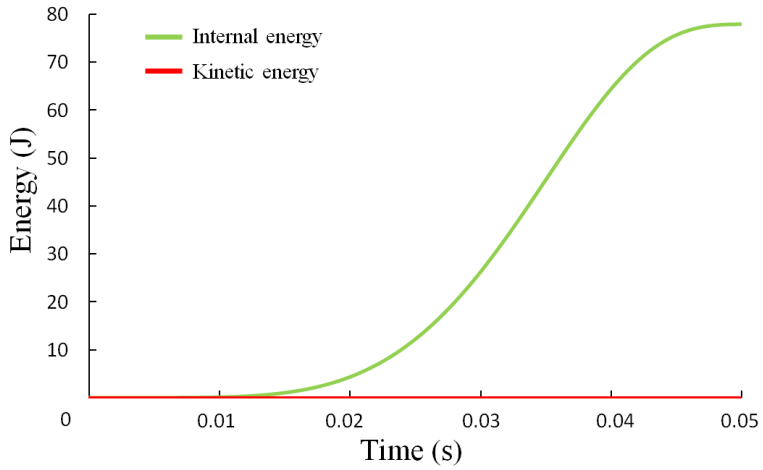

Figure 2.10 Elastic internal energy and kinetic energy in the balloon model.

2.2.1.4 Accuracy to the compliance chart

Figure 2.11 shows the diametral result of the radial displacement at the middle point of the balloon model was extracted to compare with the compliance chart in a diagram. Table 2.2 is the list for the difference at the pressure comparing with the compliance chart by the expression 2.29. All the values from 8 atm to 18 atm obtained from the numerical simulation showed good deviations with 2 % in which the maximum deviation was 1.85 % at the pressure of 8 atm. On the other hand, the mesh density also influences the numerical result. A worse mesh density and a finer mesh density were tested to confirm the accuracy. Table 2.3 shows the result of the tests. The current mesh density showed an extremely small deviation in comparison with a finer mesh density.

$$\text{Deviation} = \left| \frac{D_{numerical} - D_{compliance\ chart}}{D_{compliance\ chart}} \right| \times 100\% \qquad (2.29)$$

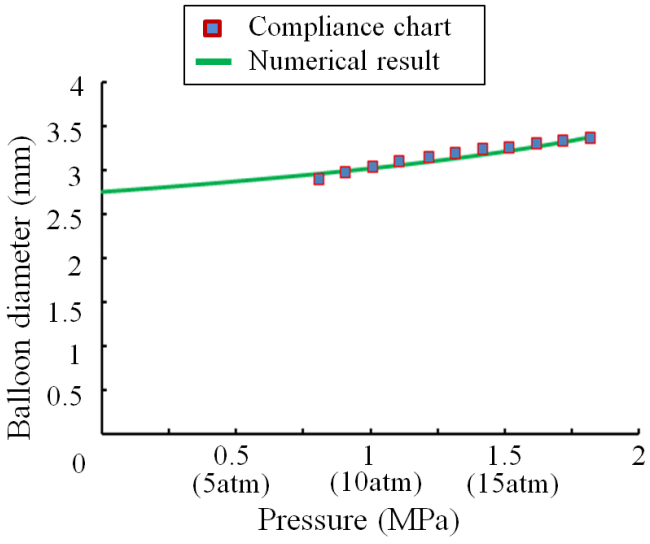

Figure 2.11 Diagram for the numerical result of balloon expansion in comparison with the compliance chart.

Table 2.2 List for the deviation of the numerical result in comparison with the compliance chart.

Xience V (Φ 3 mm x 18 mm)				
Pressure		Stent inner diameter	Balloon model diameter	Deviation
(atm)	(MPa)	(mm)	(mm)	%
8	0.81	2.90	2.9535	1.85
9	0.91	2.97	2.9862	0.55
10 (Nominal pressure)	1.01	3.04	3.0207	0.63
11	1.11	3.10	3.0569	1.39
12	1.22	3.15	3.0988	1.62
13	1.32	3.19	3.1387	1.60
14	1.42	3.23	3.1805	1.53
15	1.52	3.26	3.2239	1.10
16 (Rated burst pressure)	1.62	3.30	3.2693	0.93
17	1.72	3.33	3.3162	0.41
18	1.82	3.36	3.3649	0.15

Table 2.3 Result for the mesh density test of balloon model.

Mesh density	Coarser	current	finer
Size for one element (mm)	0.06	0.05	0.04
Element number	59,100	99,200	177,000
Radial displacement at nominal pressure (mm)	0.13518	0.13535	0.13547
Balloon diameter (mm)	3.0203	3.0207	3.0209
Deviation to the compliance chart (%)	0.648	0.635	0.628

2.2.1.5 Forming analysis for three-folded shape of balloon

A balloon catheter is wrapped from its initial shape to a three-folded shape through the processes of crimping and compressing. According to the balloon wrapper device, crimper models were created to pleat the balloon model. The details of the crimper models were shown in Fig 2.12. Five different curvature radiuses for the crimper models were defined to be 1.26 mm, 0.94 mm, 0.4 mm, 0.03 mm and 1.13 mm, respectively.

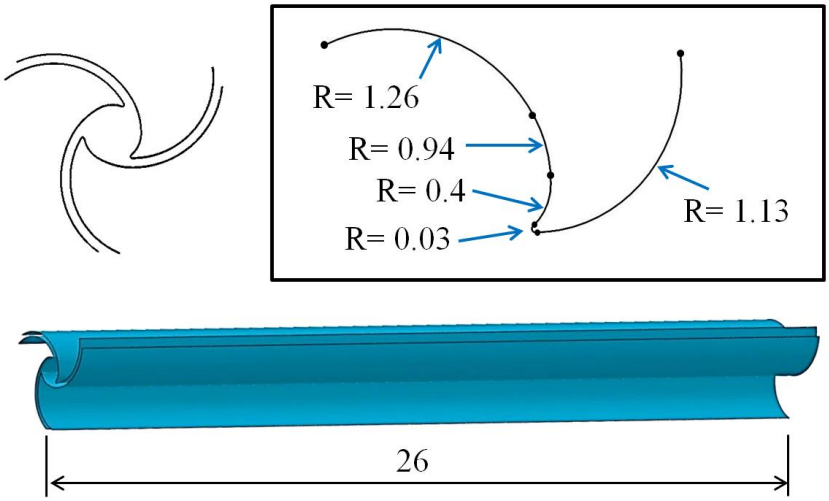

Figure 2.12 Three crimper models used to crimping the balloon model (Unit: mm).

The three crimper models were arranged around the balloon model and the displacements toward the center were applied to the crimper models (Fig 2.13a). Thereafter, a cylinder model was used to compress the crimped balloon model and decrease its diameter to 1 mm (Fig 2.13b). Since the membrane element has no bending stiffness, numerical unstable and convergence problems will occur when the membrane balloon model is crimped. Therefore, shell element type (S4R) was used to avoid numerical unstable and convergence problems to obtain a reasonable balloon shape (Fig 2.14). In order to confirm the accuracy again, balloon expansion simulation for the compressed balloon shape with membrane element type was performed and

the diametral result and deviations were illustrated in Fig 2.15 and Table 2.4. It is showed that the expanding result of the compressed balloon shape almost has no difference in comparison with that of the initial balloon shape.

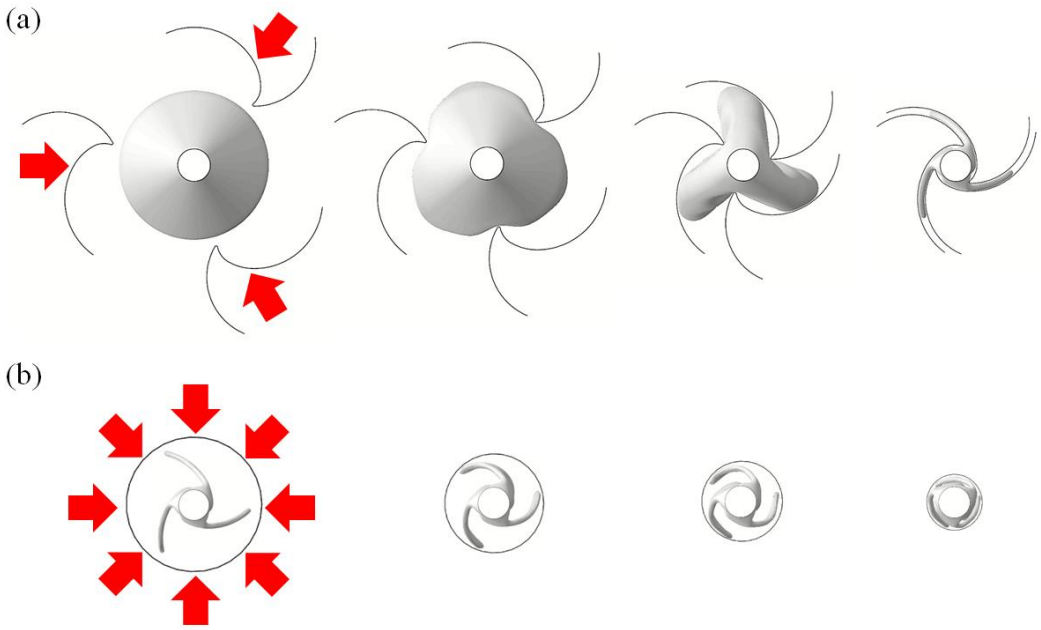

Figure 2.13 Process of three-folded balloon shape. (a) crimping (b) compressing.

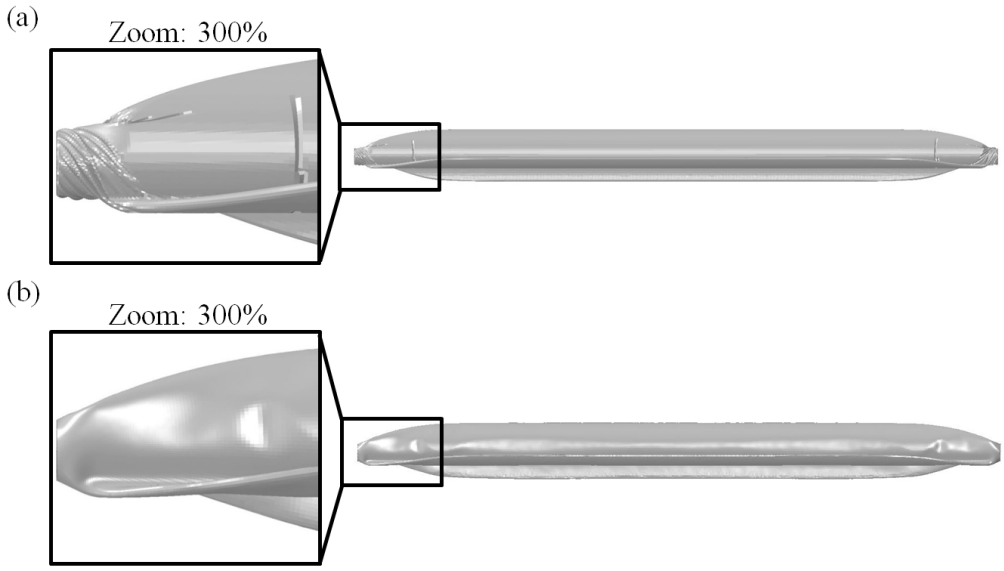

Figure 2.14 Crimping shapes of the balloon mesh model. (a) membrane element type; (b) shell element type.

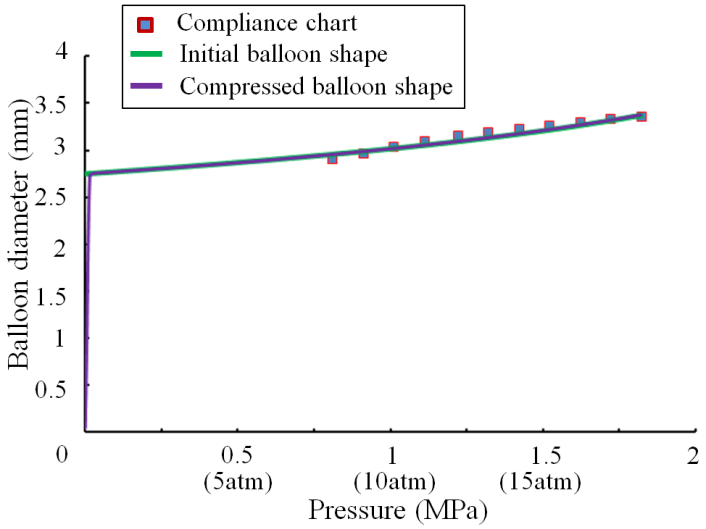

Figure 2.15 Expansion result of the diameter for the compressed balloon shape model.

Table 2.4 Deviation results for the compressed balloon shape.

Xience V (Φ 3 mm x 18 mm)						
Pressure		Stent inner diameter	Initial balloon shape		Compressed balloon shape	
(atm)	(MPa)	(mm)	Diameter (mm)	Deviation (%)	Diameter (mm)	Deviation (%)
8	0.81	2.90	2.9535	1.85	2.9539	1.86
9	0.91	2.97	2.9862	0.55	2.9846	0.49
10 (Nominal pressure)	1.01	3.04	3.0207	0.63	3.0172	0.75
11	1.11	3.10	3.0569	1.39	3.0529	1.52
12	1.22	3.15	3.0988	1.62	3.0949	1.75
13	1.32	3.19	3.1387	1.60	3.1354	1.71
14	1.42	3.23	3.1805	1.53	3.1783	1.60
15	1.52	3.26	3.2239	1.10	3.2238	1.11
16 (Rated burst pressure)	1.62	3.30	3.2693	0.93	3.2716	0.86
17	1.72	3.33	3.3162	0.41	3.3217	0.25
18	1.82	3.36	3.3649	0.15	3.3744	0.43

2.2.2 Coronary stent model

The initial balloon model and the wrapped balloon model of the Xience V coronary stent catheter were created and balloon expansion simulations were carried out to confirm the accuracy according to the compliance chart. An inflated balloon expands a coronary stent to enlarge the stenotic coronary artery and support the artery wall. Although a simple cylinder model is usually used to expand a stent model as a balloon, the wrapped balloon model should also be investigated to confirm its usefulness on the balloon-expandable stent and the difference from the cylinder model.

The three-dimensional geometric model of the Xience V coronary stent was created basing on its two-dimensional planar design drawing and generated through wrapping on a cylinder (Fig 2.16). The nominal diameter, length and strut thickness of the stent is 3 mm, 18 mm and 81 μm, respectively [49]. The initial pre-crimped external diameter of the stent is chosen equal to 1.8mm. The finite element model of the stent was meshed using eight-node hexahedral element (C3D8R) with six layers of elements through the thickness and width of the strut, about 700,000 elements in total (Fig 2.16).

An elastic-plastic material model of L605 cobalt-chromium alloy was assigned to the stent model. Young's modulus, Poisson's ratio, yield stress and density were listed in Table 2.5 [50]. The relationship of uniaxial-stress, plastic-strain and strain-rate is showed in Fig 2.17.

Isotropic elasto-plasticity is commonly utilized for metal plasticity calculations. The strain rate decomposition is:

$$\varepsilon = \varepsilon^{el} + \varepsilon^{pl} \tag{2.30}$$

In elastic-plastic analysis, the stress-strain matrix is modified to include the effects of plasticity basing on the classical flow theory with the von Mises yield condition. The von Mises

yield function is derived from the three dimensional stress-strain law with the appropriate stresses and strains set to zero. In von Mises plasticity, the stresses $S^{t+\Delta t}$ and the plastic incremental strains Δe^P are subjected to the yield condition, flow rule and hardening rule at time $t + \Delta t$:

$$F_y^{vonM\ t+\Delta t} = \frac{1}{2} S^{t+\Delta t} \cdot S^{t+\Delta t} - \frac{1}{3}\left(\sigma_y^{t+\Delta t}\right)^2 = 0 \tag{2.31}$$

Where $\sigma_y^{t+\Delta t}$ is the yield stress at time $t + \Delta t$. This stress is a function of the effective plastic strain and the hardening of the material is defined as follows.

$$\sigma_y^{t+\Delta t} = F_e(\bar{e}^{P\ t+\Delta t}) \tag{2.32}$$

with

$$\bar{e}^{P\ t+\Delta t} = \int_0^{t+\Delta t} \sqrt{\frac{2}{3} de^P \cdot de^P} \tag{2.33}$$

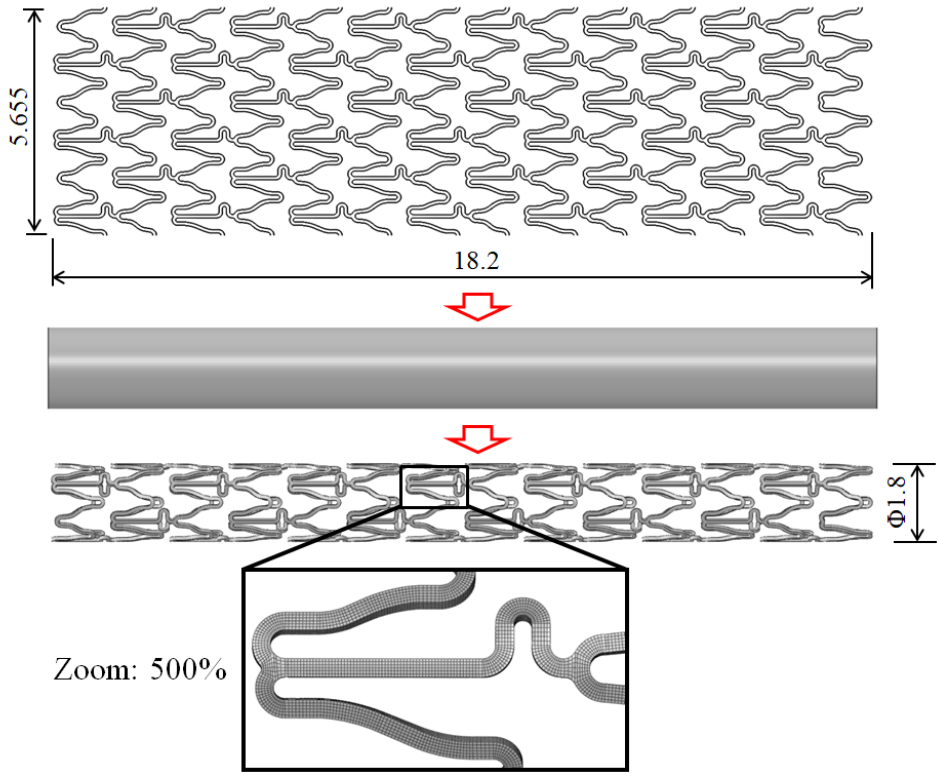

Figure 2.16 Process of the three-dimensional geometry and mesh model for the stent (Unit:

mm).

Table 2.5 Material properties for L605 cobalt-chromium alloy. [50]

Young's modulus (GPa)	243
Poisson' ratio	0.3
Density (g/cm^3)	9.1
Yield stress (MPa)	629
Stress (MPa) at 30 % strain	1089
Ultimate Tensile Strength (MPa) at 46 % strain	1147

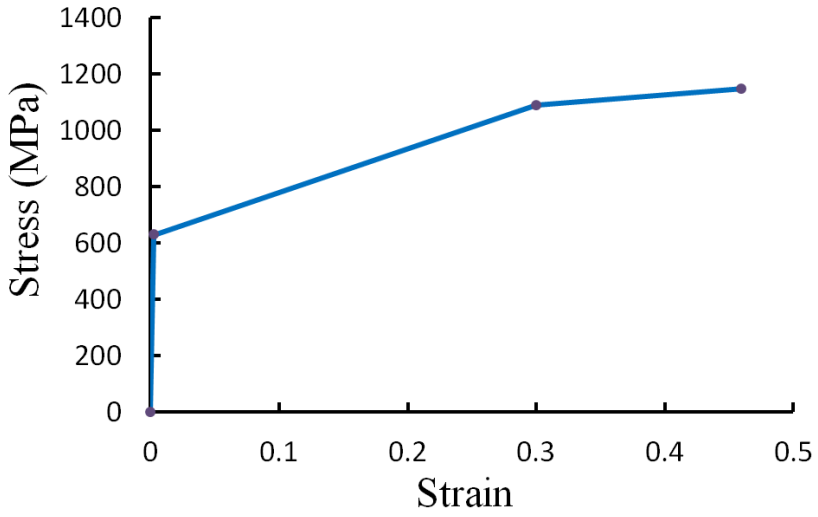

Figure 2.17 Stress-strain diagram for L605 cobalt-chromium alloy.

A simulation was carried out to generate a compressed stent model. A cylinder model which diameter was decreased by radial displacement was used to compress the outer diameter of the stent model from 1.8 mm to 1.2 mm so that the wrapped balloon model generated in Chapter 2.2.1.4 can be placed in the stent model (Fig 2.18).

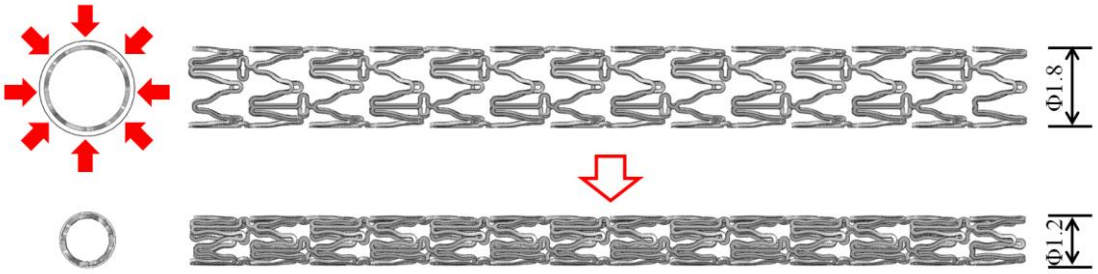

Figure 2.18 Compressing process of the stent model (Unit: mm).

2.2.3 Stenotic coronary artery model

A coronary artery model with an atherosclerotic plaque model inside was created. The length, thickness and inner diameter of the coronary artery model was 30 mm, 0.8 mm and 3 mm, respectively. The atherosclerotic plaque with a length of 14 mm and thickness of 0.75 mm was constrained at the middle of the coronary artery model via tie constraint. There is no separation and sliding between the artery model and the plaque model. The inner diameter of the plaque was equal to 1.5 mm which generating a 50 % stenotic lesion with the length of 10 mm (Fig 2.19).

The coronary artery model and plaque model were meshed using an eight-node hexahedral element (C3D8R) with approximately 72,000 elements and 36,720 elements

A study has determined and described the mechanical properties for human coronary non-atherosclerotic tissue [51]. Some studies described the atrial tissue models by Ogden or Mooney-Rivlin hyperelastic constitutive equations with three layers [52] [53] [54]. In the study of Prendergast et al [55], uniaxial and biaxial experiments on human femoral artery have been used to develop a hyperelastic constitutive model of vascular tissue suitable for implementation in finite-element analysis. It was discussed that the diseased coronary artery in which stents are implanted might be more silimar to human frmotal artery because those human tissues were

collected from elderly individuals of similar age to those undergoing coronary angioplasty and might be represent the in vivo case. Therefore, in this study, an isotropic Moony-Rivlin hyper-elastic material model was used to define the coronary artery model and the atherosclerotic plaque model. The strain energy density function was expressed as:

$$W = a_{10}\left(I_1 - 3\right) + a_{01}\left(I_2 - 3\right) \tag{2.34}$$

where I_1 and I_2 are the first and second invariants of the Cauchy–Green tensor and a_{10} and a_{01} are the hyperelastic constants listed in Table 2.6 [40] [55].

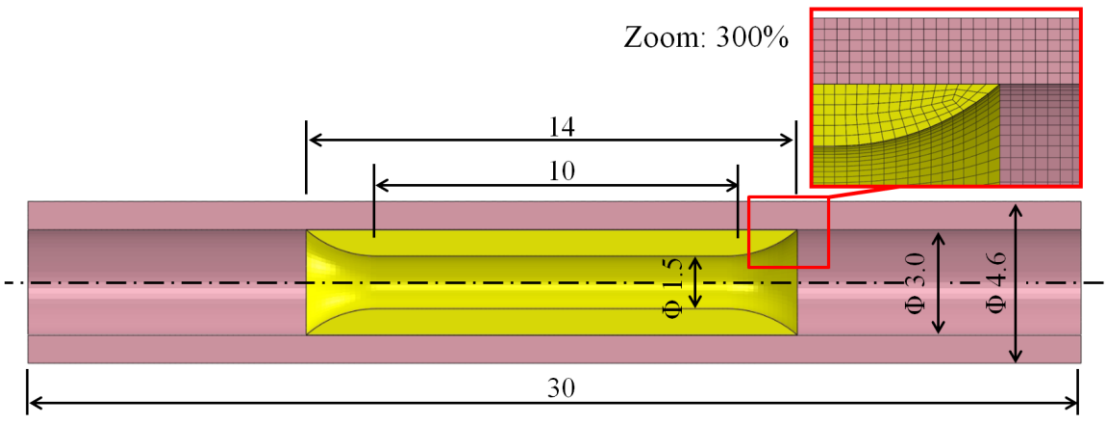

Figure 2.19 Geometry and mesh model for the coronary artery and plaque (Unit: mm).

Table 2.6 Material parameters of the coronary artery and atherosclerotic plaque. [40] [55]

Constants (MPa)	Coronary artery	Atherosclerotic plaque
a_{10}	0.01890	-0.496
a_{01}	0.00275	0.507

2.2.4 Expanding simulation of the coronary stent using the three-folded balloon

2.2.4.1 Free expansion of the coronary stent

The wrapped balloon model with a three-folded shape was created in Chapter 2.2.1 and its expanding accuracy was confirmed according to the compliance chart. A coronary stent catheter consists of a wrapped balloon, a shaft inside and a crimped stent so that it can be inserted in an artery. Therefore, a simulation of free expansion of a stent catheter with the coronary stent crimped on the balloon was carried out.

Fig 2.20 showed the stent catheter with three coaxial models of stent, balloon and shaft. The diameters for the shaft model, wrapped balloon and stent were 0.6 mm, 1 mm and 1.2 mm, respectively. The lengths for the shaft model, wrapped balloon and stent were 25 mm, 23.5 mm and 18.2 mm, respectively. There was no intersection in the three models.

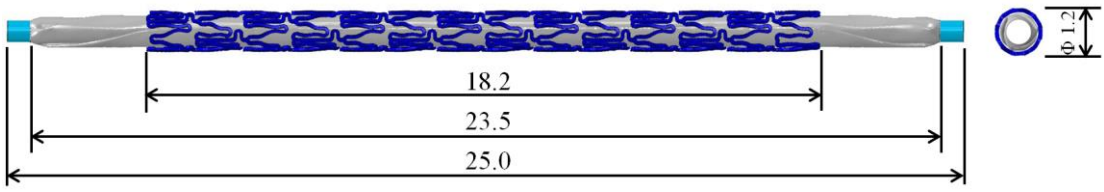

Figure 2.20 Stent catheter model with stent, balloon and shaft (Unit: mm).

Pressure from 0 MPa (0 atm) to 1.82 MPa (18 atm) increasing with a smooth curve was applied to the inner surface of the balloon model. The shaft model and the two ends of the balloon model were fixed during the expansion. The stent model was free during this expansion. The general contact algorithm available in Abaqus/Explicit was used to define the contact

conditions with friction coefficient of 0.2 in the three models. The expansion process of the stent was illustrated in Fig. 2.21.

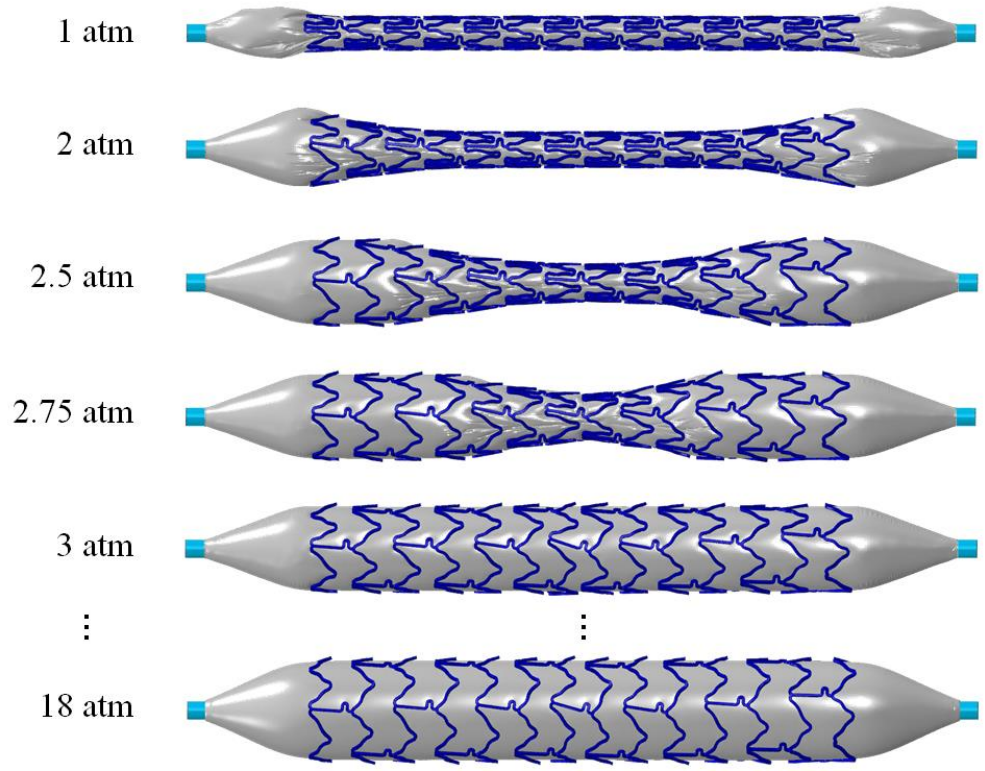

Figure 2.21 Expansion of the coronary stent model by the pressurized balloon model.

2.2.4.2 Balloon expansion and cylinder expansion of the coronary stent in a stenotic coronary artery model

The stenotic coronary artery model with plaque model inside was generated. The coronary stent catheter model was placed in the middle of the coronary artery model. To understand the difference between the balloon expansion and cylinder expansion and the reliability of the balloon, a cylinder surface model with a length of 20 mm and a diameter of 0.8 mm was created to expand the coronary stent model. Due to the diameter of the coronary artery model was 3 mm and the 50 % stenosis resulted in the 1.5 mm diameter, nominal pressure of 10 atm in the

balloon model and the radial displacement up to 3.0 mm diameter of the cylinder model was considered.

For the balloon expansion, pressure from 0 MPa (0 atm) to 1.01 MPa (10 atm) increasing with a smooth curve was applied to the inner surface of the balloon model. The two ends of the balloon model, the shaft model and the two end faces of the coronary artery model were fixed.

For the cylinder expansion, radial displacement was applied to the inner surface of the cylinder model to increase the diameter to 3 mm using a smooth curve. The cylinder model deformed only in the radial direction and the movement in the longitudinal translation was constrained. The two end faces of the coronary artery model were fixed. The expansion processes of the balloon and cylinder were illustrated in Fig 2.22 and Fig 2.23.

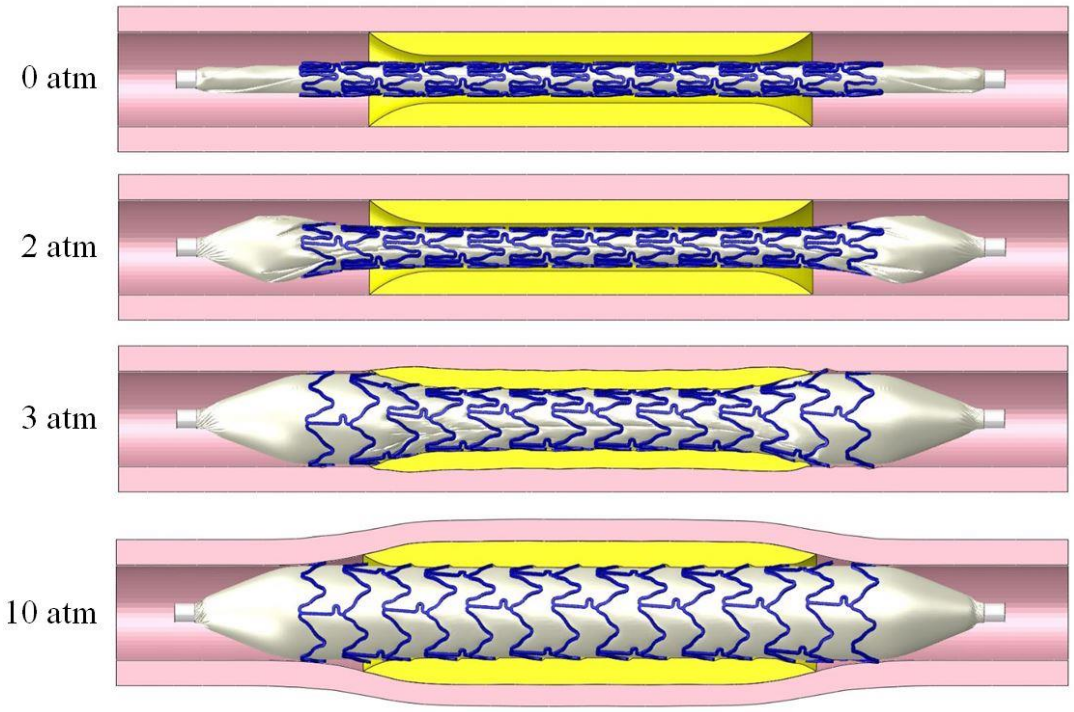

Figure 2.22 Process of the balloon expansion.

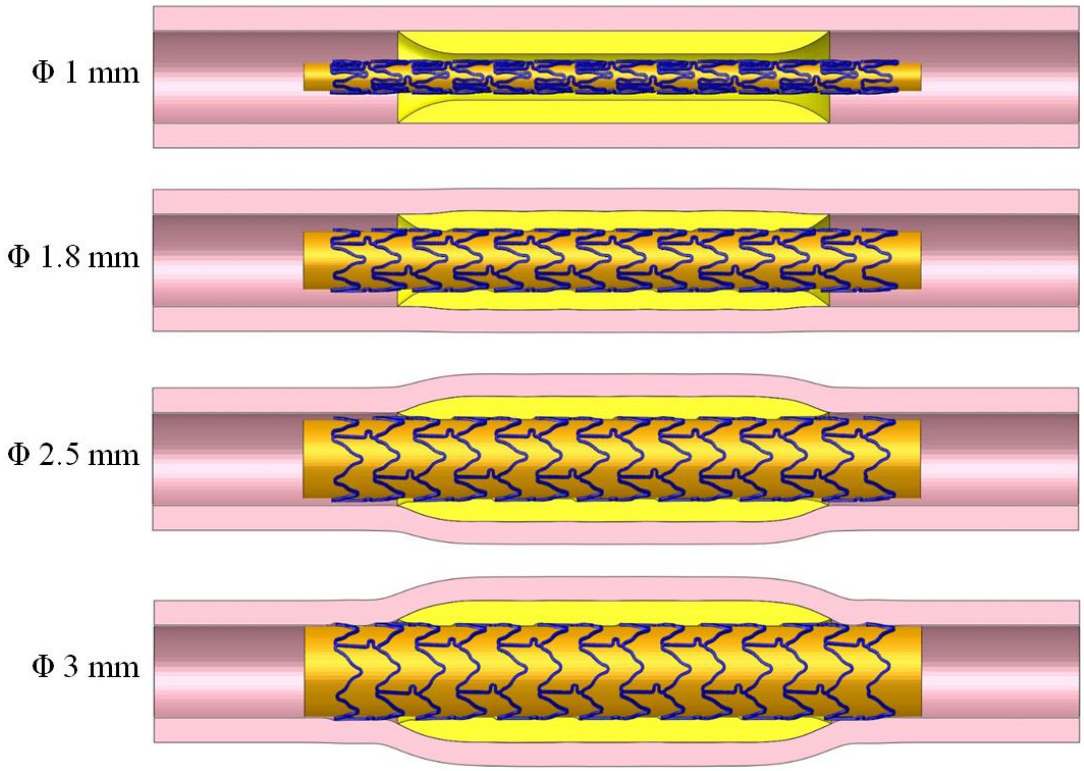

Figure 2.23 Process of the cylinder expansion.

2.3 Result

2.3.1 Free expansion of the coronary stent

In Fig 2.21, the two ends of the stent were first expanded at the initial pressurized stage since the stiffness of the middle part is higher than that of the ends. The entire stent model was fully expended at the pressure of 3 atm. The elastic internal and kinetic energy of the stent model are showed in Fig 2.24. Both peak values occurred at the pressure of 3 atm when the stent was fully expanded. The stent model was underexpanded with the “dogbone” shape before the pressure of 3 atm. Thereafter, the stent model was expanded slowly by the pressurized balloon model.

Isotropic hardening behavior occurred in the stent model with the increasing plastic stress and the elastic internal energy. The maximum kinetic energy of 0.27 J was extremely smaller than the maximum elastic internal energy of 15.44 J. The percentage of 1.75 % for the kinetic energy was under 5% to 10% fraction of the elastic internal energy, so that the inertial effect was not significant through the entire simulation.

To evaluate the equivalent stress level in the stent model, the von Mises stress that occurred in the stent model was illustrated in Fig 2.25.

The von Mises effective stress was calculated using following equation:

$$\sigma_{von\ Mises} = \sqrt{\frac{1}{2}\{(\sigma_{XX}-\sigma_{YY})^2+(\sigma_{YY}-\sigma_{ZZ})^2+(\sigma_{ZZ}-\sigma_{XX})^2\}+3(\tau_{XY}^2+\tau_{YZ}^2+\tau_{ZX}^2)} \qquad (2.35)$$

where, the σ_{XX}, σ_{YY}, σ_{ZZ}, τ_{XY}, τ_{YZ} and τ_{ZX} are stress components in the global coordinate system.

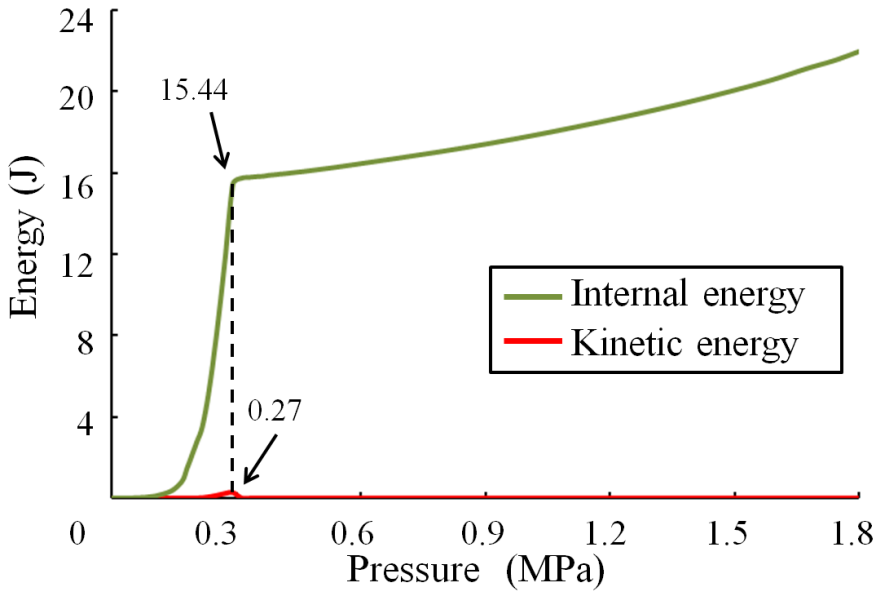

Figure 2.24 Internal and kinetic energy in the stent model during the expansion.

At the beginning of the expansion, the higher stresses occurred at the ends of the stent model due to the “dogbone” shape of the stent until the pressure of 3 atm. After the stent was fully expanded, the stress that occurred at the center strut of the stent model reached the same level of that occurred at the end strut of the stent model. The change of the stress at the center point showed a delay at the pressure of 3 atm (Fig 2.26).

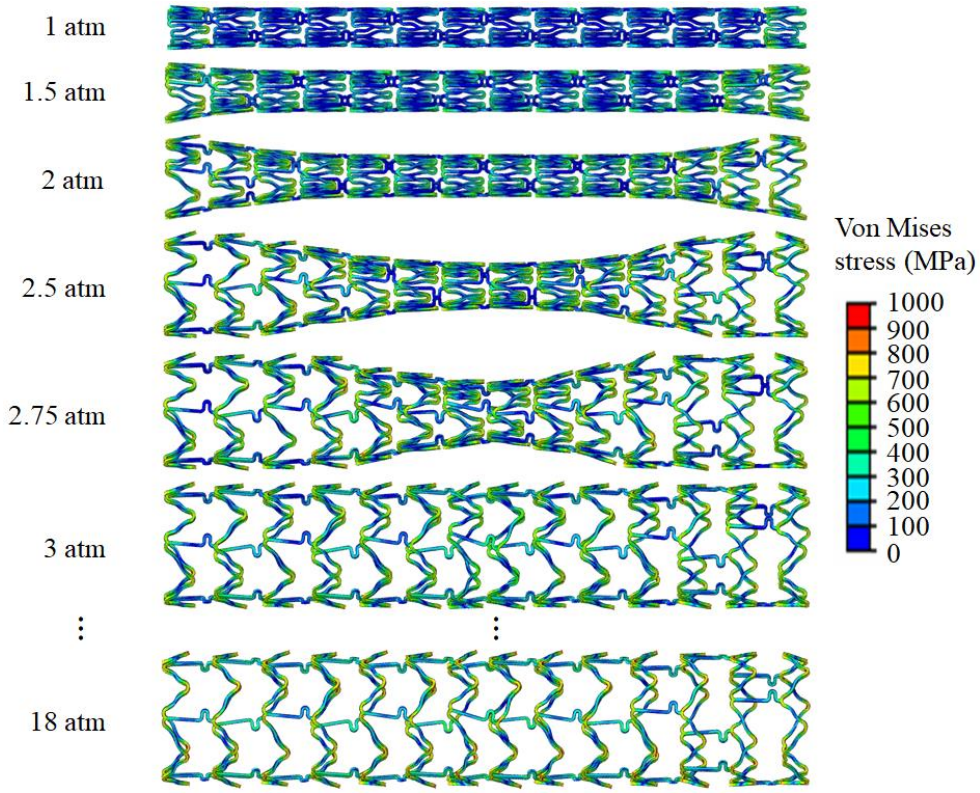

Figure 2.25 Stress plotted in the stent model.

On the other hand, high principal tensile stress was found at the inner curvature region with high value of von Mises stress showed in Fig 2.26. The values of the von Mises stress at the nominal press of 10 atm and the rated pressure of 16 atm are 1060 MPa and 1085 MPa. The values of the principal tensile stress at the nominal pressure of 10 atm and the rated pressure of 16 atm are 1082 MPa and 1109 MPa. The values of principal tensile stress are very close to the ultimate tensile strength of 1147 MPa. Crack induced by the high principal tensile stress might

occur on the surface of the stent strut during expansion.

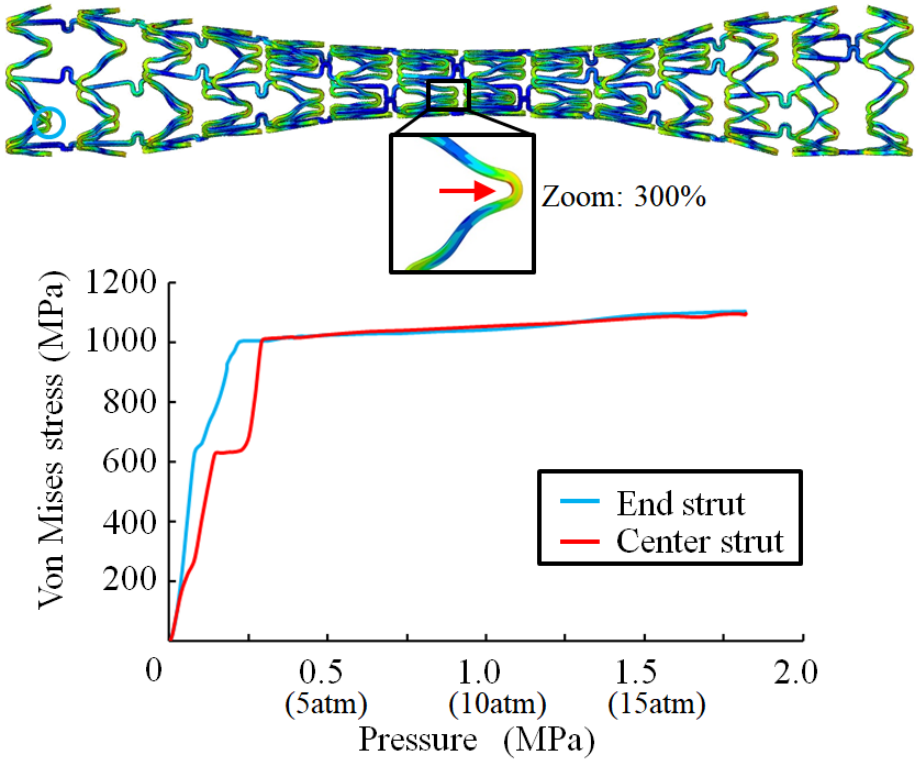

Figure 2.26 Stress changes for the center strut and the end strut of the stent model.

2.3.2 Expansion in the stenotic coronary artery model

Fig 2.27 showed the stress plotted stent model for the balloon expansion at the pressure of 10 atm and the cylinder expansion at the cylinder diameter of 3 mm. The inner diameters at the center of the stent models for the balloon expansion and the cylinder expansion were 2.958 mm and 3.013 mm, respectively. Fig 2.28 showed peak values of von Mises stress in the stent models for the balloon expansion and the cylinder expansion. Due to the different loads of the two simulations, the abscissa axis of the process was set to be 0 to 1. The process value of 1

represents the pressure of 10 atm for the balloon expansion and the cylinder diameter of 3 mm for the cylinder expansion. The peak value of the stress in the stent model for the balloon expansion was 1075.84 MPa and that for the cylinder expansion was 1034.02 MPa. The peak value for the cylinder expansion was 96.1 % of that for the balloon expansion.

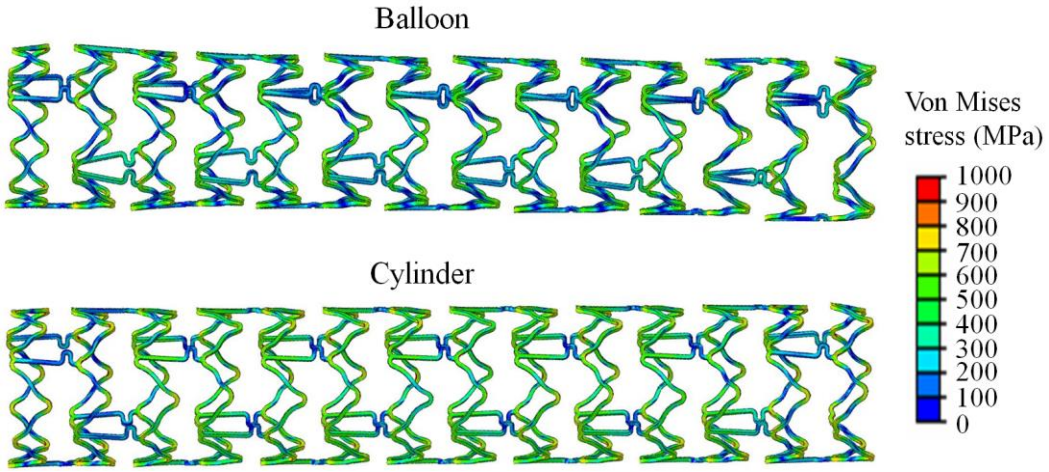

Figure 2.27 Stress in the stent models for the balloon expansion at 10atm and the cylinder expansion at 3 mm.

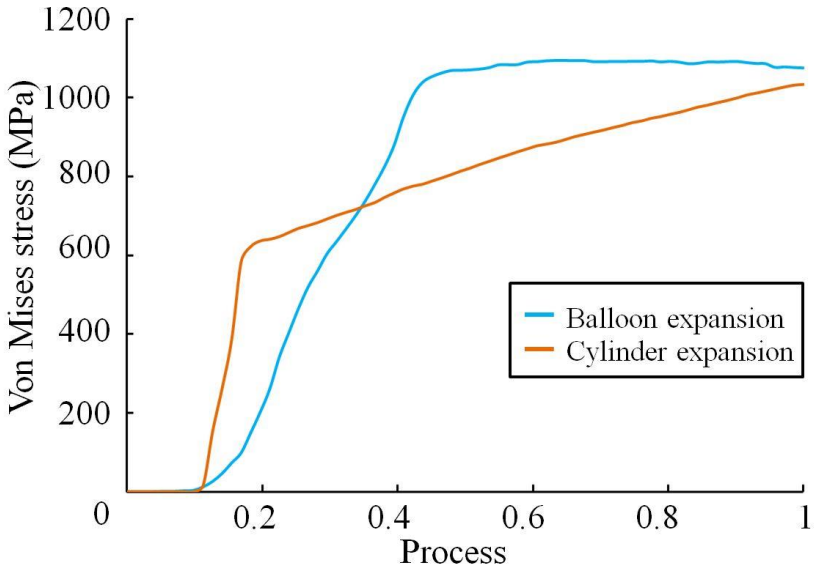

Figure 2.28 Peak values of stress in the stent models through the expansion process.

On the other hand, the maximum principal tensile stresses occurred in the plaque models for the balloon expansion at the pressure of 10 atm and the cylinder expansion at the cylinder diameter of 3 mm were illustrated in Fig 2.29. There are three principal stress components (minimum, intermediate, and maximum) with normal vectors (tensile and compression) calculated at each nodal point of the deformed part in the finite element analysis. In prior studies, high tensile stresses had been indicated as the primary inducement, which led to plaque fracture and damage in vessel wall when a balloon was inflated within a lesion [8] [56]. For this reason, the maximum principal tensile stress was used to describe the stress levels in the plaque models. Fig 2.30 showed peak values of maximum principal tensile stress in the plaque models for the balloon expansion and the cylinder expansion. The process was also scheduled to be 0 to 1. The peak value of the stress in the plaque model for the balloon expansion was 12.15 MPa and that for the cylinder expansion was 17.59 MPa. The peak value for the cylinder expansion was 144.8 % of that for the balloon expansion.

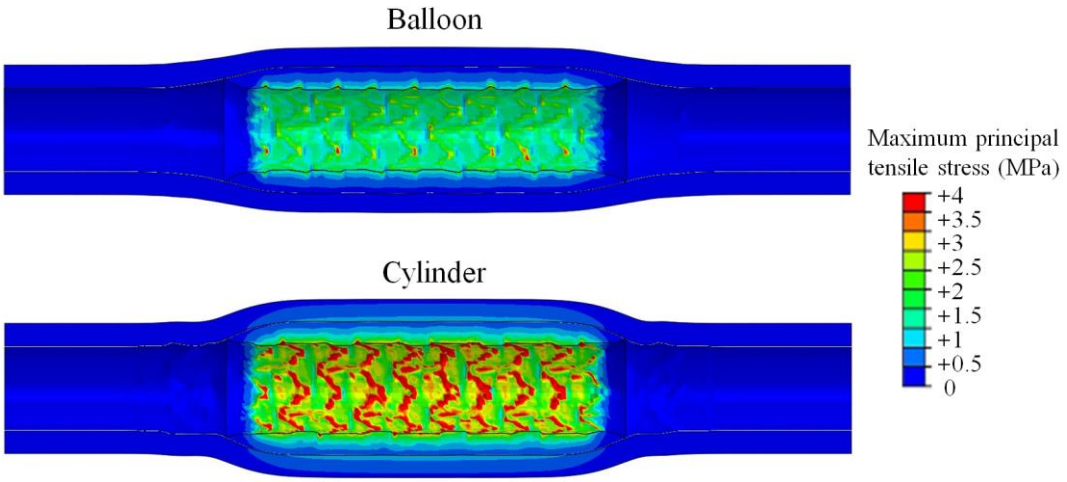

Figure 2.29 Stresses in the plaque models for the balloon expansion at 10 atm and the cylinder expansion at 3 mm.

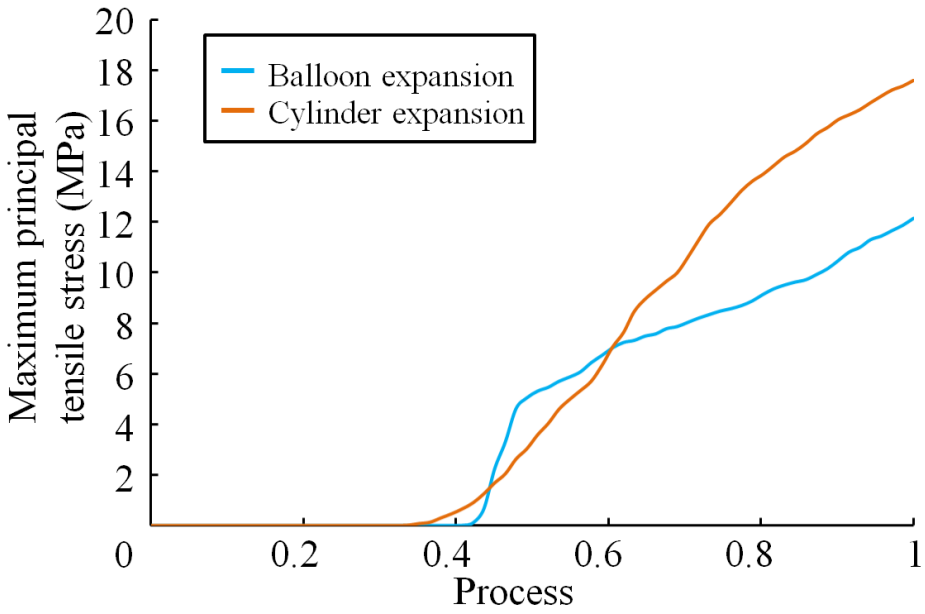

Figure 2.30 Peak values of stress in the plaque models through the expansion process.

2.4 Discussion

2.4.1 Three-folded balloon model

The length and shaft diameter of the initial balloon model was measured from the balloon catheter at the pressure of 1 atm. The initial diameter of the balloon was tested to obtain the best fit of Young's modulus through calculating the true stress and true strain from the compliance chart data. A simple expansion simulation of the initial balloon model was performed to confirm the accuracy comparing with the compliance chart and each corresponding value of the diameter was ensured within 2 % of deviation. Moreover, the three-folded wrapped balloon model was obtained through the crimping and compressing process from the initial balloon model. Thereafter, the result showed a similar deviation in comparison with the expansion of the initial balloon model. Although the actual inflation behavior of an angioplasty balloon is anisotropic

and hyperelastic, a linear isotropic balloon model can also adequately mimic the response of the balloon inflation within small deviations according to the compliance chart. This is an efficient method to generate the initial and wrapped balloon models.

2.4.2 Stent expansion

The coronary stent model was generated to confirm the free expansion of the stent model by the wrapped balloon model. The coronary stent model was expanded by the pressurized balloon model from 0 to 18 atm. The "dogbone" shape of the stent model was observed between 0 to 3 atm when the ends of the stent model were firstly expanded since the ends of the stent model were constrained by fewer neighboring struts. The stent model was fully expanded from 3 atm to 18 atm. The von Mises stress in the stent model also showed a delay at the point of the center strut in comparison with that of the end strut. The wrapped balloon model showed a feasible expansion for the coronary stent model.

The balloon expansion and cylinder expansion of the coronary stent in a stenotic coronary artery model were carried out and the differences were confirmed. The von Mises stresses occurred in the stent models were different during the expansion and the similar stresses for the balloon expansion at 10 atm and the cylinder expansion at 3 mm. The inner diameter of the stent model for the balloon expansion was smaller than that for the cylinder expansion. Since the radial displacement was applied to the cylinder surface model, the inner diameter of the stent model was more accurate. However, for the balloon expansion, the balloon model was enlarged by the load of pressure on the inner face and the diameter was slightly influenced by the resistance from the surrounding plaque model and artery model. On the other hand, the peak value of maximum principal tensile stress in the plaque model for the cylinder expansion was

higher than that for the balloon expansion at the process of 1. Since the radial displacement was applied to the cylinder surface model, it generated the high stiffness of the cylinder surface and overcame the resistance of the plaque model and artery model during expansion resulting in the higher stress level in the plaque model. It is understood that the balloon expansion using the wrapped balloon model showed a more realistic response to an actual balloon catheter and more reliable stress in the plaque model in comparison with the cylinder expansion.

2.5 Conclusion

In this chapter, the author measured the dimensions of the balloon to create an initial balloon model and accomplished the following contents:

(1) established crimping and compressing processes to generate a three-folded balloon model and verified the accuracy of the balloon expansion in comparison with the compliance chart.

(2) simulated a stent free expansion and stent expansion in a stenotic coronary artery model by the three-folded balloon model and comparing with a cylinder expansion to verify the efficacy of the three-folded balloon model and revealed the different between the balloon expansion and cylinder expansion of the stent.

It is an efficient method to obtain the wrapped balloon model and the accuracy was assured. The wrapped balloon model showed a good response to expand a coronary stent model and a more realistic effect on the plaque model than the expansion using a cylinder surface model with high stiffness. The method of generating a wrapped balloon model can be utilized to create a cutting balloon model with blades on the balloon surface described in the next chapter.

Chapter 3: Investigation of balloon-to-artery ratio of cutting balloon in 360º calcified artery model

3.1 Chapter introduction

In this chapter, the author investigates the influence of the balloon-to-artery ratio on expanding the cutting balloon in a calcified artery model. The cutting balloon angioplasty is a crucial procedure to deal with the calcified lesion before stent implantation. For cutting balloon expansion, a balloon-to-artery ratio of 1:1 is used like conventional balloon angioplasty. Little is known how the balloon-to-artery ratio for the cutting balloon influences both effective incision of the calcification and potential perforation or dissection [57].

The aims of this chapter are listed as follows:

(1) to generate the cutting balloon model with blades on the balloon surface by means of the modeling of the three-folded balloon expansion described in Chapter 2.

(2) to simulate the expansion of the cutting balloon with different diameters in a 360 degrees calcification model inside a straight coronary artery model.

A conventional non-compliant balloon is employed to understand the effects of blades for fracturing calcification.

The author investigates the influences of balloon-to-artery ratios of the cutting balloon on the stress concentrations and distribution in the calcified model and at the borders of the coronary artery adjacent to the calcification to obtain a criterion for the balloon-to-artery ratio for the cutting balloon. This may be helpful to understand the function of the blades on the balloon and

the importance of the balloon-to-artery ratio in the cutting balloon angioplasty [57].

3.2 Materials and methods

3.2.1 Geometries and mesh models

This chapter evaluated a new-generation cutting balloon, Wolverine^{TM} (Boston Scientific Corporation, MA, USA), with superior crossability and deliverability in comparison with the older cutting balloon (Flextome^{TM}, Boston Scientific Corporation, MA, USA) [57]. The length of the balloon body, total length and the diameter of the inner shaft were measured basing on the image of the cutting balloon catheter (Fig 3.1). The relationships of the diameter and the inflation pressure for the cutting balloon with balloon diameters ranging from 2 to 3 mm (2, 2.25, 2.5, 2.75, and 3 mm) are listed in Table 3.1. The nominal pressure and rated pressure for the cutting balloon are 6 atm and 12 atm, respectively [57].

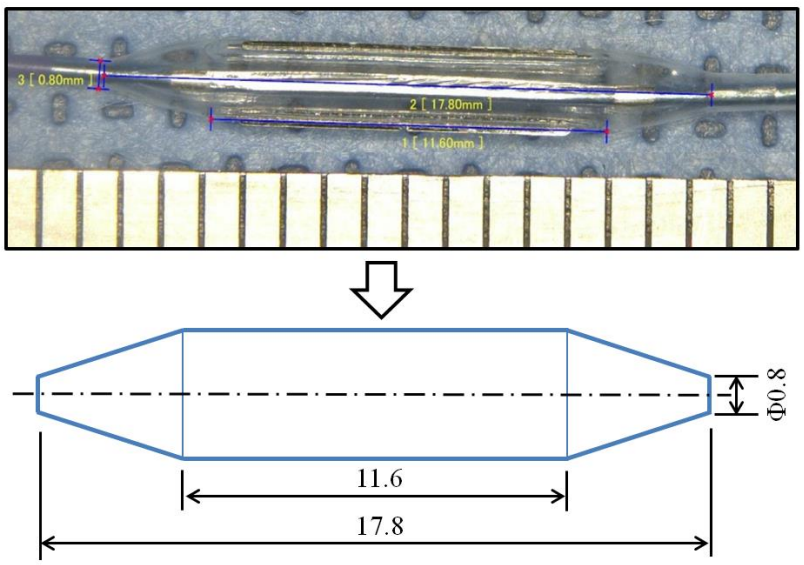

Figure 3.1 Image and dimensions for the cutting balloon catheter (Unit: mm).

Table 3.1 Compliance chart and the result by Finite element analysis for the cutting balloons.

Pressure		Balloon diameter (mm)									
		Product data provide by the manufacturer					Finite element analysis				
atm	MPa	2	2.25	2.5	2.75	3	2	2.25	2.5	2.75	3
3	0.304	1.90	2.14	2.38	2.62	2.88	1.89	2.13	2.37	2.61	2.88
4	0.405	1.95	2.18	2.43	2.69	2.94	1.92	2.16	2.40	2.65	2.92
5	0.507	1.98	2.22	2.48	2.73	2.99	1.95	2.19	2.44	2.69	2.96
6	0.608	2.02	2.26	2.52	2.78	3.06	1.98	2.23	2.47	2.73	3.00
7	0.709	2.05	2.30	2.56	2.83	3.10	2.01	2.26	2.51	2.78	3.05
8	0.811	2.08	2.33	2.60	2.88	3.15	2.05	2.30	2.56	2.83	3.10
9	0.912	2.11	2.36	2.64	2.91	3.18	2.08	2.34	2.60	2.88	3.15
10	1.013	2.13	2.39	2.67	2.95	3.22	2.12	2.39	2.65	2.94	3.20
11	1.115	2.15	2.41	2.69	2.97	3.25	2.17	2.44	2.70	2.99	3.26
12	1.216	2.17	2.44	2.71	3.00	3.28	2.21	2.49	2.75	3.06	3.32

A typical non-compliant balloon (NC EmergeTM balloon, Boston Scientific) was utilized to compare with the cutting balloon to investigate the effects of the blades in this chapter. The compliance chart of the non-compliance balloon is listed in Table 3.2. The nominal pressure and rated pressure for the non-compliant balloon are 12 atm and 20 atm, respectively [57].

Chapter 2.2.1 described a linear isotropic membrane balloon model with an initial diameter and Young's modulus obtained from the product compliance chart. The relationship between the pressure and diameter of the balloon model obtained by finite element analysis has been verified to be in accordance with the compliance chart within a deviation of 2% listed in Table 3.1 and

Table 3.2 Compliance chart and the result by Finite element analysis for the Non-compliant balloon.

Non-compliant balloon (Φ 3 mm x 10 mm)			
Pressure		Balloon diameter (mm)	
		Product data provide by the manufacturer	Finite element analysis
(atm)	(kPa)		
3	304	2.65	2.68
4	405	2.71	2.74
5	507	2.76	2.81
6	608	2.81	2.83
7	709	2.86	2.90
8	811	2.90	2.92
9	912	2.93	2.94
10	1013	2.96	2.97
11	1115	2.99	2.98
12	1216	3.01	2.99
13	1317	3.03	3.01
14	1419	3.04	3.03
15	1520	3.06	3.05
16	1621	3.08	3.07
17	1723	3.09	3.08
18	1824	3.10	3.10
19	1925	3.12	3.11
20	2027	3.13	3.12

3.2. Therefore, in Table 3.3, the initial diameters and Young's moduli of five different cutting balloon diameters (2.0, 2.25, 2.50, 2.75, and 3.0 mm), as well as the 3.0-mm non-compliant

balloon with a length of 12 mm were analyzed using the data of the compliant charts [57]. Approximately 100,000 four-node quadrilateral membrane elements (element type: M3D4R) were employed to the balloon model. A density of 1100 kg/m^3 and a uniform 0.02 mm wall thickness were assumed [37].

Table 3.3 Initial diameters and Young's moduli of the balloons. [57]

	NC balloon	Cutting balloon				
Balloon diameter (mm)	3.0	2.0	2.25	2.50	2.75	3.0
Initial diameter (mm)	2.71	1.83	2.05	2.28	2.52	2.79
Young's modulus (MPa)	908	338	365	419	447	534

NC: non-compliant

Wolverine cutting balloons with diameters smaller than 3.25 mm (2.0 mm, 2.25 mm, 2.50 mm, 2.75 mm and 3.0 mm) have three sharp metal microsurgical blades bonded on cast pads. The blades and cast pads are fixed longitudinally on the outer surface of the balloon (Fig 3.1). Those cutting balloon devices with diameters of 3.5 mm and 4.0 mm have four blades on the balloon [57].

When the cutting balloon is wrapped under the folded shape before expansion, the three blades are ensconced inside the folds of the wrapped balloon. The blades will expand out radially during inflation and make incisions in the calcified plaque [57].

The three-dimensional computer-aided-design (CAD) geometrical model of the metal microsurgical blade was constructed with length of 8.8 mm, height of 0.25 mm, and width of 0.18 mm (Fig 3.2) [57].

Considering the convergence problem and stress concentration due to the contact between the

blade model and the calcification model, the mesh density for the blade model was confirmed. The strategy of the mesh model for the blade geometric model was considered to using eight-node hexahedral elements with reduced integration (element type: C3D8R) instead of the tetrahedral elements. Generally, the hexahedral elements are superior to the tetrahedral elements because:

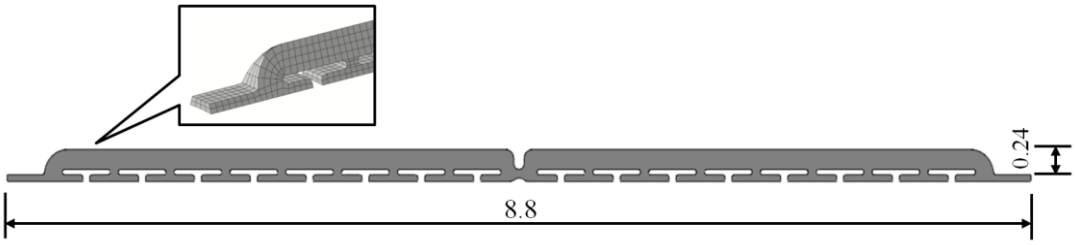

Figure 3.2 Geometric model of the blade (Unit: mm). [57]

(1) high quality structured hexahedral elements can be created easily by mapping, sweeping and extrusion techniques.

(2) hexahedral elements can be constructed following the domain boundary in layers and in alignment with geometrical features.

(3) low-order high-performance hexahedral elements are more computationally efficient than the tetrahedral elements.

A test simulation was considered to confirm the convergence and the accuracy of the stress occurred in the blade model. Pressure from 0 to 1 MPa was applied to the bottom surfaces of the blade model. A calcification model with a portion of 60º was created upside the blade model. Then, the blade model was bent to contact with a calcification model (Fig 3.3).Half of the length was considered in the simulation and the longitudinal end surface of the blade model and the entire calcification model were fixed. The mesh densities of the blade model were confirmed by

coarser mesh, current mesh and finer mesh. The results of convergence were confirmed for the three mesh densities and the results of the Y-direction displacement at the longitudinal end point and the peak values of von Mises stress and maximum principal stress were confirmed and listed in Table 3.4. The results of the current mesh density shows the closer values to the finer mesh density without any problem of convergence.

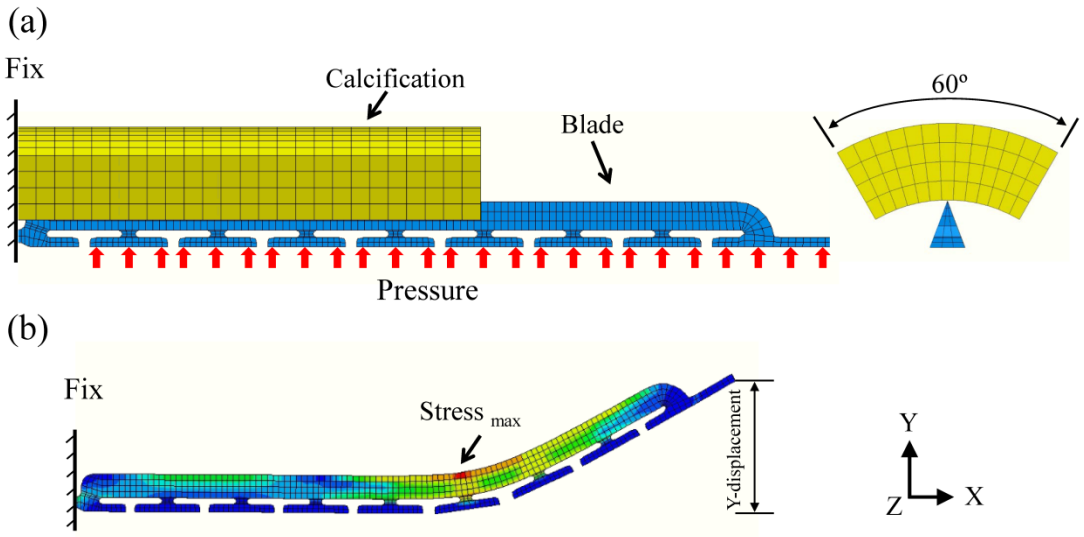

Figure 3.3 Bending simulation of the blade model. (a) the models and boundary condition. (b) Y-displacement and max stress of the deformed blade model.

Table 3.4 Results for the mesh density test of the blade model.

Mesh density	coarser	current	finer
Size for one element (mm)	0.05	0.04	0.02
Element number	3,970	6,250	12,270
Y-displacement at 1 MPa	0.73	0.84	0.86
Peak value of von Mises stress (MPa)	437.3	507.2	509.8
Peak value of maximum principal stress (MPa)	+681.5	+707.3	+716.6

Therefore, in this study, the geometric model of the blade was discretized using 6,250

eight-node hexahedral elements with reduced integration (element type: C3D8R). The metal blade is made of 316L stainless steel and the material properties of Young's modulus of 193 GPa, Poisson ratio of 0.3, density of 7950 kg/m^3, yield stress of 366 MPa, and ultimate tensile strength of 675 MPa were utilized and considered as an elastic-plastic model with isotropic hardening [50].

The three-dimensional structure of the cast pad was created with length of 9.2 mm, height of 0.1 mm, and width of 0.58 mm (Fig 3.4). The cast pad model was employed approximately 32,380 eight-node hexahedral elements (element type: C3D8R). Elastic behaviors with Young's modulus of 441 MPa, Poisson ratio of 0.3 and density of 1100 kg/m^3 were assigned to the cast pad model [57].

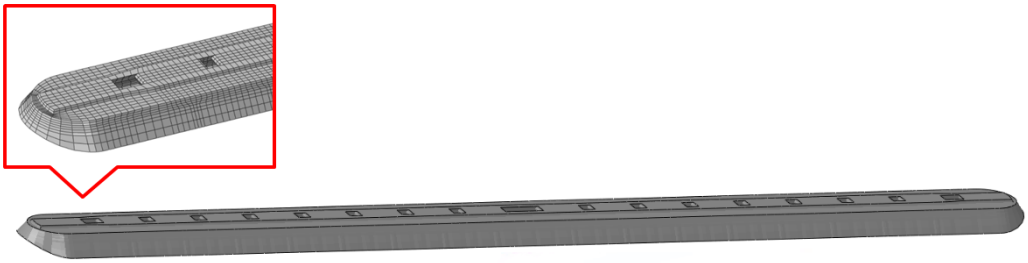

Figure 3.4 Geometric model of the cast pad.

Additionally, an inner shaft in the balloon catheter was created as a rigid cylindric model with a diameter of 0.8 mm and a length of 18 mm along the center axis of the balloon model [57].

A clinical study reported that 60% of calcium fractures (18 of 30) with large calcium arcs from 270 to 360 degrees were observed in coronary artery lesions when only conventional balloon angioplasty was used prior to stent implantation and detected that the minimum threshold of calcium thickness for calcium fracturing was 0.24 mm [46][57]. Another clinical study reported that the median calcium fracture thickness was 0.45 mm in coronary lesions with cutting balloon angioplasty or rotational atherectomy [57][58]. Furthermore, intravascular

ultrasound examinations showed that the target lesion calcium length of ≤ 5 mm was most frequently detected and the mean length of calcium was 3.5 ± 3.7 mm in patients [57][59]. In a randomized controlled trail, lumen diameter reduction of ≥ 50 % (50% diameter stenosis) in severely calcified lesions is considered the main inclusion criteria of lesion modification [24][57].

Therefore, the calcified coronary artery was modeled with 50% moderate stenosis in diameter, 24 mm length, 3 mm inner diameter, and 0.8 mm thickness [57]. In the calcified artery model, a 360 degree calcification model with 0.4 mm thickness and 5 mm length was incorporated and constrained via tie constraint in Abaqus/CAE (tying the adjacent two surfaces of calcification and artery models together) [57]. The coronary artery model was meshed using the eight-node hexahedral element (element type: C3D8R) with approximately 400,000 elements. Approximately 20,000 C3D8R elements were used to mesh the 360 degree calcification model (Fig 3.5) [57].

A hyperelastic material of the Mooney-Rivlin model was assumed to describe the mechanical behavior of the artery model as described in Chapter 2.2.3 [55]. Thermogravimetry and X-ray diffraction analyses of human aortic wall calcification have shown that the calcified spots in the aortas had similar compositions and particle size of calcium phosphate minerals compared to human bone samples [60].

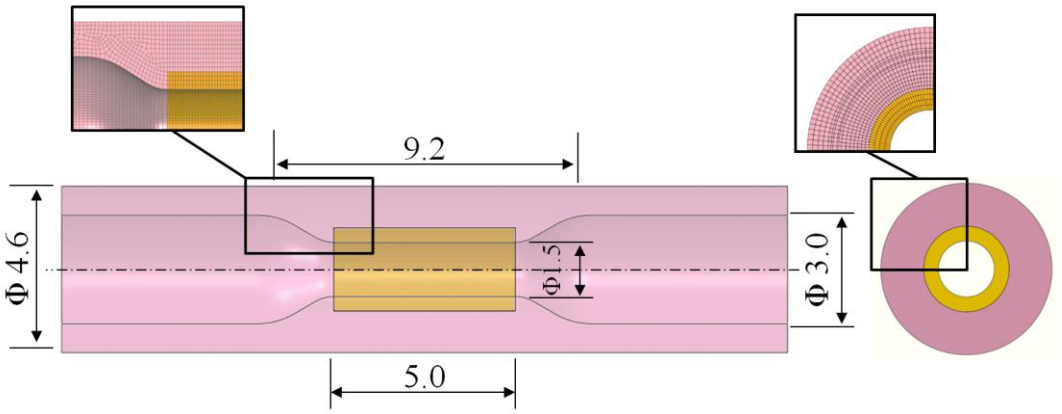

Figure 3.5 Geometric models for the coronary artery and calcification (Unit: mm). [57]

A nanoindentation study reported that Young's modulus for human calcified plaques collected from the superficial femoral artery wall was 20.1 GPa [43]. Another nanoindentation study showed that the majority of Young's modulus was within the range of 100 MPa to 10 GPa of human carotid bifurcation plaque and some as high as 21 GPa [61]. The sample preparation, variations in tissue composition and incomplete mineralization were considered as the causes of the variations. Moreover, in their follow-up study, Young's modulus of calcification with reducing the cause of these potential errors ranged from 15 to 25 GPa was in agreement with their observation of 21GPa [62]. Therefore, in this study, the calcification model was assumed to be an elastic isotropic material model with Young's modulus of 20.1 GPa and Poisson ratio of 0.3 [57].

3.2.2 Modeling of the three-folded balloon

As described in Chapter 2.2.1.4, a balloon catheter is wrapped in a folded shape before expansion. The cutting balloon catheter is radially folded and the blades are ensconced inside the folds of the wrapped balloon. The folding process for the cutting balloon was conducted to generate the three-folded shape. First, three rigid surface models were created and showed in Fig 3.6.

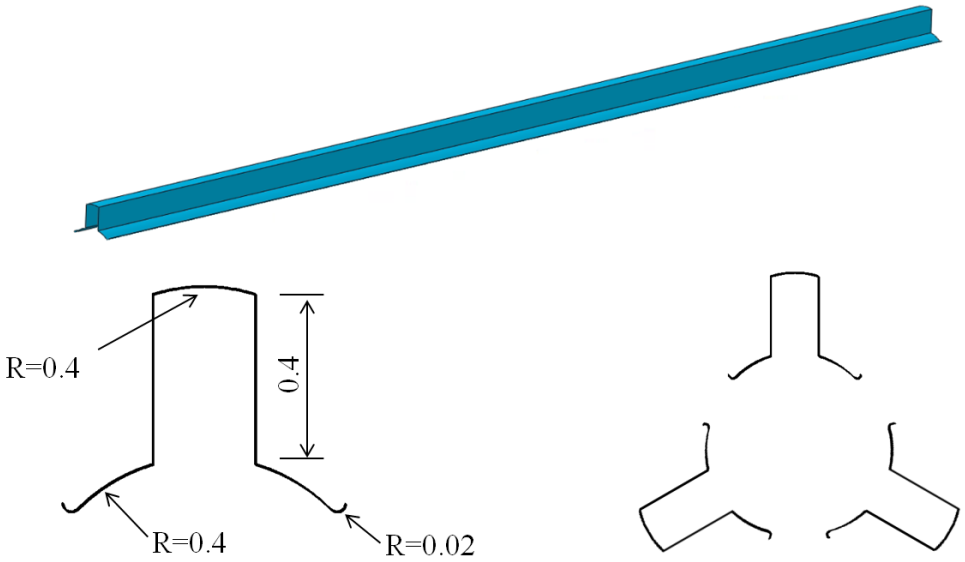

Figure 3.6 Rigid surface models for crimping the balloon model (Unit: mm).

The surface models were used as a crimping device to deform the balloon model. Displacement was applied to the surface models from radially outside the balloon model to the center to crimp the balloon model into a three-folded shape via contact condition between the surface models and balloon model (Fig 3.7) [57]. Next, a cylindrical surface model was created around the balloon model and to radially compress the balloon model by decreasing its diameter to 1.45 mm by applying displacement (Fig 3.8) [57].

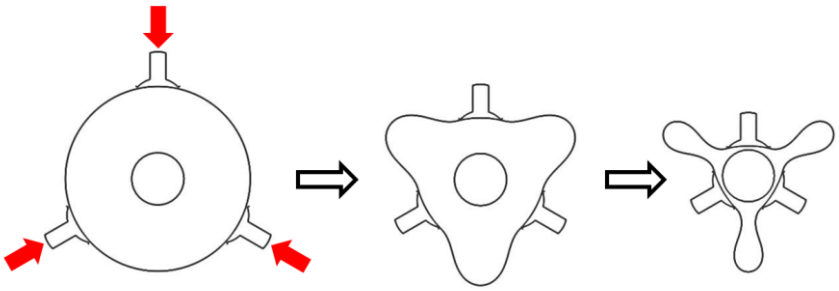

Figure 3.7 Crimping process for generating a three-folded shape. [57]

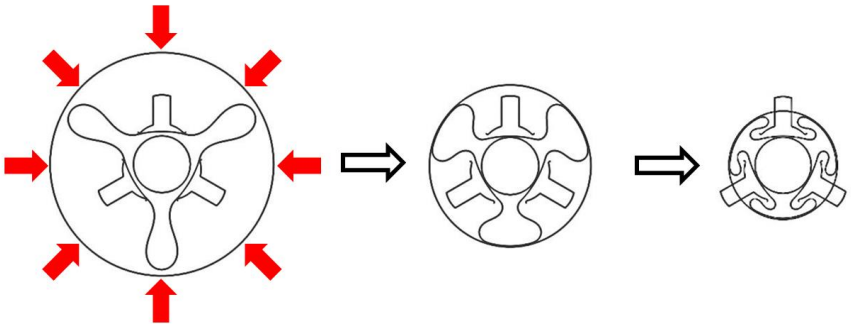

Figure 3.8 Compressing process for increasing the diameter of the balloon. [57]

Finally, three blades and cast pads were merged on the balloon model by tie-constraint to obtain the final three-folded cutting balloon model (Fig 3.9) [57]. For the non-compliant balloon model, a similar folding process was described in Chapter 2.2.1.5.

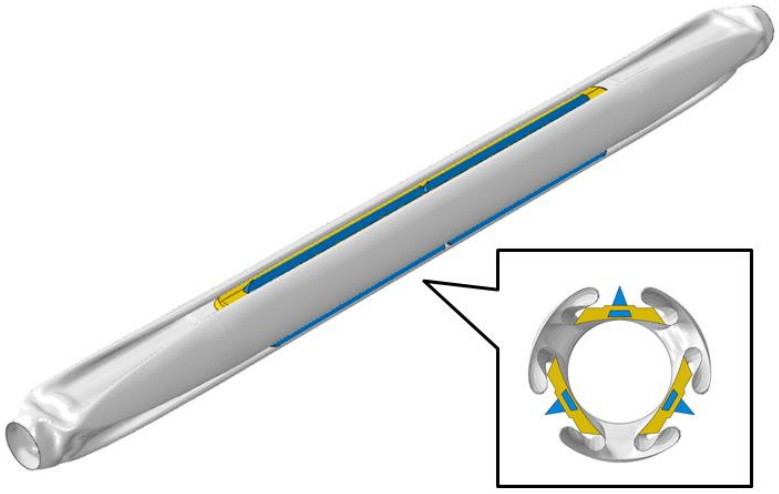

Figure 3.9 Final cutting balloon with blades and cast pads.

3.2.3 Simulation of expansions

The folded cutting balloon and non-compliant balloon models were set at the center of the calcified coronary model. Pressure was applied up to 1.216 MPa for the cutting balloon and 2.026 MPa for the non-compliant balloon to the inner surface of the balloon model. The shaft model, longitudinal ends of artery model, cutting balloon and non-compliant balloon models were fixed throughout entire simulation [57].

Expansion simulations were conducted and each analysis was performed as a quasi-static analysis (Fig 3.10). In the quasi-static simulation, the work applied by the external forces is nearly equal to the internal energy. It means that the inertial forces are negligible in a quasi-static analysis because the kinetic energy of the material in the model is negligibly small. As a general rule, the criterion is considered that the kinetic energy of the deforming material should not exceed a small fraction (typically 5% to 10%) of its internal energy throughout most of the process. The relationship of the kinetic energy and elastic internal energy for the 3.0-mm-diameter cutting balloon expansion are shown in Fig 3.11 [57].

The internal energy was lower than the kinetic energy at the beginning of the simulation (0.08 MPa~0.095 MPa). In Fig 3.12, the peak value for the ratio of kinetic energy to internal energy was 196.6% at 0.095 MPa. The ratio remained below 5% when the balloon inflation pressure became higher than 0.14 MPa. This data shows that the kinetic energy is a small fraction (less than 5%) of the internal energy through approximately 88% of the entire simulation. The beginning phase with the ratio over 5% in the analysis was considered acceptable.

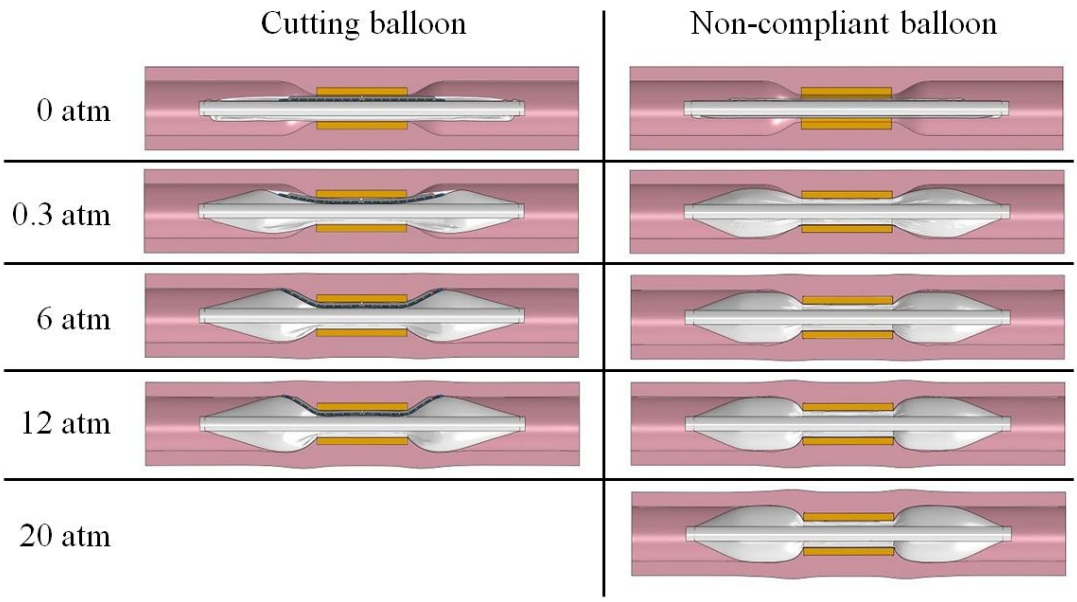

Figure 3.10 Expansion simulations in a calcified coronary artery model. [57]

Surface to surface contact conditions were specified with a friction coefficient of 0.2 between the following different models: blade-artery, blade-calcification, balloon-artery, balloon-calcification, cast pad-artery, cast pad-calcification, and balloon-balloon (self-contact between balloon folds).

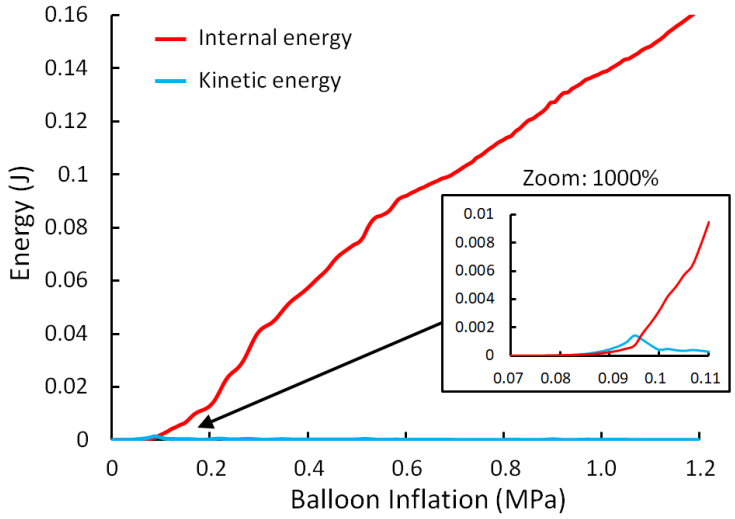

Figure 3.11 Kinetic energy and internal energy for the 3.0-mm-diameter cutting balloon expansion.

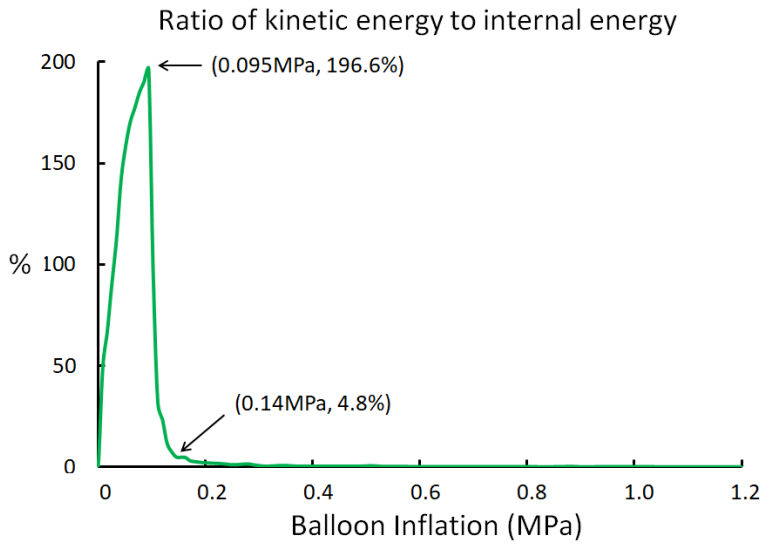

Figure 3.12 Ratio of kinetic energy to internal energy.

3.3 Result

3.3.1 Stresses in the calcification models

Fig 3.13 shows the contour plot of the maximum principal tensile stress in the calcification models for five different diameter cutting balloon expansions at the rate pressure. Fig 3.14 shows the contour plot of the calcification models for the 3.0 mm diameter non-compliant balloon at the nominal pressure and rated pressure. During balloon expansion, higher values of the stress generated at the end regions of the calcification models. In the cross-sectional views, peak values of stress were observed at the regions where the three blades were positioned. Furthermore, the larger diameter cutting balloons of 2.5, 2.75, and 3.0 mm resulted in higher stress in the middle region between the positions of the blades in the calcification models [57].

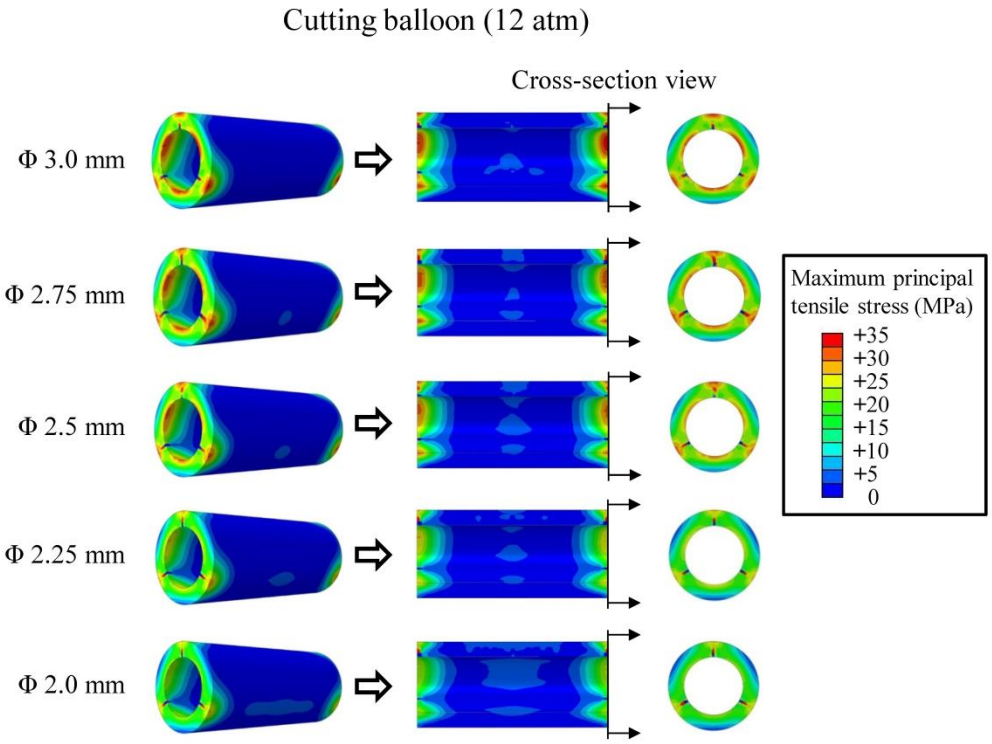

Figure 3.13 Stress distributions for the cutting balloons at the rated balloon inflation pressure of 12 atm. [57]

Fig 3.15 illustrates the peak values of the maximum principal tensile stress in the calcification models. Balloon inflation pressure for the cutting balloon was 0 to 1.216 MPa and for the non-compliant balloon was 0 to 2.026 MPa. The peak values of the maximum principal tensile stress in the calcification models under balloon inflation pressures of 0.608 MPa (6 atm), 1.216 MPa (12 atm), and 2.026 MPa (20 atm) are showed in Table 3.5 [57]. It was found that the larger diameter cutting balloons induced the higher stress concentration in the calcification model. Comparing the peak stress with the 3.0 mm diameter cutting balloon, the values at the nominal pressure were preserved to 99.4%, 99.2%, 98.8%, and 97.5% for the 2.75 mm, 2.5 mm, 2.25 mm and 2.0 mm diameter cutting balloons, respectively [57]. The values were preserved to 97.4%, 91.1%, 88.8%, and 84.2% at the rated pressure, respectively [57]. The effect of balloon

size was higher at the rated pressure on the stress concentrations [57].

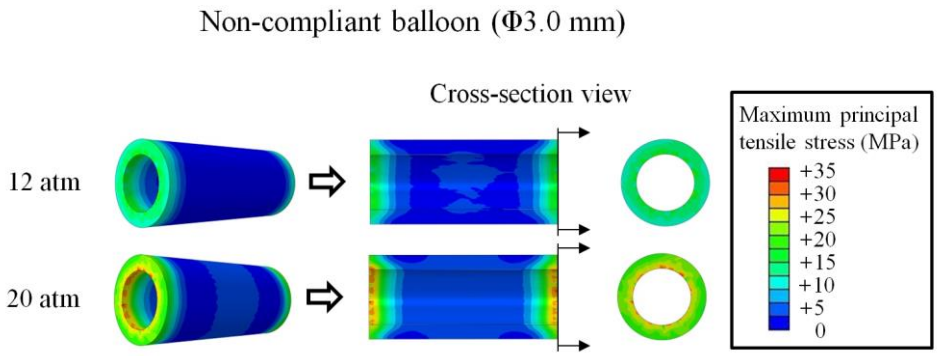

Figure 3.14 Stress distributions for the non-compliant balloon at the nominal pressure of 12 atm and the rated pressure of 20 atm. [57]

Additionally, the peak stress with the non-compliant balloon at the rated pressure 0f 20 atm was comparable to that with the 2.0 mm cutting balloon (downsized by 1 mm) at the nominal pressure of 6 atm. The blade plays a significant role on the stress concentrations in the calcification [57].

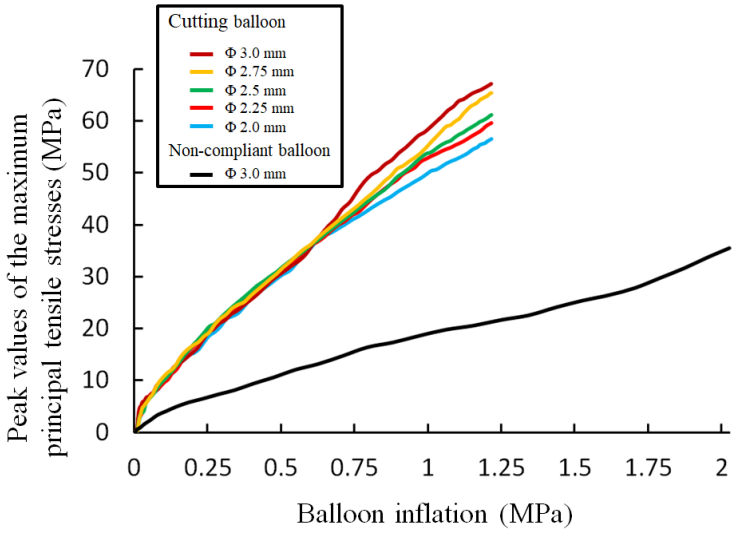

Figure 3.15 Maximum values of the maximum principal tensile stress in the calcification models. [57]

Table 3.5 Peak values of the maximum principal tensile stress in the calcification models for the nominal and rated balloon inflation pressures. [57]

	NC balloon	Cutting balloon				
Balloon diameter (mm)	3.0	2.0	2.25	2.50	2.75	3.0
Peak values of maximum principal tensile stress (MPa)						
6atm	13.21	35.52	35.98	36.12	36.19	36.42
12atm	21.68	56.53	59.61	61.17	65.39	67.14
20atm	35.51	N.A.	N.A.	N.A.	N.A.	N.A.

N.A.: not available

3.3.2 Stresses in the artery models

Fig 3.16 shows the maximum principal tensile stress yielded in the artery model and the cross-section views were taken from the location where the peak values occurred. Fig 3.17 shows the cross sectional views for each expansion at the rated pressure for the cutting balloon and the non-compliant balloon at nominal pressure and rated pressure [57].

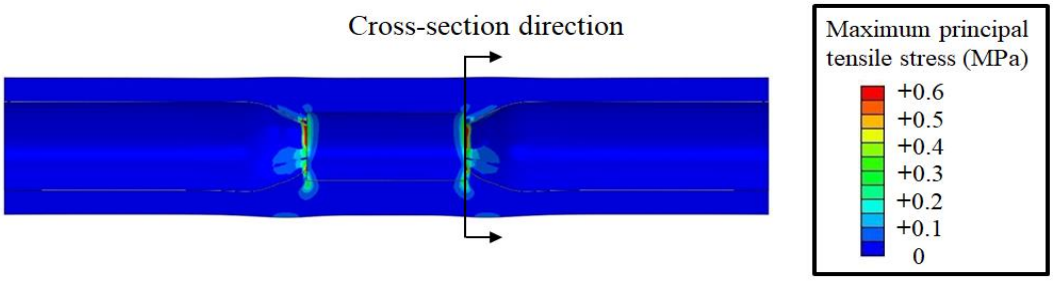

Figure 3.16 Side view of stress distribution in the artery models adjacent to the calcification model. [57]

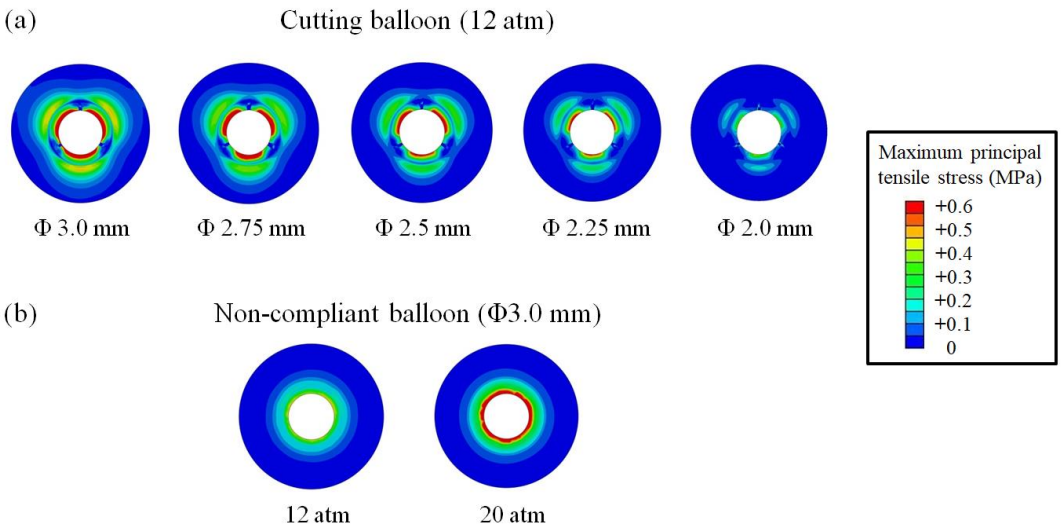

Figure 3.17 Cross-sectional views for (a) the cutting balloons at the rated pressure of 12 atm (b) non-compliant balloon at the nominal pressure of 12 atm and the rated pressure of 20 atm. [57]

High tensile stress was observed at the junction regions between the calcification and artery models. The cross-sectional views showed that higher stresses were induced between the regions where the blades contacted with the calcification for the cutting balloon expansions. Fig 3.18 illustrates the peak values of the maximum principal tensile stress generated in the artery models during balloon inflation. Table 3.6 lists the peak values of the maximum principal tensile stress in the artery models under pressures of 0.608 MPa (6 atm), 1.216 MPa (12 atm), and 2.026 MPa (20 atm) [57].

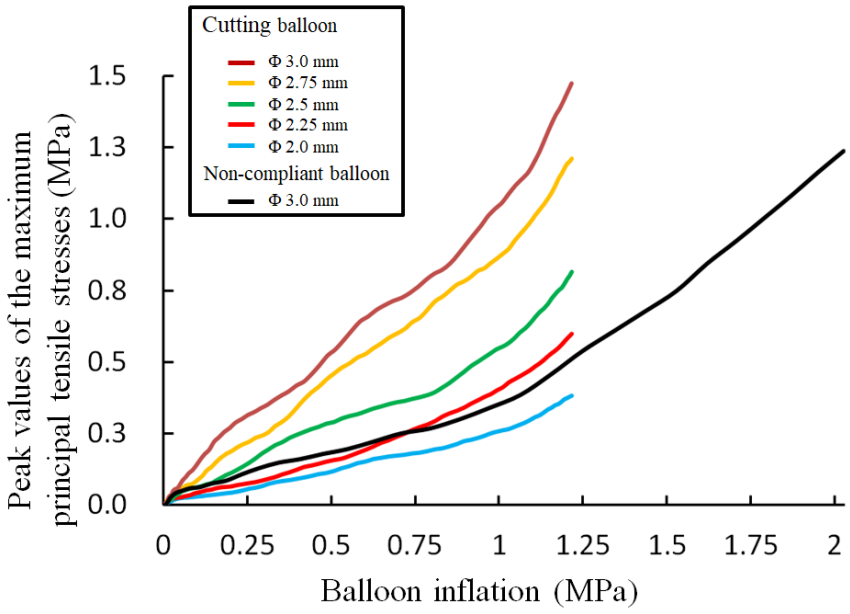

Figure 3.18 Peak values of the maximum principal tensile stress in the artery models. [57]

It shows that larger cutting balloon diameter induced higher stress level in the artery model. Comparing the stress with the 3.0 mm diameter cutting balloon, the values were reduced to 80.3%, 50%, 28.8%, and 22.7% for the 2.75 mm, 2.5 mm, 2.25 mm, and 2.0 mm diameter cutting balloons respectively at the nominal pressure [57]. At the rated pressure, those values were reduced to 82.3%, 55.8%, 40.1%, and 25.9%, respectively. It reveals that distinct decreases in the stress concentrations were observed when smaller diameter cutting balloons were used [57]. However, in the use of the non-compliant balloon, the peak values both at the nominal and rated pressures were even higher than those for the 2.0, 2.25, 2.5, and 2.75-mm-diameter cutting balloons [57].

Table 3.6 Peak values of the maximum principal tensile stress in the artery models for the nominal and rated balloon inflation pressures. [57]

	NC balloon	Cutting balloon				
Balloon diameter (mm)	3.0	2.0	2.25	2.50	2.75	3.0
Peak values of maximum principal tensile stress (MPa)						
6atm	0.22	0.15	0.19	0.33	0.53	0.66
12atm	0.54	0.38	0.59	0.82	1.21	1.47
20atm	1.24	N.A.	N.A.	N.A.	N.A.	N.A.

N.A.: not available

3.4 Discussion

3.4.1 Balloon-to-artery ratio

It reveals that cutting balloons with a balloon-to-artery ratio of less than 1:1 had a comparable ability to induce the stress concentration in the calcification while distinctly reducing the stress concentration at the border of the artery adjacent to the calcification [57]. The data indicates that the selection of a cutting balloon downsized by 0.5 mm or 0.25 mm might be effective for expanding calcification while reducing the risk of artery dissection and perforation [57].

Generally, for selecting balloons for lesion preparation, a balloon-to-artery ratio of 1:1 is recommended in clinical practice. However, the data suggest that the balloon-to-artery ratio of 1:1 is inappropriate for the cutting balloon. Downsized diameter in comparison with the reference diameter by 0.5 mm or 0.25 mm may be the first choice [57].

The stress yielded in the calcification for the non-compliant balloon at the rated pressure (20 atm) was smaller than that for the 2.5 mm diameter cutting balloon at the nominal balloon inflation pressure (6 atm). For the non-compliant balloon, the maximum stress yielded in the artery at the rated pressure (20 atm) was higher than that for the 2.75 mm diameter cutting balloon at the rated pressure (12 atm). Clinically, coronary artery perforation is the main disadvantage of cutting balloon angioplasty. These findings imply that the selection of a cutting balloon downsized by 0.5 or 0.25 mm might overcome the current limitation of the cutting balloon angioplasty [57].

3.4.2 Elastic modulus of the calcification

As described in Chapter 3.2.1, Young's modulus measured from the nanoindentation test for the calcification model is assumed to be 20.l GPa [43]. Nanoindentation was used to study mechanical properties of micro- and nano-hardness through calculating the applied force and depth of indentation, while a depth-sensing testing device indents a sample. The calcified plaques were collected from superficial femoral arteries retrieved within 1 hour following the amputation surgery and dried at room temperature for 24 hours. Nanoindentation was performed with those dry calcified plaque samples at room temperature.

Another nanoindentation study collected the calcified plaques from human carotid bifurcation plaque specimens. Those specimens were stored in physiological saline at 25°C before mechanical testing. Calcifications in calcified plaques were defined as stiff yellow-white or white parts isolated from surrounding tissue. Nanoidentation was performed and some modulus measurements for fresh and frozen calcifications were within the range of 100 MPa to 10 GPa. The upper range of modulus values of 10 ~ 20 GPa, were in the range of moduli for cortical

bone [61]. Elastic moduli for atherosclerotic calcifications measured using nanoindentation were reported within a range of 14.8 to 25.7 GPa [62].

Therefore, due to the large range in the elastic modulus for the calcification, the author considered another elastic modulus of 1 GPa for the calcification model to show the different stress levels in comparison with the current high value of 20.1 GPa.

Fig 3.19 shows the peak values of the maximum principal tensile stress in the two calcification models of 20.1 GPa and 1 GPa during balloon inflation. The values at nominal pressure and rated pressure are listed in Table 3.7. The ratios of stress for 1 GPa calcification to stress for 20.1 GPa calcification are calculated.

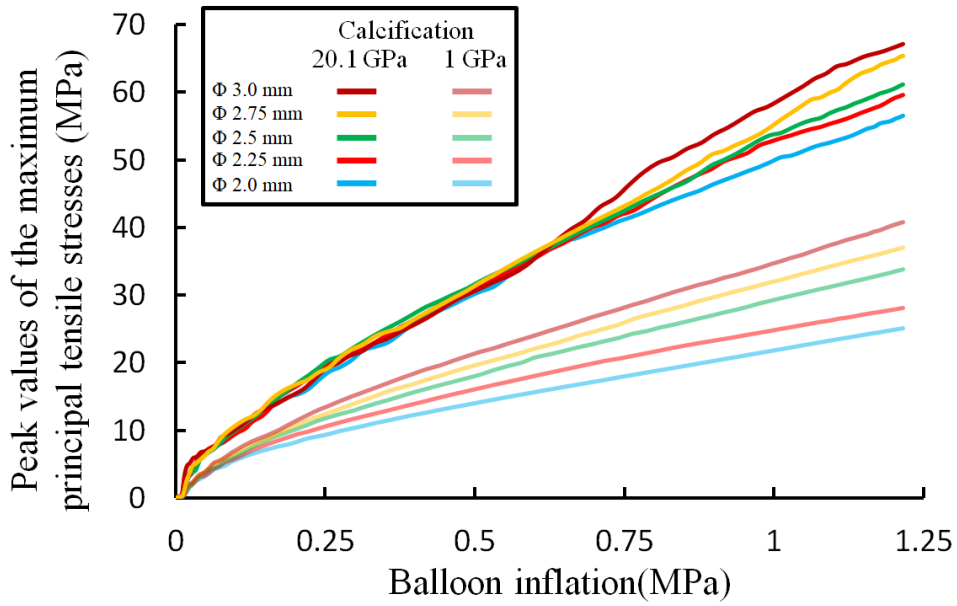

Figure 3.19 Peak values of the maximum principal tensile stress in the two calcification models. [57]

It is observed that the stresses are lower in the calcification of 1 GPa in comparison with the calcification of 20.1 GPa for the five different diameter cutting balloons. The ratios at nominal

pressure and rated pressure are in the range of 0.44 ~ 0.66.

Table 3.7 Peak values of maximum principal tensile stress at nominal pressure and rated pressure and ratios. [57]

Balloon diameter (mm)		2.0	2.25	2.50	2.75	3.0
Peak values of maximum principal tensile stress (MPa)						
6atm	20.1 GPa	35.52	35.98	36.12	36.19	36.42
	1 GPa	15.67	18.07	20.80	22.12	24.06
Ratio		0.44	0.50	0.58	0.61	0.66
12atm	20.1 GPa	56.53	59.61	61.17	65.39	67.14
	1 GPa	25.09	28.10	33.82	37.05	40.78
Ratio		0.44	0.47	0.55	0.57	0.61

3.5 Conclusion

In this chapter, the author carried out the contents as follows.

(1) generating the cutting balloon model with blades on the balloon surface.

(2) simulating the expansion of the cutting balloon with different diameter (2.0 mm, 2.25 mm, 2.50 mm, 2.75 mm and 3.0 mm) in a calcified coronary artery model with a 360 degrees calcification model.

These findings suggest that a balloon-to-artery ratio of 1:1 for the use of the cutting balloon is inappropriate. The ability to fracture the calcification for the cutting balloon seems to be superior to the non-compliant balloon. It indicates that the selection of a cutting balloon

downsized by 0.5 mm or 0.25 mm in comparison with the reference diameter of 3.0 mm may be the first choice in terms of effectively fracturing the calcification while reducing the risks of artery dissection and perforation [57].

Chapter 4: Effects of balloon-to-artery ratio and number of blades facing 180° calcification

4.1 Chapter introduction

In this chapter, the author focuses on a 180° calcification in the artery model and investigates the influence of the lesion/device diameter ratio and the number of blades facing the calcification model [63].

The aims in this chapter are listed as:

(1) to carry out the expansions of cutting balloons with different diameters in a calcified artery model with a 180° calcification model.

(2) to compare the two conditions where either one or two blades face the 180° calcification model.

It is crucial to figure out the different direction of the blades in a dissymmetric lesion for the cutting balloon expansion utilization in clinical treatment since the randomized clinical trial has shown that coronary artery injury such as perforation and dissection after cutting balloon angioplasty.

The author aims to gain mechanistic insights into lesion/device diameter ratio and the number of blades facing a non-circular calcified lesion to understand the importance of fracturing the calcification while avoiding vessel injury [63].

4.2 Modeling of cutting-balloon expansion

A clinical study reported that fracture of calcification in conventional balloon angioplasty was observed in about 2.0% (4 of 198) of the lesions where the maximum calcium angles were ≤ 180° in the circumferential-wise direction by means of investigating the cross-sectional images of optical coherence tomography [46][63]. This data emphasizes the importance of gaining more knowledge on calcifications whose maximum calcium angles are ≤ 180° to improve clinical outcomes. Therefore, in this Chapter, a calcification model with an angle of 180°, length 5 mm, and thickness 0.4 mm was constructed and constrained by tie constraint at the middle of the artery model (Fig 4.1) [63]. The artery model and calcification model were meshed using approximate 402,000 and 20,400 eight-node hexahedral elements (C3D8R), respectively [63].

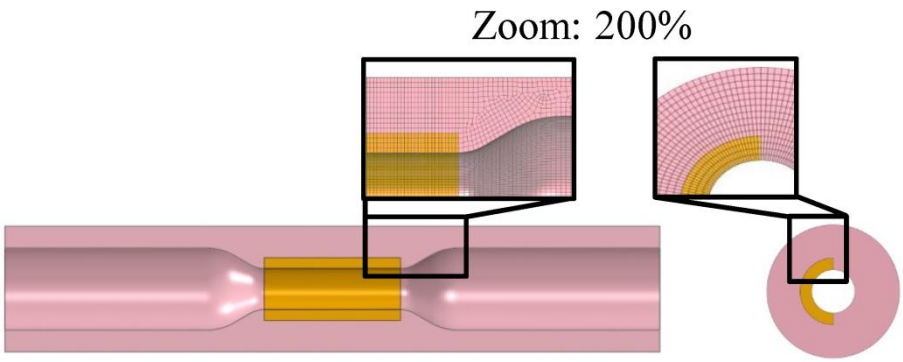

Figure 4.1 Geometric and mesh models for coronary artery and calcification. [63]

Expansion simulations of five different diameter (2.0, 2.25, 2.5, 2.75 and 3.0 mm) cutting balloons were carried out in the calcified artery models (Fig 4.2). Pressure, up to the rated pressure of 1.216 MPa (12 atm), was applied to the inner surface of the balloon model. The shaft model, longitudinal ends of the balloon model and artery model were fixed through the

entire simulation. In terms of the directions of the three blades facing the 180° calcification model, two types were considered in the expansion simulations (Fig 4.3): Type 1 had one blade facing the calcification model while the other two blades faced the artery wall; Type 2 had two blades facing the calcification while the other one blade faced the artery wall [63].

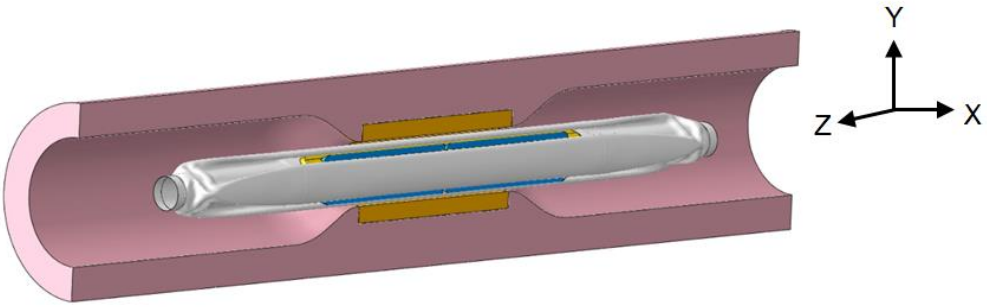

Figure 4.2 Expansion simulation for the cutting balloon in a 180° calcified artery model. [63]

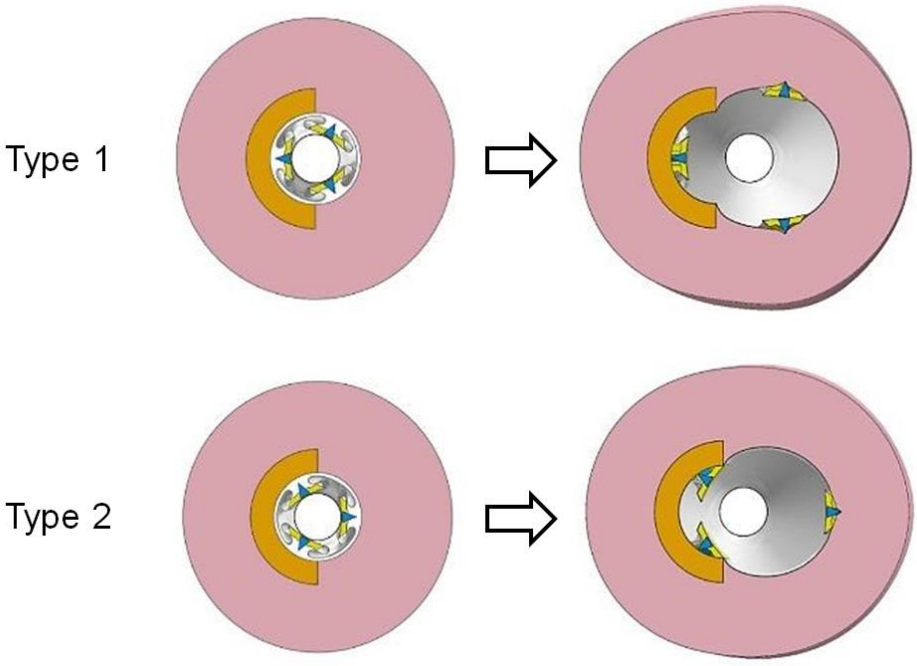

Figure 4.3 Two types for the cutting balloon in the 180° calcified artery model. [63]

4.3 Result

4.3.1 Stresses in the calcification models

Fig 4.4 shows the contour plot of the maximum principal tensile stress in the calcification models. Fig 4.5 and Fig 4.6 illustrate the peak values extracted along the lengths of the calcification models for Type 1 and Type 2 at the rated pressure of 12 atm [63].

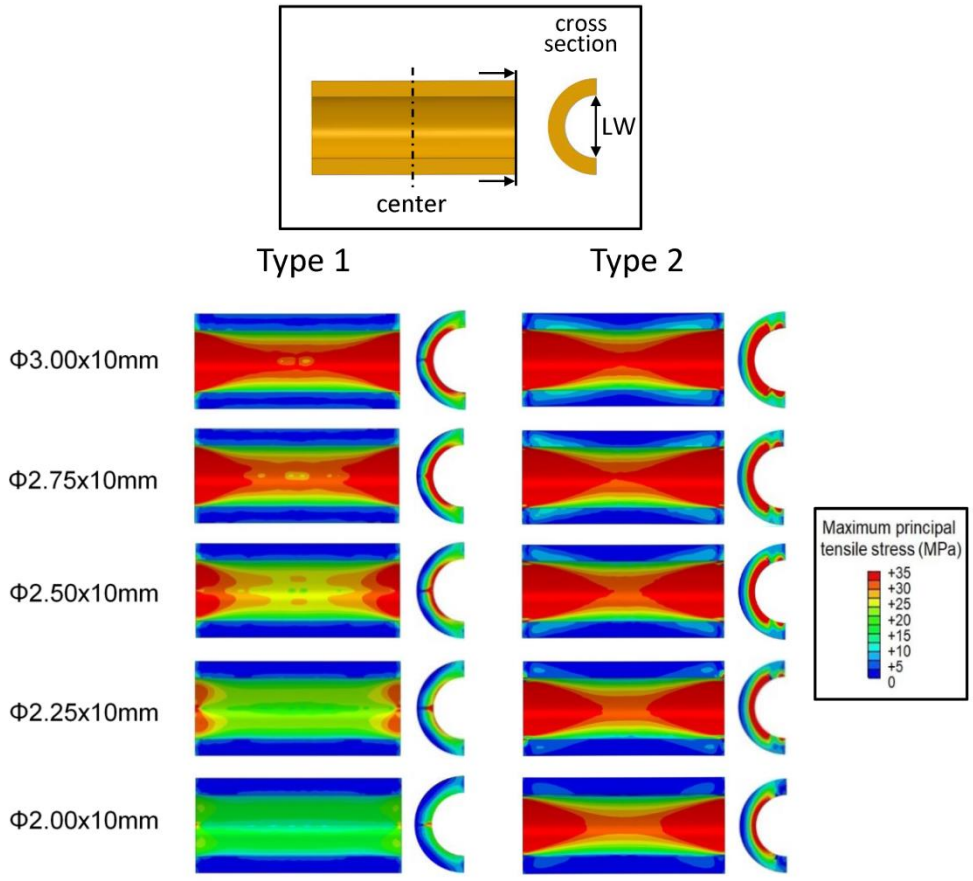

Figure 4.4 Stress distributions in the calcified artery models for Type 1 and Type 2 at rated pressure (12 atm) with five different balloon diameters. [63]

The stresses were higher at both longitudinal ends than at the center, in each calcification model. The stresses at the longitudinal ends of the calcifications were higher by 61, 79, 100, 105, and 123% than those at the centers of the calcification models for each cutting balloon in Type 1 [63]. Similarly, the stresses at the longitudinal ends of the calcifications were higher by 72, 114, 138, 174, and 193% than those at the centers for each cutting balloon in Type 2 [63]. This data indicated that cracks might occur at the longitudinal ends in the calcification during cutting balloon expansion [63]. The peak values of the maximum principal tensile stresses in the calcification models for Types 1 and Type 2 during balloon expansion are extracted in Fig 4.7 [63]. All the peak values for Type 1 and Type 2 at both nominal pressure and rated pressure are listed in Table 4.1 [63].

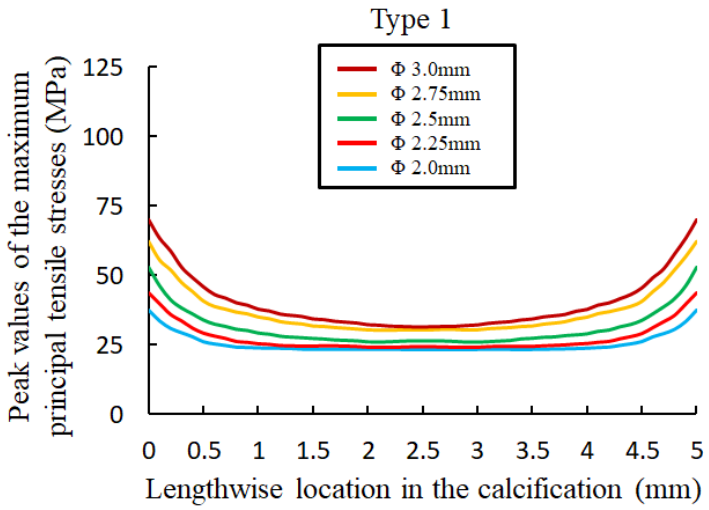

Figure 4.5 Peak values of the maximum principal tensile stresses in the calcification models along the longitudinal direction for Type 1 at the rated pressure (12 atm). [63]

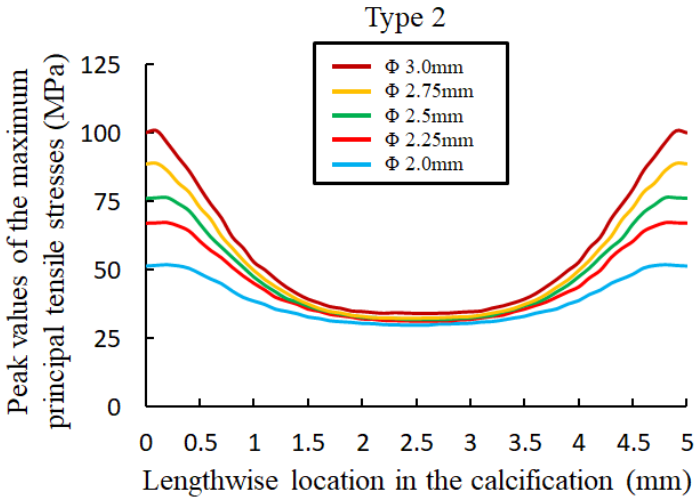

Figure 4.6 Peak values of the maximum principal tensile stresses in the calcification models along the longitudinal direction for Type 2 at the rated pressure (12 atm). [63]

It is observed that larger balloon diameters induced the higher levels of stress for both Type 1 and Type 2, except for the cutting balloon diameter of 2 mm at the nominal pressure (6 atm) in Type 2 [63]. Particularly, the peak values for 2 and 2.25 mm diameters in Type 2 were observed to creep down rapidly, near the pressures of 0.5 and 0.9 MPa, respectively [63].

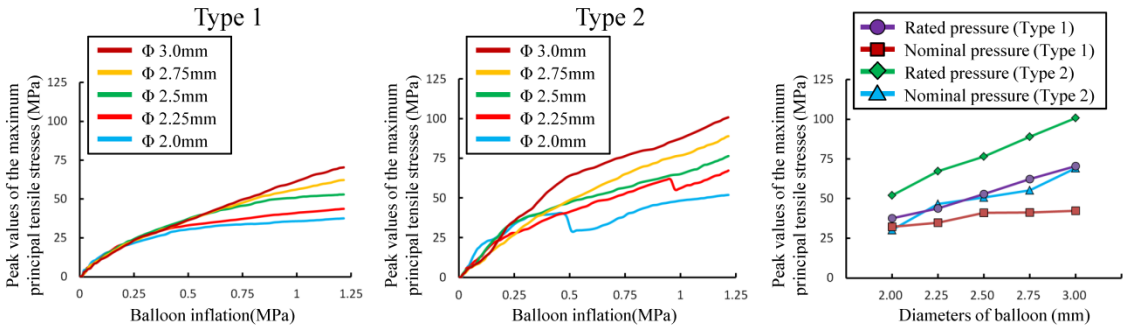

Figure 4.7 Effects of cutting balloon diameter and blade direction on the maximum principal tensile stresses in the models of the calcification. [63]

The results indicated that the calcification expansion ability of the cutting balloon in the case of Type 2 under the nominal pressure of 6 atm was comparable to that in the case of Type 1

under the rated pressure of 12 atm [63]. Moreover, under both the nominal and rated pressures, larger stress concentrations occurred in the calcification models even using undersized balloons of diameter 2.5 and 2.75 mm in Type 2, in comparison with a balloon of diameter 3.0 mm in Type 1 (Table 4.1) [63].

Additionally, the lumen width corresponding to the inner diameter of calcification before expansion at the longitudinal and circumferential ends (denoted as "LW" in Fig 4.4) are measured and listed in Table 4.2 [63]. The lumen width in Type 2 increased in comparison with that in Type 1 for each cutting balloon diameter at both the nominal pressure and rated pressure [63].

Table 4.1 Peak values of the maximum principal tensile stresses in the calcification models. [63]

Balloon diameter (mm)		2.0	2.25	2.5	2.75	3.0
Peak values of the maximum principal tensile stresses (MPa)						
Nominal pressure (6 atm)	Type 1	32.2	34.8	41.1	41.3	42.4
	Type 2	30.2	46.7	50.7	55.1	69.1
Rated pressure (12 atm)	Type 1	37.5	43.7	52.9	62.2	70.4
	Type 2	51.9	67.3	76.4	88.9	100.8

Table 4.2 Lumen width at the inner surface of the calcification model at the longitudinal and circumferential ends. [63]

Balloon diameter (mm)		2.0	2.25	2.5	2.75	3.0
Lumen width (mm)						
Nominal pressure (6 atm)	Type 1	1.504	1.506	1.507	1.509	1.513
	Type 2	1.509	1.511	1.515	1.517	1.519
Rated pressure (12 atm)	Type 1	1.508	1.513	1.517	1.520	1.524
	Type 2	1.518	1.528	1.536	1.543	1.552

4.3.2 Stresses in the artery models

Fig 4.8 shows the maximum principal tensile stresses generated in the coronary artery model adjacent to the calcification for Type 1 and Type 2 at the rated pressure of 12 atm. All the cross-sections were drawn at the end positions of the artery models connected with the calcification models where the peak values occurred [63].

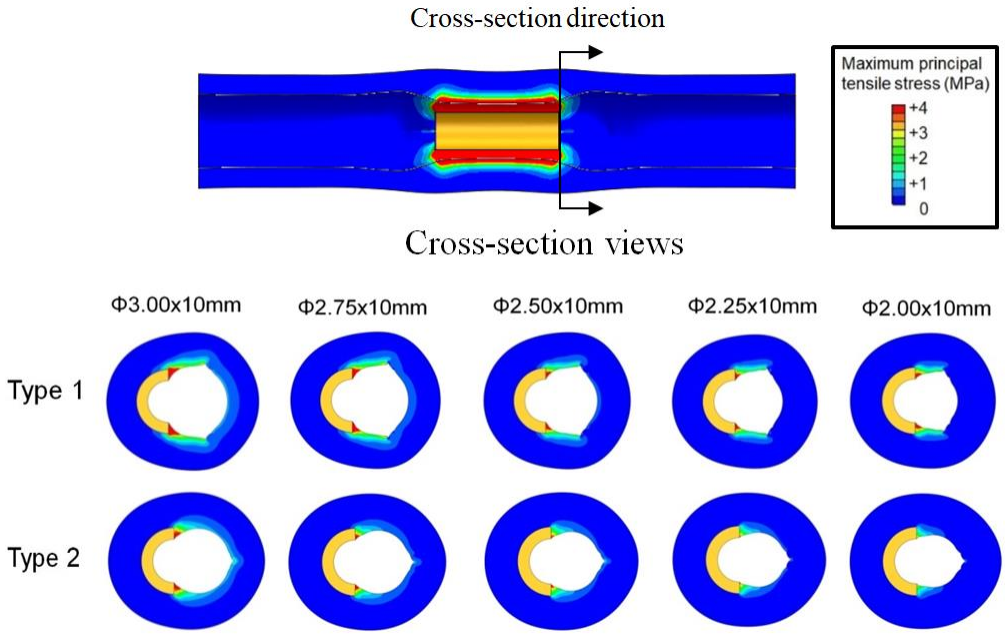

Figure 4.8 Stress distributions in the artery model for Type 1 and Type 2 at the rated pressure (12 atm) for the five different balloon diameters. [63]

Fig 4.9 shows the peak values of the maximum principal tensile stresses generated in the artery models adjacent to the calcification during the balloon expansion. The peak values at the nominal pressure and rated pressure for Type 1 and Type 2 are showed in Table 4.3. The larger balloon diameters induced the higher levels of stress for both the types in the artery models adjacent to the calcification [63]. For each cutting balloon diameter, the peak values at both

nominal and rated pressures for Type 1 were higher than that for Type 2 [63]. Interestingly, in the case of Type 2, the maximum principal stress produced in the artery model adjacent to the calcification, under the rated pressure of 12 atm when employing under-sized balloons, was smaller than that in the case of Type 1 using lesion-identical balloon diameters under the nominal pressure of 6 atm (Table 4.3, Fig 4.9) [63].

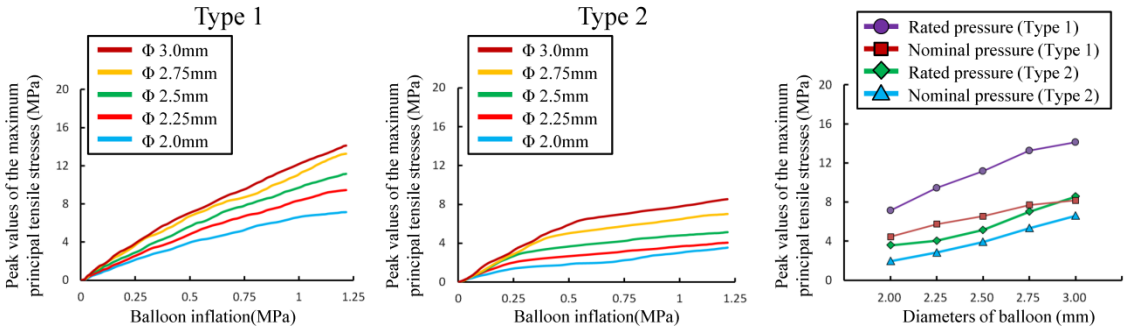

Figure 4.9 Effects of cutting balloon diameter and blade direction on the maximum principal tensile stresses in the models of artery adjacent to the calcification. [63]

Table 4.3 Peak values of the maximum principal tensile stresses in the model of artery adjacent to the calcification. [63]

Balloon diameter (mm)		2.0	2.25	2.5	2.75	3.0
Peak values of the maximum principal tensile stresses (MPa)						
Nominal pressure (6 atm)	Type 1	4.45	5.73	6.57	7.69	8.19
	Type 2	1.96	2.85	3.92	5.34	6.59
Rated pressure (12 atm)	Type 1	7.15	9.46	11.16	13.27	14.12
	Type 2	3.55	4.06	5.15	7.02	8.54

These findings suggest that in the case of Type 2, the risk of dissection or perforation upon expanding the balloon with the rated pressure can be reduced, in comparison with the balloon

expansion under nominal pressure in Type 1, when at least 0.25 mm undersized balloons are employed [63].

4.3.3 Effects of balloon diameter and blade direction

In Fig 4.7, a reduction in stress is observed during the expansion of the 2.0 mm and 2.25 mm diameter cutting balloons of Type 2, at the pressures of 0.5 and 0.95 MPa, respectively [63]. This resulted in lower peak stresses in Type 2, compared to that in Type 1 at the nominal pressure of 6atm [63]. An obvious slippage of the blades was observed and two of the blades were dragged in opposite directions during the expansion (the red arrows in Fig 4.10) [63].

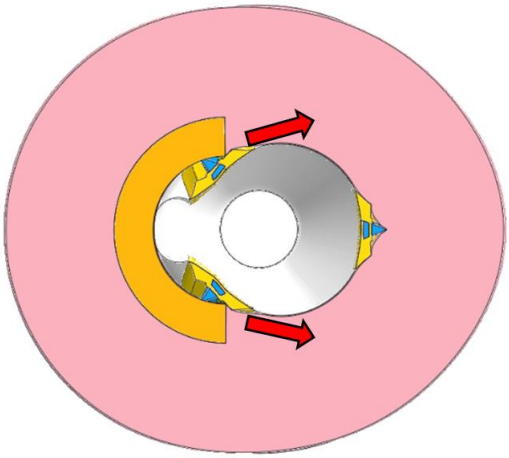

Figure 4.10 Incidence of slippage during the inflation of balloons of diameters 2 and 2.25 mm. [63]

Moreover, the stresses in Type 2 expansion for the 2.0 mm cutting balloon expansion were higher than those for the other balloon diameters, from the incipient pressure of 0.06 MPa to 0.15 MPa [63]. The angular change of the blade facing the calcification model was measured

from the center line of the blade cross-section during expansion (Fig 4.11) [63]. In Fig 4.12, the angular change for the 2.0 mm cutting balloon was obviously lower than that for the 2.25, 2.5, 2.75, and 3.0 mm cutting balloons for the entire pressure range including 0.06 to 0.15 MPa. Therefore, a higher acting force was generated in the normal direction [63].

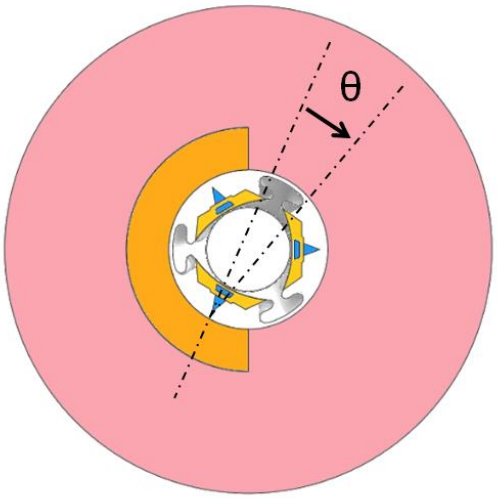

Figure 4.11 Change in the angle of the blade facing the calcification model during expansion. [63]

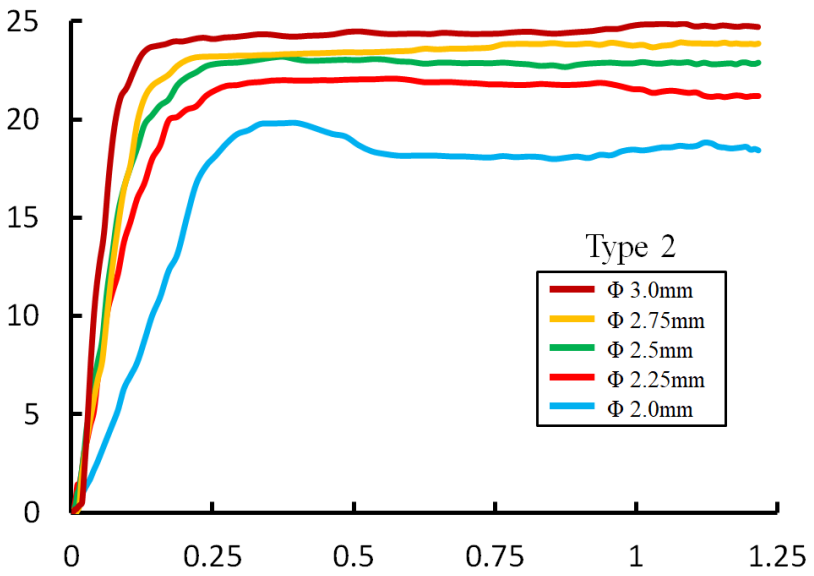

Figure 4.12 Comparison of angle changes of cutting balloons for the entire pressure range. [63]

4.4 Discussion

4.4.1 Balloon-to-artery ratio and number of blades facing the 180° calcification

The author considered two cases in the 180° calcified artery model to perform the expansion simulations of the cutting balloons with five different balloon diameters. Type 1 is the case that one blade faced the calcification while the other two blades faced the artery wall. Type 2 is the case that two blades faced the calcification while the other faced the artery wall [63]. The lesion expansion ability was distinctly higher when two blades faced the calcification model than when one blade faced the calcification model [63]. Moreover, when two blades faced the calcification, larger stresses were generated in the calcification even when using undersized balloons with diameters reduced by 0.5 or 0.25 mm from the reference diameter, in comparison with the case where one blade faced the calcification and a balloon of diameter equal to the reference diameter was used [63]. In terms of the stress concentration in the model of the artery adjacent to the calcification, the peak values were higher when one blade faced the calcification (Type 1) than when two blades faced the calcification (Type 2) [63]. Interestingly, in the case where two blades faced the calcification (Type 2), the maximum principal stress generated in the artery model adjacent to the calcification under the rated pressure of 12 atm when the under-sized balloons were employed was smaller than that in the case where one blade faced the calcification (Type 1) and lesion-identical balloon diameters were used under the nominal pressure of 6 atm [63]. These findings suggest that in the case where two blades face the

calcification, 0.5 or 0.25 mm size-down balloons would be effective for not only expanding the calcified lesion but also reducing the risk of dissection and perforation [63].

Cutting balloon angioplasty provided adequate lumen expansion in the calcified lesions, but suffered from the possibility of dissection [25] [63]. In this study, a larger balloon diameter resulted in a higher level of stress in both the models of the calcification and artery adjacent to the calcification, which might lead to plaque rupture and arterial dissection [63]. A comparison of the two types of expansions in 180° calcified artery models indicated that the arrangement where two blades faced the calcification as opposed to one blade might generate higher stresses in the calcification models for inducing fracture, while generating lower stresses in the artery models adjacent to the calcification, so as to be less traumatic to the arterial wall [63].

In a clinical setting, there are no measures to guide two blades facing the calcification. However, it showed that three-time repetition of delivery-balloon inflation for stent deployment increased the luminal cross-sectional area [63] [64] [65]. Repeating the cutting balloon inflation by changing the rotation of the cutting balloon catheter may change the direction of the blades and may be able to adjust two blades toward the calcification side [63].

4.4.2 Effect of contact friction coefficient

In Chapter 4.3.3, slippage was observed in the expansion of 2.0 mm and 2.25 mm cutting balloon in the case of two blades facing the 180° calcification. The contact friction coefficient is considered as the factor in the contact condition. Therefore, in Type 2, different friction coefficients of 0.1, 0.2 and 0.3 were considered and compared for the 2.0 mm and 2.25 mm diameter cutting balloon in the 180° calcified artery model. The peak values of the maximum principal tensile stresses in the calcifications for 2.0 mm diameter cutting balloon were shown in

Fig 4.13. The phenomenon of creep down for the peak values were observed for different friction coefficients of 0.1, 0.2 and 0.3, near the pressure of 0.45 MPa, 0.5 MPa and 0.85 MPa, respectively. The peak values of the maximum principal tensile stresses in the calcifications for 2.25 mm diameter cutting balloon were shown in Fig 4.14. The phenomenon of creep down for the peak values were observed for the friction coefficients of 0.1, 0.2 near the pressure of 0.55 MPa and 0.95 MPa. However, there is no creep down observed in the case of friction coefficient of 0.3. It is revealed that larger friction coefficient might prevent slippage of the 2.0 mm and 2.25 mm diameter cutting balloon during expansion in the 180° calcified artery model. The friction coefficient plays a role in the expansion of cutting balloon.

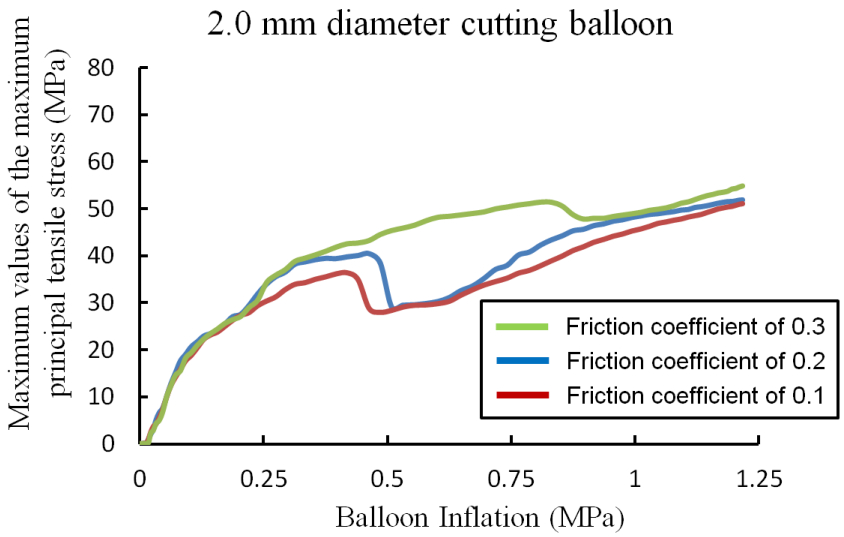

Figure 4.13 Peak values of maximum principal tensile stress in the calcifications for the 2.0 mm diameter cutting balloon by setting different friction coefficients in Type 2.

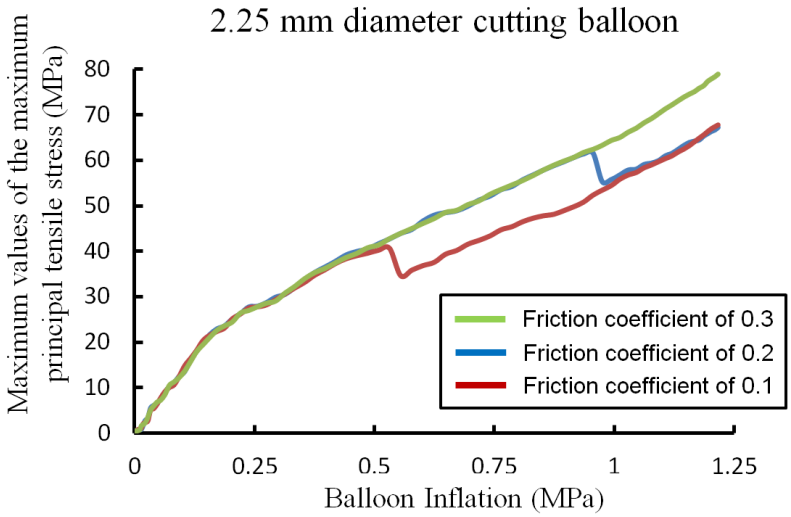

Figure 4.14 Peak values of maximum principal tensile stress in the calcifications for the 2.25 mm diameter cutting balloon by setting different friction coefficients in Type 2.

4.4.3 Effect of the elastic modulus of the calcification

As discussed in Chapter 3.4.2, a variation of elastic modulus of the calcification was observed in some nanoindentation studies. A nanoindentation study reported that Young's modulus for human calcified plaques collected from the superficial femoral artery wall was 20.1 GPa [43]. A range of 100 MPa to 10 GPa, some as high as 21 GPa was measured from human carotid bifurcation plaque specimens [61]. Another study reported the elastic moduli for atherosclerotic calcifications were in a range of 14.8 to 25.7 GPa [62]. In this section, the author considers two elastic moduli of 20.1 GPa and 1 GPa of the calcification in the expansion of five different diameter cutting balloon in the two types.

Fig 4.15 shows the peak values of maximum principal tensile stress in the calcifications of 20.1 GPa and 1 GPa for the five different cutting balloon during inflation in Type 1. Table 4.4 lists the peak values at nominal pressure and rated pressure and the ratios of stress in 1GPa

calcification to 20.1 GPa calcification are calculated. The ratios are in the range of 0.35 ~ 0.67 at the nominal pressure and 0.43 ~ 0.62 at the rated pressure for the five different diameter cutting balloon.

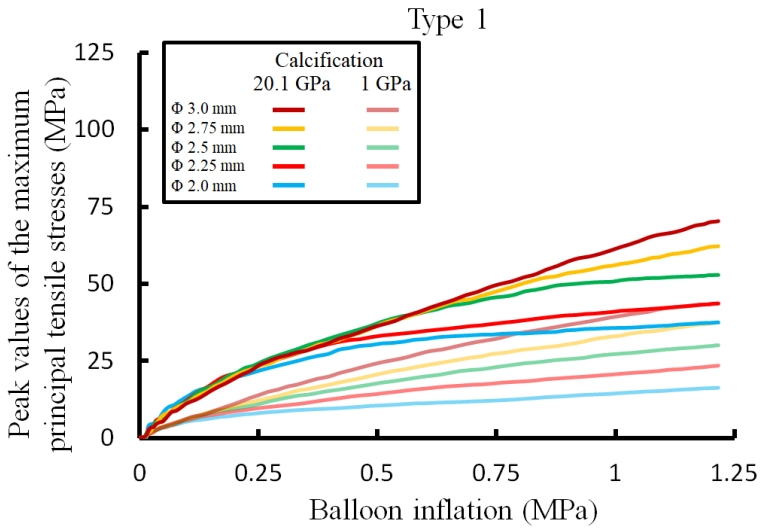

Figure 4.15 Peak values of the maximum principal tensile stress in the two calcification models during cutting balloon inflation in Type 1. [63]

Table 4.4 Peak values of the maximum principal tensile stress at nominal pressure and rated pressure and ratios in Type 1. [63]

Balloon diameter (mm)		2.0	2.25	2.50	2.75	3.0
Peak values of maximum principal tensile stress (MPa)						
6atm	20.1 GPa	32.2	34.8	41.1	41.3	42.4
	1 GPa	11.3	16.1	20.1	23.6	28.2
Ratio		0.35	0.46	0.49	0.57	0.67
12atm	20.1 GPa	37.5	43.7	52.9	62.2	70.4
	1 GPa	16.3	23.5	30.1	37.5	43.7
Ratio		0.43	0.54	0.57	0.60	0.62

Fig 4.16 shows the peak values of maximum principal tensile stress in the calcifications of 20.1 GPa and 1 GPa for the five different cutting balloon during inflation in Type 2. Table 4.5 lists the peak values at nominal pressure and rated pressure and the ratios of stress in 1GPa calcification to 20.1 GPa calcification are calculated. The ratios are in the range of 0.60 ~ 0.82 at the nominal pressure and 0.63 ~ 0.71 at the rated pressure for the five different diameter cutting balloon.

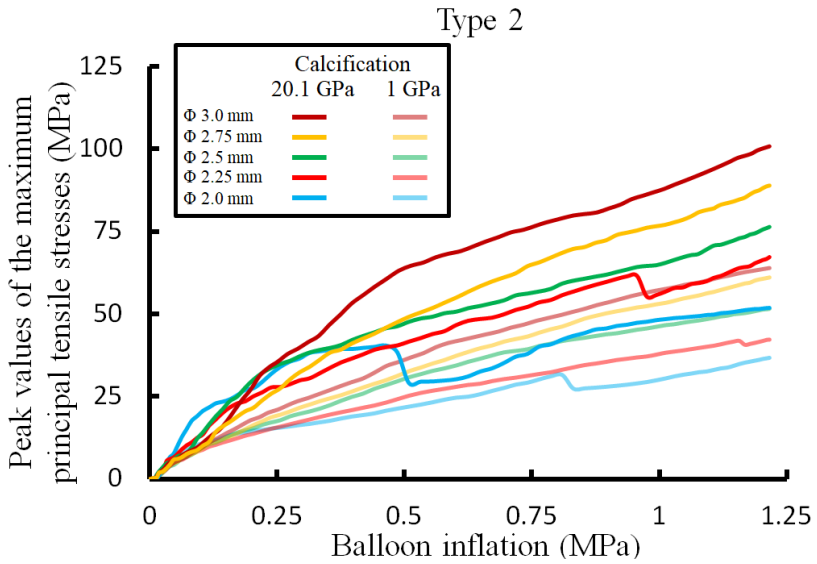

Figure 4.16 Peak values of the maximum principal tensile stress in the two calcification models during cutting balloon inflation in Type 2. [63]

Additionally, the lumen width corresponding to the inner diameter of calcification before expansion at the longitudinal and circumferential ends (denoted as “LW” in Fig 4.4) are measured and listed in Table 4.6 [63]. The lumen width in Type 2 increased in comparison with that in Type 1 for each cutting balloon diameter at both the nominal pressure and rated pressure [63]. It shows that the lumen width for the calcification of 1 GPa are larger than those for the calcification of 20.1 GPa.

Table 4.5 Peak values of the maximum principal tensile stress at nominal pressure and rated pressure and ratios in Type 2. [63]

Balloon diameter (mm)		2.0	2.25	2.50	2.75	3.0
Peak values of maximum principal tensile stress (MPa)						
6atm	20.1 GPa	30.2	46.7	50.7	55.1	69.1
	1 GPa	24.7	27.9	34.4	37.4	42.1
Ratio		0.82	0.60	0.68	0.68	0.61
12atm	20.1 GPa	51.9	67.3	76.4	88.9	100.8
	1 GPa	36.8	42.3	51.6	61.1	63.9
Ratio		0.71	0.63	0.68	0.69	0.63

Table 4.6 Lumen width at the inner surface of the calcification model at the longitudinal and circumferential ends for the calcifications of 20.1 GPa and 1 GPa. [63]

Balloon diameter (mm)			2.0	2.25	2.5	2.75	3.0
Lumen width (mm)							
20.1 GPa	Nominal pressure (6 atm)	Type 1	1.504	1.506	1.507	1.509	1.513
		Type 2	1.509	1.511	1.515	1.517	1.519
	Rated pressure (12 atm)	Type 1	1.508	1.513	1.517	1.520	1.524
		Type 2	1.518	1.528	1.536	1.543	1.552
1 GPa	Nominal pressure (6 atm)	Type 1	1.564	1.585	1.617	1.642	1.668
		Type 2	1.629	1.656	1.679	1.709	1.732
	Rated pressure (12 atm)	Type 1	1.617	1.637	1.682	1.717	1.746
		Type 2	1.760	1.789	1.824	1.865	1.908

4.5 Conclusion

This chapter described the following contents:

(1) carrying out the expansions of the cutting balloons with different diameters (2.0 mm, 2.25 mm, 2.50 mm, 2.75 mm and 3.0 mm) in a calcified artery model with a 180° calcification model.

(2) comparing the two conditions where either one or two blades face the 180° calcification model.

These findings suggest that when non-circular calcified lesion is treated using the cutting balloon, 0.25 mm or 0.5 mm undersized balloons in comparison with the reference diameter would be effective in not only expanding the calcified lesion but also reducing the risk of dissection and vessel perforation. In clinical setting, although there are no methods to guide two blades facing the calcium, the suggestion is that repeating the cutting balloon inflation though changing rotation of the cutting balloon catheter may adjust the direction of the blades to the calcium [63].

Chapter 3 and Chapter 4 presented the simulations of the cutting balloon expanding in a 360° and 180° calcification models. In the case of 180° calcification model, two types were confirmed and the findings indicated the number of blades facing the 180° calcification model plays a role in the expansion of the cutting balloon. 0.25 mm or 0.5 mm undersized cutting balloon may be more appropriate to be used in the reference 3.0 mm diameter calcified artery in the both cases with potentially fracturing the calcification and avoiding arterial injury. Although there are many variations in the calcification such as angle and dimension, these findings may present a suggestion on the selection of balloon-to-artery ratio and the influence on the direction of blades in cutting balloon angioplasty.

Chapter 5: Conclusion and future work

5.1 Chapter introduction

This chapter describes the conclusion and future work of this thesis. The author summarizes the overall contents with the main points in this study. Moreover, the author lists the issues considered as extensions of this study and suggests the future direction of this study.

5.2 Conclusion

In this thesis, the author investigated the efficacy and safety of expanding the cutting balloon in calcified artery models using the finite element method. The author generated a useful numerical method of modeling a three-folded balloon shape according to the process of a wrapped balloon. A complex device of cutting balloon model was successfully created through this method. The thesis was composed of five chapters.

In Chapter 1, the background of the general treatment for coronary artery calcification and the cutting balloon was introduced. The author described the state-of-arts of related studies to understand the finite element balloon model definition, plaque model material and a reference research to indicate the purpose of this study.

In Chapter 2, the dimensions of the balloon model, as well as the isotropic elastic material properties, were determined referring to the compliance chart and the accuracy of the balloon expansion was ensured. The wrapped balloon model was generated by means of the process of crimping and compressing. Furthermore, stent expansion through the wrapped balloon model

was conducted to confirm the realistic expansion of the stent model and balloon expansion in a stenotic artery model was performed to verify the reliability of the wrapped balloon model in comparison with a cylinder expansion.

In Chapter 3, the author created the balloon model through the compliance chart by means of the method described in Chapter 2 and generated the cutting balloon model. The simulations of expansion for the cutting balloon in the calcified artery model with different balloon diameters are carried out in comparison with a non-compliant balloon. It indicated that the selection of a cutting balloon downsized by 0.25 or 0.5 mm in comparison with the reference diameter is the first choice in terms of effectively fracturing the calcification while reducing the risks of artery dissection and perforation. In the use of the cutting balloon, the data suggest that a balloon-to-artery ratio of 1:1, which is currently recommended for conventional balloons, is inappropriate.

In Chapter 4, the author focuses on a 180° calcification in the artery model and investigates the influence of the lesion/device diameter ratio and the number of blades facing the calcification model. The data showed that in the case where two blades face the calcification, 0.25 mm or 0.5 mm undersized balloons in comparison with the reference diameter would be effective in not only expanding the calcified lesion but also reducing the risk of dissection and vessel perforation.

In Chapter 5, a summary of the achievement and mechanical insights for the expansion of the cutting balloon was described in this chapter. The author described the future work of this study.

This study described a novel approach to generate a three-folded shape of the balloon and successfully constructed the cutting balloon models. Moreover, numerical simulations showed the effect on the balloon-to-artery ratio and number of blades facing the calcification during the expansion of the cutting balloon. This is the first three-dimensional numerical investigation on

the expansion of the cutting balloon in a calcified artery model. These mechanical findings revealed the importance of balloon-to-artery ratio in the cutting balloon angioplasty and the direction of the blades facing the calcification plays a role in the expansion with potentially fracturing the calcification and avoiding arterial injury. This study is a significant contribution to the cutting balloon angioplasty.

5.3 Future work

The author purposes a useful and straightforward numerical method to generate a wrapped balloon using the compliance chart. The initial diameter and isotropic elastic material properties were determined, and the process of crimping and compressing was developed to complete the wrapped balloon shape. Although its reliability and accuracy have been verified through the stent expansion compared with a simple cylinder surface model, a realistic and complex material should be considered to mimic the mechanical behavior of the balloon. Experimental tests and material constitutions could be considered to enrich the material definition.

The calcification models were created in two cases of 360° and 180°. More variations in calcium arc, diameter stenotic ratio, and thickness and length of the calcification should also be considered to further understand the efficacy and safety of the cutting balloon. Some of these parameters can be obtained from patients by clinical imaging technologies to define typical cases of lesions.

Furthermore, different components mixed types of plaques in lesions with crack or failure for the plaque model and dissection or perforation behavior occurs at the artery wall might be the challenge in this study. Some cardiovascular events occur in the cutting balloon angioplasty or in the stent implantation after cutting balloon expansion. More mechanical challenges

considered in the study may contribute to the clinical outcome.

References

[1] James, S. L., et al. Global, regional, and national incidence, prevalence, and years lived with disability for 354 diseases and injuries for 195 countries and territories, 1990-2017: a systematic analysis for the Global Burden of Disease Study 2017. The Lancet 392(10159) (2018): 1789-1858.

[2] Roth, G. A., et al. Global, regional, and national age-sex-specific mortality for 282 causes of death in 195 countries and territories, 1980-2017: a systematic analysis for the Global Burden of Disease Study 2017. The Lancet 392(10159) (2018): 1736-1788.

[3] Mori, H., et al. Coronary artery calcification and its progression: what does it really mean?. JACC: Cardiovascular Imaging 11(1) (2018): 127-142.

[4] Madhavan, M. V., et al. Coronary artery calcification: pathogenesis and prognostic implications. Journal of the American College of Cardiology 63(17) (2014): 1703-1714.

[5] Savage, M. P., et al. Clinical and angiographic determinants of primary coronary angioplasty success. Journal of the American College of Cardiology 17(1) (1991): 22-28.

[6] Tan, K., et al. Clinical and lesion morphologic determinants of coronary angioplasty success and complications: current experience. Journal of the American College of Cardiology 25(4) (1995): 855-865.

[7] Nobuyoshi, M., et al. Restenosis after percutaneous transluminal coronary angioplasty: pathologic observations in 20 patients. Journal of the American College of Cardiology 17(2) (1991): 433-439.

[8] Fitzgerald, P. J., et al. Contribution of localized calcium deposits to dissection after angioplasty. An observational study using intravascular ultrasound. Circulation 86(1) (1992): 64-70.

[9] Fasseas, P., et al. Incidence, correlates, management, and clinical outcome of coronary perforation: analysis of 16,298 procedures. American Heart Journal 147(1) (2004): 140-145.

[10] Kempczinski, R. Intravascular stents to prevent occlusion and restenosis after transluminal angioplasty: Sigwart U, Puel J, Mirkovitch V, Joffre F, Kappenberger L. N Engl J Med 1987; 316: 701-6. Journal of Vascular Surgery 6(5) (1987): 533.

[11] Fischman, D. L., et al. A randomized comparison of coronary-stent placement and balloon angioplasty in the treatment of coronary artery disease. New England Journal of Medicine 331(8) (1994): 496-501.

[12] Serruys, P W., et al. A comparison of balloon-expandable-stent implantation with balloon angioplasty in patients with coronary artery disease. New England Journal of Medicine 331(8) (1994): 489-495.

[13] Hoffmann, R., et al. Treatment of calcified coronary lesions with Palmaz-Schatz stents: an intravascular ultrasound study. European Heart Journal 19(8) (1998): 1224-1231.

[14] Vavuranakis, M., et al. Stent deployment in calcified lesions: Can we overcome calcific restraint with hightpressure balloon inflations?. Catheterization and Cardiovascular iInterventions 52(2) (2001): 164-172.

[15] Jensen, L. O., et al. Stent thrombosis, myocardial infarction, and death after drug-eluting and bare-metal stent coronary interventions. Journal of the American College of Cardiology 50(5) (2007): 463-470.

[16] Moses, J. W., et al. Sirolimus-eluting stents versus standard stents in patients with stenosis in a native coronary artery. New England Journal of Medicine 349(14) (2003): 1315-1323.

[17] Khattab, A. A., et al. Drug-eluting stents versus bare metal stents following rotational atherectomy for heavily calcified coronary lesions: late angiographic and clinical follow-up results. Journal of Interventional Cardiology 20(2) (2007): 100-106.

[18] Rathore, S., et al. Rotational atherectomy for fibr-calcific coronary artery disease in drug eluting stent era: Procedural outcomes and angiographic follow-up results. Catheterization and Cardiovascular Interventions 75(6) (2010): 919-927.

[19] Bangalore, S., et al. Percutaneous coronary intervention of moderate to severe calcified coronary lesions: insights from the National Heart, Lung, and Blood Institute Dynamic Registry. Catheterization and Cardiovascular Interventions 77(1) (2011): 22-28.

[20] Moussa, I., et al. Impact of coronary culprit lesion calcium in patients undergoing paclitaxel-eluting stent implantation (a TAXUS-IV sub study). The American Journal of Cardiology 96(9) (2005): 1242-1247.

[21] Kawaguchi, R., et al. Impact of lesion calcification on clinical and angiographic outcome after sirolimus-eluting stent implantation in real-world patients. Cardiovascular Revascularization Medicine 9(1) (2008): 2-8.

[22] Onuma, Y., et al. Efficacy of everolimus eluting stent implantation in patients with calcified coronary culprit lesions: two-year angiographic and three-year clinical results from the SPIRIT II study. Catheterization and Cardiovascular Interventions 76(5) (2010): 634-642.

[23] Vaquerizo, B., et al. Aggressive plaque modification with rotational atherectomy and/or cutting balloon before drug-eluting stent implantation for the treatment of calcified coronary lesions. Journal of Interventional Cardiology 23(3) (2010): 240-248.

[24] Abdel-Wahab, M., et al. High-Speed Rotational Atherectomy Versus Modified Balloons Prior to Drug-Eluting Stent Implantation in Severely Calcified Coronary Lesions: The Randomized PREPARE-CALC Trial. Circulation: Cardiovascular Interventions 11(10) (2018): e007415.

[25] Okura, H., et al. Mechanisms of acute lumen gain following cutting balloon angioplasty in calcified and noncalcified lesions: an intravascular ultrasound study. Catheterization and

Cardiovascular Interventions 57(4) (2002): 429-436.

[26] Tang, Z., et al. Cutting-balloon angioplasty before drug-eluting stent implantation for the treatment of severely calcified coronary lesions. Journal of Geriatric Cardiology: JGC 11(1) (2014): 44.

[27] Mauri, L., et al. Cutting balloon angioplasty for the prevention of restenosis: results of the Cutting Balloon Global Randomized Trial. The American Journal of Cardiology 90(10) (2002): 1079-1083.

[28] Martí, V., et al. Significance of angiographic coronary dissection after cutting balloon angioplasty. American Journal of Cardiology 81(11) (1998): 1349-1352.

[29] Levine, G. N., et al. 2011 ACCF/AHA/SCAI guideline for percutaneous coronary intervention: a report of the American College of Cardiology Foundation/American Heart Association Task Force on Practice Guidelines and the Society for Cardiovascular Angiography and Interventions. Circulation 124(23) (2011): e574-e651.

[30] Allen, D. W. and Prashant K. Atherectomy and Specialty Balloons in Percutaneous Coronary Intervention. Current Treatment Options in Cardiovascular Medicine 21(3) (2019): 13.

[31] Liang, D. K., et al. Finite element analysis of the implantation of a balloon-expandable stent in a stenosed artery. International Journal of Cardiology 104(3) (2005): 314-318.

[32] Marrey, Ramesh V., et al. Fatigue and life prediction for cobalt-chromium stents: A fracture mechanics analysis. Biomaterials 27(9) (2006): 1988-2000.

[33] Wang, W., et al. Analysis of the transient expansion behavior and design optimization of coronary stents by finite element method. Journal of Biomechanics 39(1) (2006): 21-32.

[34] Takashima, K., et al. Simulation and experimental observation of contact conditions between stents and artery models. Medical Engineering & Physics 29(3) (2007): 326-335.

[35] Lim, D., et al. Suggestion of potential stent design parameters to reduce restenosis risk driven by foreshortening or dogboning due to non-uniform balloon-stent expansion. Annals of Biomedical Engineering 36(7) (2008): 1118-1129.

[36] Martin, D. and Fergal B. Finite element analysis of balloon-expandable coronary stent deployment: Influence of angioplasty balloon configuration. International Journal for Numerical Methods in Biomedical Engineering 29(11) (2013): 1161-1175.

[37] De Beule, M., et al. Realistic finite element-based stent design: the impact of balloon folding. Journal of Biomechanics 41(2) (2008): 383-389.

[38] Ragkousis, G. E., et al. Computational modelling of multi-folded balloon delivery systems for coronary artery stenting: insights into patient-specific stent malapposition. Annals of Biomedical Engineering 43(8) (2015): 1786-1802.

[39] Zahedmanesh, H. and Caitríona L. Determination of the influence of stent strut thickness using the finite element method: implications for vascular injury and in-stent restenosis. Medical & Biological Engineering & Computing 47(4) (2009): 385.

[40] Azaouzi, M., et al. On the numerical investigation of cardiovascular balloon-expandable stent using finite element method. Computational Materials Science 79 (2013): 326-335.

[41] Imani, M., et al. Finite element analysis of mechanical behaviors of multi-link stent in a coronary artery with plaque. World Applied Sciences Journal 21(11) (2013): 1597-1602.

[42] Schiavone, A., et al. Effects of material, coating, design and plaque composition on stent deployment inside a stenotic artery-finite element simulation. Materials Science and Engineering: C 42 (2014): 479-488.

[43] Riel, L., et al. Characterization of calcified plaques retrieved from occluded arteries and comparison with potential artificial analogues. ASME International Mechanical Engineering Congress and Exposition. Vol. 46469. American Society of Mechanical Engineers, 2014.

[44] Kawase, Y., et al. Utility of a scoring balloon for a severely calcified lesion: bench test and finite element analysis. Cardiovascular Intervention and Therapeutics 29(2) (2014): 134-139.

[45] Song, X., et al. Efficacy of the Wolverine cutting balloon on a circumferential calcified coronary lesion: Bench test using a three-dimensional printer and computer simulation with the finite element method. Cardiovascular Intervention and Therapeutics (2021): 1-11.

[46] Fujino, A., et al. Predictors of calcium fracture derived from balloon angioplasty and its effect on stent expansion assessed by optical coherence tomography. JACC: Cardiovascular Interventions 11(10) (2018): 1015-1017.

[47] De Beule, M. Finite element stent design. Diss. Ghent University, 2008.

[48] Ventsel, E., et al. Thin plates and shells: theory, analysis, and applications. Applied Mechanics Reviews 55(4) (2002): B72-B73.

[49] Lange, R. A. and Hillis, L. D. Second-generation drug-eluting coronary stents. New England Journal of Medicine 362(18) (2010): 1728-1730.

[50] Poncin, P. and Proft, J. Stent tubing: understanding the desired attributes. In: Medical device materials: proceedings of the materials & processes for medical devices conference. (2004): 253-259.

[51] Holzapfel, G. A., et al. Determination of layer-specific mechanical properties of human coronary arteries with nonatherosclerotic intimal thickening and related constitutive modeling. American Journal of Physiology-Heart and Circulatory Physiology 289(5) (2005): H2048-H2058.

[52] Gervaso, F., et al. On the effects of different strategies in modelling balloon-expandable stenting by means of finite element method. Journal of Biomechanics 41(6) (2008): 1206-1212.

[53] Zahedmanesh, H. and Caitríona L. Determination of the influence of stent strut thickness using the finite element method: implications for vascular injury and in-stent restenosis. Medical & Biological Engineering & Computing 47(4) (2009): 385-393.

[54] Karimi, A., et al. A computational fluid-structure interaction model for plaque vulnerability assessment in atherosclerotic human coronary arteries. Journal of Applied Physics 115(14) (2014): 144702.

[55] Prendergast, P. J., et al. Analysis of prolapse in cardiovascular stents: a constitutive equation for vascular tissue and finite-element modelling. Journal of Biomechanical Engineering 125(5) (2003): 692-699.

[56] Sadat, U., et al. Biomechanical structural stresses of atherosclerotic plaques. Expert Review of Cardiovascular Therapy 8(10) (2010): 1469-1481.

[57] Zhu, X., et al. Finite element analysis of the cutting balloon with an adequate balloon-to-artery ratio for fracturing calcification while preventing perforation. Circulation Reports 3(1) (2021): 1-8.

[58] Kubo, T., et al. Superficial calcium fracture after PCI as assessed by OCT. JACC: Cardiovascular Imaging 8(10) (2015): 1228-1229.

[59] Mintz, G. S., et al. Patterns of calcification in coronary artery disease: a statistical analysis of intravascular ultrasound and coronary angiography in 1155 lesions. Circulation 91(7) (1995): 1959-1965.

[60] Becker, A., et al. A comparative study of clinically well-characterized human atherosclerotic plaques with histological, chemical, and ultrastructural methods. Journal of Inorganic Biochemistry 98(12) (2004): 2032-2038.

[61] Ebenstein, D. M., et al. Nanomechanical properties of calcification, fibrous tissue, and hematoma from atherosclerotic plaques. Journal of Biomedical Materials Research Part A: An

Official Journal of The Society for Biomaterials, The Japanese Society for Biomaterials, and The Australian Society for Biomaterials and the Korean Society for Biomaterials 91(4) (2009): 1028-1037.

[62] Coughlin, D. G. Nanomechanical properties, composition, and mineral-density distributions of late-stage atherosclerotic calcifications. Diss. University of California, San Francisco with the University of California, Berkeley, 2005.

[63] Zhu, X., et al. Finite element analysis of cutting balloon expansion in a calcified artery model of circular angle 180°: Effects of balloon-to-diameter ratio and number of blades facing calcification on potential calcification fracturing and perforation reduction. PLoS ONE 16(5)(2021): e0251404.

[64] Iwasaki, K., et al. Repeated 3-times-balloon-inflation for Stent Deployment Increases Luminal Patency of Cobalt Alloy Stent: In vitro Study Using 75% Stenotic Mechanically-equivalent Coronary Artery Replica. Circulation 120 (2009): S196.

[65] Hikichi, Y., et al. Reduction in incomplete stent apposition area caused by jailed struts after single stenting at left main bifurcation lesions: micro-CT analysis using a three-dimensional elastic bifurcated coronary artery model. Cardiovascular Intervention and Therapeutics 32(1) (2017): 12-17.

Research achievements

By Type	theme, journal name, date & year of publication, name of authors inc. yourself
Academic Papers	○ (1) **X. Zhu**, M. Umezu. K. Iwasaki. Finite element analysis of cutting balloon expansion in a calcified artery model of circular angle 180°: Effects of balloon-to-diameter ratio and number of blades facing calcification on potential calcification fracturing and perforation reduction. PLoS ONE.16(5): e0251404.2021.5 ○ (2) **X. Zhu**, M. Umezu. K. Iwasaki. Finite element analysis of the cutting balloon with an adequate balloon-to-artery ratio for fracturing calcification while preventing perforation. Circulation Reports.3(1): 1-8.2021.1 (3) A. Takahashi, **X. Zhu**, Y. Aoyama, M. Umezu, K. Iwasaki, Three-dimensional strain measurements of tubular elastic model using tomographic particle image velocimetry, Cardiovasc Eng Technol. s13239-018-0350-5, 1-10, 2018.3
Conference abstract	(1) R. Ito, **X. Zhu**, K. Matsubara, K. Sugiyama, M. Yumoto, M. Umezu, K. Iwasaki, Influences of thickness and circumferential angles of calcification on the capability of fracturing calcification of the cutting balloon: an experimental investigation, euro PCR 2019, Paris, 24 May.2019 (2) K. Matsubara, Y. Hikichi, K. Sugiyama, **X. Zhu**, Y. Tsuboko, Y. Matsuhashi, R. Ito, K. Iwasaki, Experimental investigation of influence of stent designs on jailed struts and flow using a left main coronary artery model, euro PCR 2019, Paris, 21-24 May.2019 (3) J. Kozaki, **X. Zhu**, K. Shukuzawa, M. Umezu, K. Iwasaki, Finite element analysis of potential migration of a stent graft into thoracic aotic aneurysm, EMBC 2018, Honolulu, 20 July.2018 (4) **X. Zhu**, M. Umezu, K. Iwasaki, Finite element analysis on expansion of cutting balloon in calcified coronary artery in comparison with conventional balloon, EMBC 2018, Honolulu, 20 July.2018 (5) **X. Zhu**, Y. Mizutani, M. Umezu, K. Iwasaki, Finite element amalysis of the radial artery compression devices to investigate relationships between an inflation volume and compression pressure of wrist tissue, CMBBE 2018, Lisbon, 27 Mar.2018 (6) J. Takada, **X. Zhu**, K. Mahara, H. Kasegawa, M.Umezu, K. Iwasaki, Finite element analysis on the influence of distance between anterior and posterior papillary muscles on the stress distribution of the stentless mitral valve at closure, CMBBE 2018, Lisbon, 26 Mar.2018 (7) **X. Zhu**, M. Umezu, K Iwasaki, Finite Element Analysis of Self-Expanding Nitinol Stent under Torsion and Shortening Conditions of superficial femoral Artery, 39th Annual International Conference of the IEEE Engineering in Medicine and Biology Society, Jeju Island, 11-15 July.2017

By Type	theme, journal name, date & year of publication, name of authors inc. yourself
Conference abstract	(8) 湯本幹基, 杉山航太, 松原海人, 伊藤遼太, 朱暁冬, 梅津光生, 岩﨑清隆, 腸骨静脈ステントの性能評価のためのブタ腹部大静脈の力学的特性の取得と加速耐久試験装置の開発, 第 42 回日本バイオレオロジー学会年会, P25, 福岡, 2019 年 6 月 2 日 (9) 水谷泰之，松原海斗，杉山航太，湯本幹基，伊藤遼太，朱暁冬，梅津光生，岩﨑清隆，浅大腿動脈でのねじり伸縮複合負荷環境における重複留置したステントの破断耐久性に関する研究，第 29 回バイオフロンティア講演会，p.2C13，千葉, 2018 年 10 月 25 日 (10) 水谷泰之，和泉恒平，高橋啓明，松原海斗，杉山航太，朱暁冬，梅津光生，岩﨑清隆，生体吸収性スキャフォールドの経時的拡張保持特性と分解特性に関する研究，第 30 回バイオエンジニアリング講演会，p.348，京都，2017 年 12 月 15 日 (11) 水谷泰之，松原海斗，朱暁冬，鮫島啓，杉山航太，挽地裕，梅津光生，岩﨑清隆，粒子イメージ流速計測法を用いたステントデザインが分岐狭窄病変における血流に及ぼす影響の検討，第 28 回バイオフロンティア講演会，2B31，徳島，2017 年 10 月 29 日 (12) 朱暁冬，梅津光生，岩﨑清隆，有限要素法を用いた屈曲変形時における冠動脈ステントの応力解析，日本機械学会 2017 年度年次大会，埼玉，2017 年 9 月 4 日 (13) 朱暁冬，橋本雅也，梅津光生，岩﨑清隆：浅大腿動脈のねじり短縮複合負荷に対する自己拡張型 Ni-Ti 合金製ステントの有限要素解析，第 40 回日本バイオレオロジー学会年会，p.126，岡山，2017 年 5 月 28 日 (14) 徳武祐論，岩﨑清隆，朱暁冬，梅津光生，複合負荷の作用する大腿膝窩動脈へ留置した自己拡張型 Ni-Ti 合金製ステントの疲労解析，第 28 回バイオエンジニアリング講演会，2B15，東京，2016 年 1 月 9 日 (15) 徳武祐論，岩﨑清隆，朱暁冬，梅津光生：下肢浅大腿動脈へ留置した自己拡張型 Ni-Ti 合金製ステントに生じるひずみ解析，第 26 回バイオフロンティア講演会，113-114，福岡，2015 年 10 月 (16) 徳武祐論，岩﨑清隆，朱暁冬，梅津光生，狭窄を有する下肢浅大腿動脈に事項拡張型ステントを適用時に生じる応力解析，第 31 回ライフサポート学会， 54-55，福岡，2015 年 9 月 8 日 (17) 朱暁冬，岩﨑清隆，徳武祐論，梅津光生，有限要素法を用いた繰り返し屈曲変形が冠動脈ステントの破断に及ぼす影響の検討，第 25 回バイオフロンティア講演会，pp.75-76，鳥取，2014 年 10 月 3 日

By Type	theme, journal name, date & year of publication, name of authors inc. yourself
Conference abstract	(18) 徳武祐論，岩﨑清隆，**朱暁冬**，梅津光生，自己拡張型 Ni-Ti 合金製ステントを留置した浅大腿動脈の応力解析, 第 25 回バイオフロンティア講演会，pp.77-78，鳥取，2014 年 10 月 3 日 (19) **朱暁冬**，岩﨑清隆，徳武祐論，梅津光生，繰り返し屈曲変形の角度変化量が冠動脈ステントの破断に及ぼす影響の有限要素法解析，LIFE2014 生活生命支援医療福祉工学系学会連合大会，留寿都，2014 年 9 月 24 日